

University of Windsor

Scholarship at UWindor

Electronic Theses and Dissertations

Theses, Dissertations, and Major Papers

6-18-2021

Development of Polymer Composite Coatings for Condensing Heat Exchangers

Joselyne McPhedran
University of Windsor

Follow this and additional works at: <https://scholar.uwindsor.ca/etd>

Recommended Citation

McPhedran, Joselyne, "Development of Polymer Composite Coatings for Condensing Heat Exchangers" (2021). *Electronic Theses and Dissertations*. 8606.
<https://scholar.uwindsor.ca/etd/8606>

This online database contains the full-text of PhD dissertations and Masters' theses of University of Windsor students from 1954 forward. These documents are made available for personal study and research purposes only, in accordance with the Canadian Copyright Act and the Creative Commons license—CC BY-NC-ND (Attribution, Non-Commercial, No Derivative Works). Under this license, works must always be attributed to the copyright holder (original author), cannot be used for any commercial purposes, and may not be altered. Any other use would require the permission of the copyright holder. Students may inquire about withdrawing their dissertation and/or thesis from this database. For additional inquiries, please contact the repository administrator via email (scholarship@uwindsor.ca) or by telephone at 519-253-3000ext. 3208.

Development of Polymer Composite Coatings for Condensing Heat Exchangers

By

Joselyne McPhedran

A Thesis
Submitted to the Faculty of Graduate Studies
through the Department of Mechanical, Automotive, and Materials Engineering
in Partial Fulfillment of the Requirements for
the Degree of Master of Applied Science
at the University of Windsor

Windsor, Ontario, Canada

2021

© 2021 Joselyne McPhedran

Development of Polymer Composite Coatings for Condensing Heat Exchangers

by

Joselyne McPhedran

APPROVED BY:

M. Mirhassani
Department of Electrical and Computer Engineering

A. R. Riahi
Department of Mechanical, Automotive and Materials Engineering

Y. He, Co-Advisor
CanmetMATERIALS, Natural Resources Canada

A. Edrisy, Co-Advisor
Department of Mechanical, Automotive and Materials Engineering

March 26, 2021

DECLARATION OF ORIGINALITY

I hereby certify that I am the sole author of this thesis and that no part of this thesis has been published or submitted for publication.

I certify that, to the best of my knowledge, my thesis does not infringe upon anyone's copyright nor violate any proprietary rights and that any ideas, techniques, quotations, or any other material from the work of other people included in my thesis, published or otherwise, are fully acknowledged in accordance with the standard referencing practices. Furthermore, to the extent that I have included copyrighted material that surpasses the bounds of fair dealing within the meaning of the Canada Copyright Act, I certify that I have obtained a written permission from the copyright owner(s) to include such material(s) in my thesis and have included copies of such copyright clearances to my appendix.

I declare that this is a true copy of my thesis, including any final revisions, as approved by my thesis committee and the Graduate Studies office, and that this thesis has not been submitted for a higher degree to any other University or Institution.

ABSTRACT

Polymer coatings exhibit superior corrosion resistance, making them a good solution to protect heat exchange components from chemical attack in low temperature heat recovery. Nonetheless, major shortcomings to using polymer coatings include their low thermal conductivity, low strength, and susceptibility to wear. Studies conducted collaboratively by the University of Windsor and CanmetMATERIALS have investigated the suitability of perfluoroalkoxy (PFA) composite coatings with conductive filler materials, such as graphene, for polymer composite coatings. The following research investigates the impact of two different filler incorporation techniques, ball milling and magnetic functionalization, to optimize the microstructural, thermal, and tribological properties of the polymer composite coating. Through microscopy, the investigation revealed that the ball milled samples display excellent filler particle distribution, and a general lateral alignment of graphite filler particles. The composites displayed a decrease in the thermal conductivity after ball milling, resulted from the lateral alignment of filler particles and measurement of the thermal properties in the out-of-plane direction. Furthermore, Raman analysis indicated that the ball milling process did not produce monolayer graphene. The magnetically functionalized multi-layer graphene (MF-MLG) particles were responsive to an external magnet however, microscopy showed that the MF-MLG were not aligned within the polymer matrix. A combination of abrasive and adhesive wear was observed through pin-on-disk wear testing; higher weight fractions of filler resulted in lower wear resistance. All composites displayed very low coefficient of friction values throughout testing.

DEDICATION

To my family and friends, for their endless support and encouragement.

ACKNOWLEDGEMENTS

First and foremost, I would like to thank my supervisors Dr. Afsaneh Edrisy and Dr. Youliang He for their guidance and continuous support throughout my graduate studies. Their mentorship, expertise, and advice regarding my research has been invaluable. I would like to thank my research committee members, Dr. Mitra Mirhassani and Dr. Reza Riahi for their time, feedback, and insightful suggestions.

I would like to thank my research colleagues from the University of Windsor; Mitchell Cierpisz, Lucas Chauvin, Liza Dicecco, Dr. Mehdi Mehdi, Dr. Olufissayo Gali, Razieh Kiani Harchegani, Iman Borojeni, Junhui Ma, and Javad Mohammadi. I am grateful for their friendship, guidance, and training throughout my studies. I would like to thank Sharon Lackie for her time coordinating with me virtually and technical support conducting SEM and Raman Spectroscopy. I would also like to thank Mark Gryn and Andy Jenner for their technical support, and Angela Haskell for her administrative assistance.

I would also like to thank my research colleagues from CanmetMATERIALS, Dan Walsh, Ruby Zhang, Renata Zavadil, Maciej Podlesny, Raul Santos, Mason Thomas, Maggie Matchim, and Christine Sheldrick, for their assistance in adjusting to a new lab, guidance, and welcoming me in a new city. A special thank you to Dr. Taylor Martino for her friendship, continued support, and encouragement while working on my thesis.

Lastly, I am sincerely thankful for my parents Heather and Jim McPhedran, their genuine support and encouragement has continually motivated me to strive for

success throughout my studies. I sincerely appreciate all my family and friends, especially Nick, for their unlimited love, patience, and wholehearted support during my graduate studies.

TABLE OF CONTENTS

DECLARATION OF ORIGINALITY	iii
ABSTRACT.....	iv
DEDICATION	v
ACKNOWLEDGEMENTS	vi
LIST OF TABLES	x
LIST OF FIGURES	xi
LIST OF ABBREVIATIONS/SYMBOLS.....	xvii
CHAPTER 1: INTRODUCTION.....	1
1.1 Background and Motivation.....	1
1.2 Objectives of Study	3
1.3 Organization of Thesis	3
CHAPTER 2: LITERATURE SURVEY.....	5
2.1 Introduction	5
2.2 Low-Temperature Corrosion of Heat Exchangers	5
2.2.1 Dew Point Corrosion	6
2.2.2 Corrosion of Metal Heat Exchangers	9
2.2.3 Corrosion Resistant Polymer Coatings.....	12
2.3 Polymer Composite Coatings.....	15
2.3.1 Selection of Polymer Matrix.....	15
2.3.2 Recent Advances in PFA-Composite Coatings	16
2.4 Graphene, Multi-Layer Graphene, and Graphite Nanosheets	20
2.5 Graphene-Polymer Composites	22
2.5.1 Factors Limiting the Thermal Performance of Graphene-Polymer Composites	25
2.5.2 Graphene Incorporation via Ball Milling	28
2.5.3 Graphene Incorporation via Magnetic Functionalization.....	32
CHAPTER 3: MATERIALS AND EXPERIMENTAL METHODS.....	35
3.1 Bulk Materials	36
3.2 Filler Incorporation Methods	37
3.2.1 Ball Milling.....	37
3.2.1.1 Naming System for Ball Milled Samples	39
3.2.2 Magnetic Functionalization	39
3.2.2.1 Determination of Graphene Content in MF-MLG.....	41
3.2.2.2 Naming System for Magnetically Functionalized Samples.....	42
3.3 Sample Preparation Process	43
3.3.1 Compression-Molded Disks	43
3.3.2 Electrostatically Sprayed Coupons.....	45
3.4 Sample Analysis Methods.....	47

3.4.1 Microscopy	47
3.4.1.1 Sample Preparation for Microscopy	47
3.4.1.2 Microscopy and Image Analysis.....	48
3.4.2 Surface Topography	49
3.4.3 Thermal Property Analysis	49
3.4.4 Wear Testing.....	50
3.4.4.1 Wear Test Analysis	51
3.4.5 Raman Spectroscopy	52
CHAPTER 4: EXPERIMENTAL RESULTS	55
4.1 Microstructural Analysis	55
4.1.1 Microstructural Analysis of Compression-Molded Disks	55
4.1.2 Microstructural Analysis of Electrostatically Sprayed Composite Coatings	63
4.1.3 Microscopy Image Analysis	66
4.1.4 Morphology and Compositional Analysis of Blended Powders	69
4.2 Surface Topography Analysis	73
4.3 Thermal Analysis	74
4.4 Wear Test Results.....	83
4.4.1 Coefficient of Friction and Wear Rates	83
4.4.2 Microscopy Analysis of Worn surfaces.....	90
4.5 Raman Spectroscopy Results	98
CHAPTER 5: DISCUSSION.....	102
5.1 Composite Morphology.....	102
5.1.1 Effect of Ball Milling on Filler Particle Alignment and Distribution ..	102
5.1.2 Effect of Compression Molding Versus Electrostatic Coating on Microscopy	104
5.1.3 Effect of MF-MLG Particles on Composite Microstructure	105
5.1.4 Effect of Filler Particles on Surface Topography	106
5.1.5 Effect of Ball Milling on Raman Spectra	108
5.2 Thermal Properties	109
5.3 Wear Behaviour of Composite Coatings.....	113
CHAPTER 6: CONCLUSIONS	117
6.1 Conclusions	117
6.2 Recommendations	119
REFERENCES	121
VITA AUCTORIS	137

LIST OF TABLES

Table 2.1 Common sources, their corresponding temperatures, and typical recovery methods for low-temperature waste heat (table reproduced from [1]).	6
Table 3.1 Selected properties and dimensions of PFA and graphite filler materials [42], [64], [116].....	36
Table 3.2 Schedule of ball milling experiments: time, filler type and weight percentage.	38
Table 3.3 Calculation of the graphene content in the produced MF-MLG.....	42
Table 4.1 The area percentages of fillers calculated using the ImageJ software for various fillers, weight percentages, and ball milling times.....	68
Table 4.2 The arithmetic mean height surface roughness (R_a) and root mean square roughness (R_q) values obtained from optical /laser microscopy (scan area: $1000 \times 1400 \text{ um}^2$).....	73
Table 4.3 The mass loss or gain of both the composite-coated samples and the stainless steel counter-face ball.....	87
Table 4.4 The average wear area, wear volume, and corresponding wear rate (in terms of volume removed over sliding distance) for various composite-coated samples after pin-on-disk wear testing.	88

LIST OF FIGURES

Figure 2.1 The effect of the surface temperature of heat exchange elements on low-temperature corrosion [2].	8
Figure 2.2 SEM image of low alloy steel specimen #1 immersed in 30% H ₂ SO ₄ solution for 48 hours [21].	10
Figure 2.3 Thermal conductivity of PFA composites with respect to temperature (the "x" shows the thermal conductivity of pure PFA) [7].	18
Figure 2.4 SEM images of the PFA-20wt% graphite samples following microscratch testing (0.03 to 28N loading, 3mm length scratch track). (a) Secondary electron (SE) image of the overall scratch morphology, with the enclosed areas illustrated at higher magnification. (b) back-scattered electron (BSE) image of location "b" in Figure 2.4(a) showing micro-crack initiation and flattening of graphite particles. (c) BSE image of location "c" in Figure 2.4(a) displaying failure exposed substrate indicating delamination of the polymer coating, elongated strands along the scratch direction, and un-melted PFA particles [7].	20
Figure 2.5 Schematic of thermal conductive mechanisms at the interface between graphene and polymer materials [12].	26
Figure 2.6 Schematic of the ball milling process incorporating the graphene and polymer powders [97].	30
Figure 2.7 Schematic illustration of graphene magnetic functionalization process [13].	33
Figure 3.1 Schematic illustration of the experimental methods and procedures used in this research, divided into three steps: filler incorporation, sample preparation, and sample analysis.	35
Figure 3.2 Photograph of the dried MF-MLG particles attracted to an external magnetic force. The MF-MLG particles produced from both trial 1 and trial 2 were magnetically responsive.	41
Figure 3.3 (a) Curing scheme for the compression-molded disks [7], and (b) schematic of magnetic alignment of filler particles in composite disk.	44
Figure 3.4 Schematic of the compression molded samples: (a) waterjet cutting schemes, and (b) cross-section of the samples for microscopy.	45

Figure 3.5 (a) Curing scheme for electrostatically coated primer powder and blended powder mixtures [7], (b) schematic illustration of the coating cross-section, and (c) schematic illustration of the cross-section of the primer and top coating layers, and the magnetic alignment of MF-MFG filler particles within the top-coat layer.....	47
Figure 3.6 (a) Micrograph of the PFA composite with 20 wt % 60 nm MLG filler ball milled for 25 hours (60nm-20wt%-25h), and (b) the micrograph produced using the ImageJ software by applying a binary mask.....	49
Figure 3.7 (a) Schematic of the wear track, with micrographs taken at the 4 locations indicated. (b) Micrograph of the wear track, with wear profiles extracted at the 6 locations indicated, and (c) A wear profile taken at 1 of the 6 indicated locations.....	52
Figure 3.8 (a) The Raman spectra (514 nm excitation) of graphene compared to bulk graphite, with the main peak locations marked, and (b) The Raman spectra (514 nm excitation) of the 2D band as it evolves from monolayer graphene to bulk graphite, with the shoulder (red) and peak (blue) locations labelled (graphs reproduced from Ferrari et al. [130])......	53
Figure 4.1 Laser/optical micrographs of the PFA- 60 nm MLG composite samples: (a) 60nm-20wt%-0h at low magnification [8], (b) 60nm-20wt%-25h at low magnification, (c) 60nm-20wt%-0h at high magnification [8], and (d) 60nm-20wt%-25h at high magnification. It is important to note that all the micrographs are of compression molded disks except Figure 4.1c, which is an electrostatically coated coupon.....	57
Figure 4.2 Laser/optical micrographs of the PFA- 9 μm graphite composite compression molded samples containing 20 wt% filler with increasing ball milling times: (a) 0 hours, (b) 5 hours, (c) 10 hours, (d) 15 hours, (e) 20 hours, (f) 25 hours, and (g) 30 hours.....	59
Figure 4.3 Laser/optical micrographs of the PFA-44 μm graphite composite compression molded samples: (a) 44 μm -20wt%-0h, (b) 44 μm -20wt%-25h.	60
Figure 4.4 Laser/optical micrographs of the PFA- 9 μm graphite composite compression molded samples: (a) 9 μm -10wt%-0h, (b) 9 μm -10wt%-25h, and (c) M9 μm -10wt%-25h.....	61
Figure 4.5 Laser/optical micrographs of the PFA- MF-MLG composite compression molded samples: (a) MF-MLG-2g-10wt% at 200 \times magnification, (b)	

MF-MLG-2g-10wt% at 500 × magnification, (c) MF-MLG-0.15g-1wt% at 200 × magnification, and (d) MF-MLG-0.15g-1wt% at 500 × magnification.....62

Figure 4.6 Example of the cross section of an electrostatically coated coupon (9µm-10wt%-25h) displaying the steel substrate followed by a ~50-µm primer layer and a subsequent ~150 - 250 µm PFA-composite top layer.....63

Figure 4.7 Laser/optical cross-sectional micrographs of the electrostatically coated PFA- composite coupons: (a) 60nm-20wt%-25h, (b) 9µm-20wt%-25h, and (c) 44µm-20wt%-25h.64

Figure 4.8 Cross-sectional laser/optical micrographs of the electrostatically coated PFA- composite samples: (a) 9µm-10wt%-25h, and (b) M9µm-10wt%-25h.65

Figure 4.9 Cross-sectional laser/optical micrographs of the electrostatically coated MF-MFG-2g-10wt% composite sample at two different locations: (a) the filler particle distribution and alignment, and (b) MF-MFG particle at the surface of the coating, leading to higher surface roughness values.....66

Figure 4.10 The area percentage of filler: (a) for compression-molded disk samples (60nm-20wt%, 9µm-20wt%, 44µm-20wt%) after 0 and 25 hours of ball milling, and (b) for the compression molded disks versus electrostatically coated coupons.....68

Figure 4.11 SEM images of the PFA-20 wt% 44 µm graphite powder mixture (before curing): (a) before ball milling, (b) after ball milling for 20h, (c) after ball milling for 25h, and (d) after ball milling for 30h.70

Figure 4.12 SEM images of the blended powder mixture (before curing) after ball milling for 25 hours containing various amounts of 44 µm graphite filler: (a) 10 wt% , (b) 15 wt%, and (c) 20 wt%.71

Figure 4.13 Energy dispersive spectroscopy analysis of the powder mixture containing 20 wt% 44 µm graphite after ball milling for 30 hours (before curing): (a) SEM image, and (b) EDS element overlay map.....71

Figure 4.14 SEM images and EDS spectra of the blended powder mixture (before curing, without ball milling) containing PFA and 10 wt% MF-MLG (MF-MLG-2g-10wt%): (a) SEM image at a lower magnification showing the PFA and MF-MLG particles, (b) a higher magnification SEM image of the area outlined in (a), showing the rough surface of the MF-MLG particle, (c) the EDS spectrum for ‘EDS Spot 1’ shown in (a), (d) the EDS spectrum for ‘EDS Spot 2’ shown in (a).72

Figure 4.15 Three-dimensional optical/laser profiles of the composite coatings: (a) 60nm-20wt%-25h, (b) 44 μ m-20wt%-25h, (c) 9 μ m-20wt%-25h, (d) MF-MFG-2g-10wt%, (e) 9 μ m-10wt%-25h, (f) M9 μ m-10wt%-25h.	74
Figure 4.16 The overall thermal property results from 25 °C to 250 °C for the composite samples containing 60 nm MLG, 9 μ m graphite, and 44 μ m graphite filler particles (no ball milling, and milled for 25 hours). The graphs summarize the: (a) thermal diffusivity values, and (b) specific heat values.....	76
Figure 4.17 The overall thermal conductivity results from 25 °C to 250 °C for the composite samples containing 60 nm MLG, 9 μ m graphite, and 44 μ m graphite filler particles (no ball milling and milled for 25 hours).	77
Figure 4.18 The thermal conductivity values from 25 °C to 250 °C for the 60 nm MLG filled composites with: (a) increasing filler weight percent (10wt%-20wt%) for samples that underwent no ball milling, versus ball milling for 25 hours, and (b) increasing ball milling time (0-30 hours) for samples with 20 wt% filler.....	79
Figure 4.19 The thermal conductivity values from 25 °C to 250 °C for the 9 μ m graphite filled composites with: (a) increasing filler weight percent (10wt%-20wt%) for samples that underwent no ball milling, versus ball milling for 25 hours, and (b) increasing ball milling time (0-30 hours) for samples with 20 wt% filler.....	80
Figure 4.20 The thermal conductivity values from 25 °C to 250 °C for the 44 μ m graphite filled composites with: (a) increasing filler weight percent (10wt%-20wt%) for samples that underwent no ball milling, versus ball milling for 25 hours, and (b) increasing ball milling time (0-30 hours) for samples with 20 wt% filler.....	81
Figure 4.21 The thermal conductivity values from 25 °C to 250 °C for the PFA composites containing MF-MLG-0.15g, MF-MLG-2g, and randomly oriented graphene filler particles.....	82
Figure 4.22 The coefficient of friction (COF) versus sliding distance curves for composite-coated samples: 60nm-20wt%-25h, 9 μ m-20wt%-25h, 44 μ m-20wt%-25h, and MF-MLG-10wt%.	84
Figure 4.23 The variation of the coefficient of friction with respect to sliding distance for composite-coated samples: 9 μ m-20wt%-25h, 9 μ m-10wt%-25h, M9 μ m-20wt%-25h.....	85
Figure 4.24 The average coefficient of friction in the steady-state region (9 μ m-20wt%-25h: ~250m to 1750m; 44 μ m-20wt%-25h: ~250m to 2125m; 9 μ m-10wt%-25h and M9 μ m-10wt%-25h: ~250m to 2500m; 60nm-20wt%-25h and MF-MLG-	

2g-10wt%: ~250m to 2800m) for composite-coated samples during pin-on-disk wear testing.86

Figure 4.25 Micrographs of the stainless steel counter-face balls after wear testing: (a) 9 μ m-20wt%-25h, (b) 9 μ m-10wt%-25h, (c) M9 μ m-10wt%-25h, (d) 44 μ m-20wt%-25h, (e) 60nm-20wt%-25h, (f) MF-MLG-2g-10wt%. The red arrow indicates the sliding direction.87

Figure 4.26 The average volumetric wear rate (in terms of volume removed over sliding distance) for various composite-coated samples after pin-on-disk wear testing.....89

Figure 4.27 Three-dimensional optical/laser profiles of the wear tracks on the composite-coated samples: (a) 9 μ m-20wt%-25h, (b) 9 μ m-10wt%-25h, (c) M9 μ m-10wt%-25h, (d) 44 μ m-20wt%-25h, (e) 60nm-20wt%-25h, (f) MF-MLG-2g-10wt%.89

Figure 4.28 Backscattered electron (BSE) images of wear tracks on the surfaces of composite coatings after 8 hours of testing: (a) 60nm-20wt%-25h, (b) 9 μ m-20wt%-25h, (c) 44 μ m-20wt%-25h, (d) 9 μ m-10wt%-25h, (e) M9 μ m-10wt%-25h, and (f) MF-MLG-2g-10wt%.....91

Figure 4.29 SEM images of the wear track on the 60nm-20wt%-25h coated sample: (a) SE image of the wear track, (b) a higher magnification BSE image of the area 'M1' outlined in (a), with EDS spectra taken at the 3 locations indicated (EDS Spot 1: Fe, Cr, Si, Al, Ni, F, S, C, O; EDS Spot 2: Fe, Cr, F, S, C, O; EDS Spot 3: F, C, O, Fe), (c) a higher magnification BSE image of the area 'M2' outlined in (a), showing coating failure in the form of cracking and tearing.93

Figure 4.30 SEM images of the wear track on the 9 μ m-20wt%-25h coated sample, (a) SE image of the wear track, (b) a higher magnification BSE image of the area outlined in (a), with EDS spectra taken at the 3 locations indicated (EDS Spot 1: Fe, F, C, O; EDS Spot 2: Fe, Cr, Si, Al, Ni, F, S, C, O; EDS Spot 3: F, S, C, O, Fe), (c) an even higher magnification BSE image of the area outlined in (a), showing coating failure in the form of tearing.94

Figure 4.31 SEM images of the wear track on the 44 μ m-20wt%-25h coated sample: (a) SE image of the wear track, (b) a higher magnification BSE image of the area 'M1' outlined in (a), with EDS spectra taken at the 2 locations indicated (EDS Spot 1: Fe, Cr, Al, F, C, O, S; EDS Spot 2: F, S, C, O), (c) a higher magnification SE image of the area 'M2' outlined in (a), showing coating failure in the form of minor cracking.95

Figure 4.32 SEM images of the composite-coating containing 10 wt% 9 μm graphite filler: (a) SE image of the wear track on the 9 μm -10wt%-25h coating, (b) a higher magnification BSE image of the area ‘M1’ outlined in (a), displaying coating failure in the form of tearing, (c) SE image of the wear track on the M9 μm -10wt%-25h coating, and (d) a higher magnification BSE image of the area ‘M2’ outlined in (c), displaying coating failure in the form of minor tearing and cracking.96

Figure 4.33 SEM images of the wear track on the MF-MLG-2g-10wt% composite coatings: (a) SE image of the wear track, (b) a higher magnification SE image of the area ‘M1’ outlined in (a), displaying large cracks within the coating, (c) a higher magnification BSE image of the area ‘M2’ outlined in (a), displaying fine cracks within the coating.....97

Figure 4.34 The Raman Spectra of graphene/graphite in composite samples containing 20 wt% filler ball milled for 0-30 hours. The graphs display the effect of ball milling time on the graphene particles: (a) 60 nm MLG, (b) 9 μm graphite, and (c) 44 μm graphite, (d) comparison of all three filler materials after 25 hours of ball milling99

Figure 4.35 Raman spectra analysis for the PFA composite samples with increasing ball milling times showing: (a) the number of graphene layers (N_G), and (b) the I_D/I_G ratio.100

Figure 4.36: The Raman Spectra of graphene/graphite in composite samples ball milled for 25 hours. The graphs display the effect of filler weight fraction (10, 15, and 20 wt% filler) on the graphene particles: (a) 60 nm MLG, (b) 9 μm graphite, and (c) 44 μm graphite.....101

Figure 4.37 Raman spectra analysis for the PFA composite samples with increasing filler weight fractions showing: (a) the number of graphene layers (N_G), and (b) the I_D/I_G ratio.....101

Figure 5.1 The laser/optical micrograph of the PFA- 60nm MLG sample, with arrows indicating the pressing direction in compression-molding.103

LIST OF ABBREVIATIONS/SYMBOLS

PFA	Perfluoroalkoxy
MLG	Multi-Layer Graphene
MF-MLG	Magnetically Functionalized Multi-Layer Graphene
SEM	Scanning Electron Microscopy
SE	Secondary Electrons
BSE	Back-Scattered Electrons
EDS	Electron Dispersive Spectrometer
SO ₂	Sulfur Dioxide
SO ₃	Sulfur Trioxide
H ₂ SO ₄	Sulfuric Acid
H ₂ SO ₃	Sulfurous Acid
WT%	Weight Percent
PTFE	Teflon
COF	Coefficient of Friction
GNPs	Graphene nanoplatelets
MWCNTs	Multi-Walled Carbon Nanotubes
ZrO ₂	Zirconium Oxide
UTS	Ultimate Tensile Strength
HRTEM	High Resolution Transmission Electron Microscopy
PWT	Polymer Wrapping Technique
LBL	Layer-by-Layer
PSS	Poly(sodium 4-styrene sulfonate)

PDDA	Poly-dimethyl-diallylammonium chloride
Fe_3O_4	Magnetite
$\gamma\text{-Fe}_2\text{O}_3$	Maghemite
M	Mole
C	Carbon
F	Fluorine
Fe	Iron
N_G	Estimated number of graphene layers
I_D/I_G	Defect Intensity Ratio

CHAPTER 1: INTRODUCTION

1.1 Background and Motivation

With an emphasis on increasing energy efficiency in modern industry, it is crucial to develop heat recovery technologies capable of capturing and re-using energy lost in the form of waste heat. The U.S. Department of Energy estimates that 20-50% of industrial energy consumption is lost as waste heat [1]. Statistics in China indicate even higher percentages, reporting industrial waste heat losses of roughly 60% [2]. Over half of the available waste heat energy is classified as low-temperature (~230 °C or lower), making this sector a valuable energy resource for industrial processes [1]. However, low-temperature waste heat is rarely recovered due to the extremely corrosive operating environments which result in catastrophic chemical attack on the heat exchange components [1]–[3]. Polymer coatings exhibit superior corrosion resistance, making them a good solution to protecting heat exchange components from chemical attack [4], [5]. Nonetheless, there are major shortcomings to using polymer coatings on heat exchangers, including, e.g., the low thermal conductivity, low strength, susceptibility to delamination and wear, etc. To address these drawbacks, filler materials may be incorporated into the polymer matrix to enhance the thermal, mechanical, and tribological properties of the coating.

Several recent studies have explored the suitability of using fluoropolymer-based composites such as perfluoroalkoxy (PFA) incorporated with thermally conductive filler materials, e.g. graphite and graphene, as heat exchanger coatings for low-temperature waste heat recovery [3], [6]–[8]. Graphene filler is believed to be able to significantly enhance the overall performance of coatings due to its extraordinary thermal and

mechanical properties [9]. However, the use of traditional processing methods (e.g. tumble mixing) to incorporate graphene filler into the polymer matrix usually produces a mixture of randomly oriented graphene particles, resulting in limited increases in the composite's thermal conductivity [8]. The present study investigates two alternative processing methods: the incorporation of graphene filler via ball milling and the incorporation of magnetically functionalized graphene filler followed by filler alignment. Incorporation of filler materials via ball milling was reported to simultaneously exfoliate graphite to produce few-layer graphene, and improve the compatibility and interfacial resistance at the graphene-polymer interface [10]. The ability to integrate filler particles through ball milling has been a proven and cost-effective method to increase filler compatibility within the polymer matrix, which increases the thermal performance of the composite [11]. The latter method, the incorporation of magnetically functionalized graphene filler, utilizes external magnetic fields to align the graphene particles in the direction of heat flux during curing. Graphene filler materials have greater thermal performance along their in-plane direction; thus filler alignment optimizes the thermal capabilities of graphene and results in increased thermal performance of graphene-polymer composites [12], [13].

This study explores advanced filler incorporation techniques to optimize the performance of graphene within PFA composite coatings. The work provides a comprehensive overview of the properties and performance of the coatings produced, specifically simulating the conditions experienced in low-temperature waste heat recovery. The development of the proposed coating enables the implementation of economically viable waste heat exchangers, thus reducing overall energy consumption in the industrial energy sector.

1.2 Objectives of Study

The objective of this research is to develop a polymer composite coating with enhanced thermal, mechanical, and tribological properties while maintaining superior corrosion resistance to the conditions experienced in low-temperature waste heat recovery. Two advanced filler incorporation techniques were investigated, aiming to improve the thermal conductivity of the composite. Ball milling was conducted for various times on three different filler particle sizes to examine its impact on the mechanical exfoliation of graphite, and the compatibility at the graphene-polymer interfaces. Extensive microscopy was performed to characterize the distribution and orientation of the filler particles within the polymer matrix. The study further aims to characterize the thermal performance, mechanical behavior, and durability of the coating, as compared to previously studied materials. This is essential to understanding the effect of the processing methods on the performance of the material, and the suitability of the coating produced for low-temperature waste heat recovery applications.

1.3 Organization of Thesis

This thesis is organized into six chapters, including the Introduction. Chapter 2 includes a literature survey of the topics relevant to this work. The mechanisms of low-temperature corrosion, the corrosion of metal heat exchangers, and the potential of protective polymer coatings are discussed. The properties of graphene and their effects on the graphene-polymer composites are evaluated. The two processing methods, the incorporation of graphene via ball milling and the incorporation of graphene via magnetic functionalization, are comprehensively reviewed. Chapter 3 introduces the materials studied and details the experimental methods utilized in this study. Chapter 4 analyzes the experimental results

and observations made throughout the research. The significance of the experimental results and the discussion of the associated physical principles and theories are presented in Chapter 5. Lastly, Chapter 6 summarizes the conclusions and provides recommendations for future work.

CHAPTER 2: LITERATURE SURVEY

2.1 Introduction

Fluoropolymers, specifically perfluoroalkoxy (PFA), are attractive candidates of coating materials for heat exchangers used in low-temperature heat recovery due to their superior corrosion resistance, melt-processability, and relatively high operating temperature (up to ~ 260 °C) [3], [6], [14]. However, they are not typically considered as an ideal material for heat recovery applications due to their intrinsically low thermal conductivity, low strength, and susceptibility to wear. To address these shortcomings, filler materials may be added to the polymer matrix to enhance the thermal and mechanical properties of the composite [3], [7], [8].

This study characterizes the properties and performance of graphene-PFA composites prepared using two different filler incorporation methods, as previously introduced in Chapter 1. This survey focuses on the mechanisms of low-temperature corrosion, and polymer composites as potential protective coating materials. The theoretical and experimental benefits of incorporating graphene via ball milling and incorporating magnetically functionalized graphene followed by filler alignment are comprehensively reviewed. Although these methods have been previously explored for polymeric materials in literature, this research provides a novel analysis of the incorporation techniques for the specific PFA-graphene composite.

2.2 Low-Temperature Corrosion of Heat Exchangers

Waste heat may be categorized into three main classes based on the temperature: high (~ 650 °C and higher), medium (~ 232 °C - 650 °C), and low (~ 232 °C and lower) [1]. Low-temperature waste heat accounts for the majority of available waste heat energy, yet it is

often disregarded due to its inferior thermal value compared to high-temperature waste heat. Nonetheless, the work potential of low-temperature waste heat is substantial and may even exceed the potential of high-temperature waste heat in certain applications [1], [3]. Common sources and potential end-uses for low-temperature waste heat are shown in *Table I*; examples include combustion exhaust gases from coal-fired boilers, gas-fired boilers, ethylene furnaces, and etcetera. The condensation of corrosive acids from the exhaust streams onto heat exchange elements presents one of the main barriers to low-temperature heat recovery.

Table 2.1 Common sources, their corresponding temperatures, and typical recovery methods for low-temperature waste heat (table reproduced from [1]).

Example Sources	Temperature (°C)	Typical Recovery Methods
Exhaust gases exiting recovery devices in gas-fired boilers, ethylene furnaces, etc.	70-230	Space heating
Process steam condensate	50-90	Domestic water heating
Cooling water from:		
furnace doors	30-50	Upgrading via heat pump to increase temperature for end use
annealing furnaces	70-230	
air compressors	30-50	
internal combustion engines	70-120	
Drying, baking, and curing ovens	90-230	Organic Rankine cycle
Hot processed liquids/ solids	30-230	

2.2.1 Dew Point Corrosion

The phenomena responsible for the corrosive operating conditions in low-temperature heat recovery is known as dew point corrosion. During the combustion of fossil fuels, such as coal and oil, sulfur content within the fuel becomes oxidized producing sulfur dioxide (SO₂) gas [2][15]. In *oxygen rich environments*, roughly 1-5% of the sulfur dioxide gas is converted to sulfur trioxide (SO₃) gas [15]. As temperatures cool below ~176 °C, the sulfur trioxide forms highly corrosive sulfuric acid (H₂SO₄) [15], [16]. The sulfuric

acid dew point temperature varies based on the sulfuric acid and water concentration within the flue gas. However, it is estimated to occur between 95-150°C [17]. When the flue gas and/or the heat exchanger surface cools below the sulfuric acid dew point the vapor begins to condense on heat exchanger surfaces, subjecting the heat-exchange elements to extremely corrosive operating conditions.

The effect of tube surface temperature on dew point corrosion is illustrated in Figure 2.1. There are two zones of severe corrosion: below the sulfuric acid dew point temperature, and below the water dew point temperature. When the tube surface temperature is just below the sulfuric acid dew point the rate of acid condensation is low, resulting in low corrosion rates. As the tube surface temperature decreases, the rate of condensation increases, leading to increased corrosion rates. The corrosion rate displays a peak at roughly 15-50 °C below the sulfuric acid dew point temperature [2]. At this point, a decrease in corrosion rate is experienced as the surface is sufficiently covered by sulfuric acid and the corrosion rate becomes dependent on the wall temperature [2]. When the surface temperature reaches the water dew point, water vapor begins to condense and combine to sulfur dioxide (SO₂) within the flue gas and forms sulfurous acid (H₂SO₃) [2]. Consequently, the heat exchanger surface becomes exposed to sulfurous acid condensates and a sharp increase in corrosion rates is experienced. It is evident that decreases in surface temperature below the sulfuric acid and water dew point temperatures result in severe increases in corrosion. The first zone, sulfuric acid dew point corrosion, is the main cause of corrosion in low-temperature heat recovery [5], [15], [17], and will be the main corrosive agent investigated for this study.

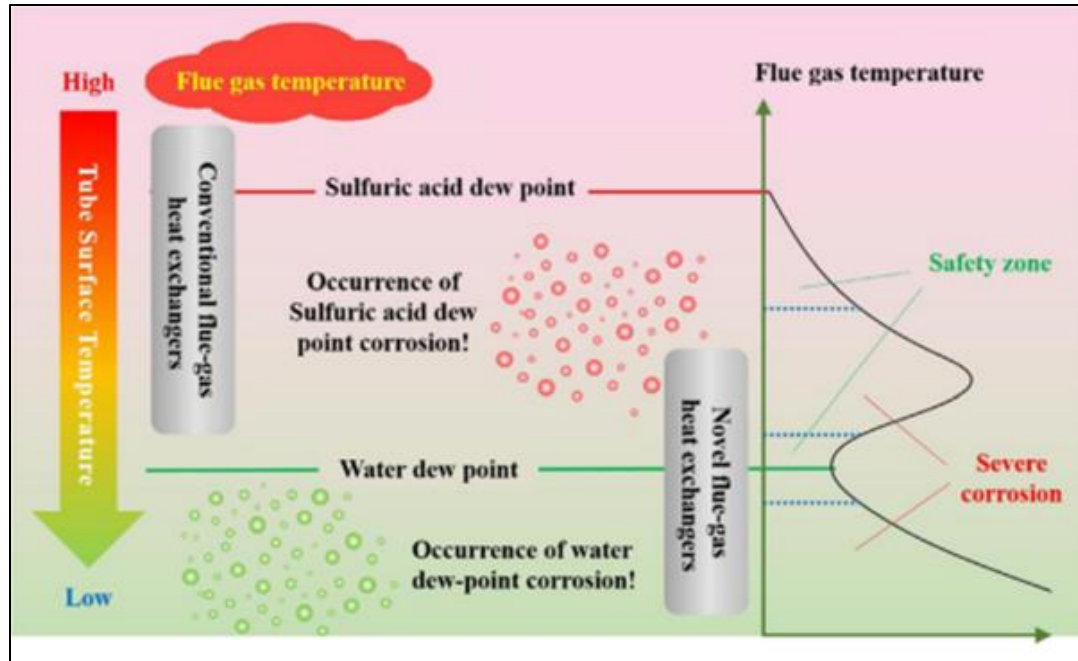


Figure 2.1 The effect of the surface temperature of heat exchange elements on low-temperature corrosion [2].

Naturally, temperature moderation may be one of the first approaches to controlling corrosion in low-temperature heat recovery. Maintaining operating temperatures of both the flue gas and heat-exchange components above the acid dew point may prevent acidic vapors from condensing on the heat exchange surfaces, thus preventing corrosion. Nonetheless, several factors make this approach impractical. The sulfuric acid dew point varies based on the acid and water vapor content within the fuel, which is dependent on the specific fuel source [15]. The heat exchanger geometry, flue gas velocity, and fly ash particle size are additional factors influencing the sulfuric acid dew point, and are unique to each heat-exchange system [18]. Temperature fluctuations during plant start-ups and shut-downs are often unavoidable and may also cause the temperature to fall below the sulfuric acid dew point [19]. Furthermore, cooling the flue gas temperature below the dew point temperature allows both the latent and sensible heat to be obtained, resulting in

substantial energy savings [1], [20]. Considering the challenges associated with accurately predicting the dew point temperature for specific systems, and the economic benefit of cooling flue gases below the dew point temperature, it is critical to design systems capable of withstanding sulfuric acid dew point corrosion.

2.2.2 Corrosion of Metal Heat Exchangers

Metals are typically the preferred material for heat-exchange components due to their high strength, high thermal conductivity, and high operating temperatures [5]. However, common metals such as low carbon steel, aluminum, copper, stainless steel, etc. fail rapidly due to severe chemical attack on the heat-exchange surfaces. The high cost associated with exotic metals (e.g. tantalum, titanium, molybdenum, etc.) and super alloys (e.g. Inconel, Hastelloy, etc.) that can withstand the corrosive operating environments are not economically viable [3], [5]. The following section reviews the failure mechanisms of metal heat exchangers implemented in low-temperature waste heat recovery, and in experimental simulations.

A study conducted by Cheng et al. [21] investigated the suitability of three newly developed low-alloy steels for sulfuric acid dew point corrosion resistance. The low-alloy steels all contained various percentages of each alloying element (Si, Mn, P, S, Cu, Cr, Ti, Ni), and the addition of each element remained below 1 weight percent (wt %) of the alloy's overall composition. The specimens were each immersed in 10, 30, and 50% H₂SO₄ at their corresponding dew point temperatures for 48 hours. Mass loss measurements indicated lowered corrosion rates in all three specimens compared to plain carbon steel, nonetheless mild to severe corrosion was observed on all the samples as revealed by both macroscopic and microscopic evaluations. The severity of failure varied with the specific composition

of the low-alloy steel sample and the concentration of the acid solution. Failure mechanisms included localized pitting, micro-cracking, and build-up of corrosion products. The most severe failure occurred in low-alloy steel sample #1 immersed in 30% H_2SO_4 solution at 50 °C; large (100 μm) pits and microcracks were observed on the surface using a scanning electron microscope (SEM), as shown in Figure 2.2 [21]. When immersed in higher acid concentrations (50% H_2SO_4 , 70 °C) all samples formed a protective layer of corrosion product; the long-term impact of the protective layer on the overall corrosion resistance of the material has not been studied.

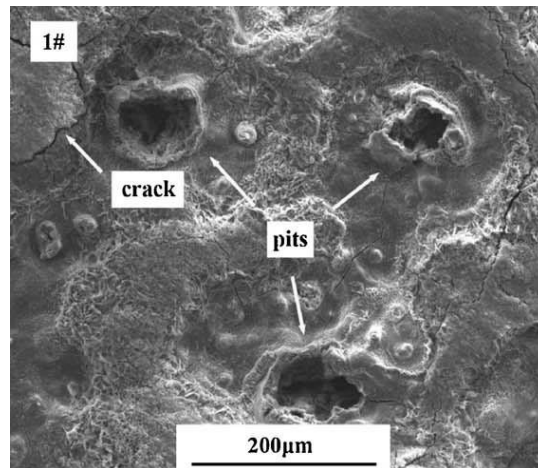


Figure 2.2 SEM image of low alloy steel specimen #1 immersed in 30% H_2SO_4 solution for 48 hours [21].

Ding et al. completed a comprehensive analysis on the repeated failure of low carbon steel (A106 Gr. A) economizer tubes in a low-temperature waste heat boiler [22]. Failure of the heat exchange tubing resulted in leakage, leading to four plant shutdowns for repair within a five-year period. Micro-zone analysis was conducted on the tubing using an SEM equipped with an electron dispersive spectrometer (EDS). Observations revealed thick deposits of corrosion product on the tube surface, and EDS profiles detected the presence of sulfur within the deposits [22]. Further examination of the corrosion products

via x-ray diffraction (XRD) confirmed that the deposits ($\text{Fe}(\text{OH})\text{SO}_4 \cdot 2\text{H}_2\text{O}$) resulted from sulfuric acid dew point corrosion [22]. Thick deposits lower the thermal performance of the heat exchanger, subsequently lowering the tube surface temperature and causing more sulfuric acid to condense on the surface [22]. Corrosion deposits flake as the tube temperature fluctuates due to the difference in thermal expansion from the tube material, and flaking results in shallow pits and thinning of the heat exchanger tube [22]. Thus, the severity of dew point corrosion intensifies over time.

A report by Levy et al. [20] conducted laboratory corrosion tests simulating different scenarios in low-temperature heat recovery to analyze the performance of several candidate heat-exchange tube materials. Mass loss measurements were used as a basis to determine the corrosion resistance, followed by visual inspection to ensure samples did not exhibit localized corrosion. The test materials included: carbon and low-alloy steels, stainless steels, nickel alloys, an aluminum-bronze alloy, aluminum alloys, graphite, and Teflon coatings [20]. It should be noted that the polymer-based material selected for the present research (PFA) was not included in the study. Preliminary corrosion testing in 60% H_2SO_4 at 121 °C determined that the stainless steels (304, 316, AL6XN, 2205), nickel alloy (600), and the aluminum alloys (3003, 6061) are not suitable for low-temperature heat exchanger environments [20]. Further testing indicated that the corrosion resistance of the steels (1018, A387, Corten B) is also inadequate in high acid concentrations and temperatures (80% H_2SO_4 , 150 °C). The nickel alloys (22, 690) and polymer coatings (FEP, PTFE) provided the best corrosion resistance at high acid concentrations, consistent with results previously published by Fontana [23] and Brubaker [24]. Nickel alloy 22 is the preferred metal due to its overall corrosion resistance at high acid concentrations

(corrosion rate of ~0.95 mm/year in 80% H₂SO₄ at 150°C), commercial availability, high yield strength, and high thermal conductivity [20]. The Teflon coatings (FEP, PTFE) exhibited superior corrosion resistance, displaying no visible signs of corrosion during testing at all acid concentrations (60%-80% H₂SO₄). Nonetheless, nickel alloy 22 remains the recommended material due to the low thermal conductivity, low strength, and potential manufacture difficulties of the PTFE coating [20].

The failure of metal heat-exchange components due to dew point corrosion results in repair, replacement, and shutdown of plant operations, all leading to substantial economic losses [22], [25], [26]. It is essential to find an economically viable material for heat-exchange components capable of withstanding the corrosive operating conditions in low-temperature waste heat recovery.

2.2.3 Corrosion Resistant Polymer Coatings

The corrosive operating conditions in low-temperature heat recovery are considered unavoidable [2], thus preventing the selection of low-cost metals due to severe chemical attack and failure of the heat-exchange components. Corrosion resistant coatings have been identified as a viable solution to protect heat exchanger surfaces from chemical attack due to sulfuric acid dew point corrosion. The benefits of coatings are twofold: (i) the temperature may be lowered well below the sulfuric acid dew point as the surface is protected from corrosion, and (ii) cost effective and thermally conductive metals may be used for the base material. Polymers are an attractive coating candidate due to their superior corrosion and fouling resistance [5], [27]. The following section reviews the main benefits, drawbacks, and recent advances of polymer coatings for low-temperature heat exchanger applications.

Initial interest in polymer coatings peaked due to their superior corrosion and fouling resistance, relatively low cost, lightweight, and ease of fabrication [4], [5], [27]. Unlike metals, polymers are typically completely corrosion resistant to a substance, or rapidly deteriorate [28]. Corrosion of polymers normally presents in the form of discoloration, swelling, delamination/blistering, or dissolution of the material into the corrosive solution [28]. The relatively low melting point of polymers is not considered a major barrier as low-temperature heat recovery occurs below $\sim 232^{\circ}\text{C}$, which is within the operating temperatures of several polymers [5]. Research further states that the implementation of polymer coatings promotes dropwise condensation, leading to significant increases in thermal heat transfer performance [29], [30]. Unfortunately, the intrinsically low thermal conductivity of polymers combined with the required thickness of the coatings for adequate corrosion protection often counteracts any benefits from dropwise condensation [31], [32]. Thus, drawbacks of polymer coatings include low thermal conductivity, low strength, and susceptibility to wear.

Early research conducted by Roach and Holtz aimed to identify polymers capable of withstanding sulfuric acid corrosion [5], [33]. Candidate polymers were applied to metal tubes and exposed to sulfuric acid condensates; results indicated that the performance of the coating was dependent on the coating technique, porosity, and thickness [5]. Thin coatings below $50\ \mu\text{m}$ were not sufficient and corrosion of the metal substrate was observed, likely due to defects and/or pores within the polymer coating [5]. Coatings with thicknesses between $100\text{-}500\ \mu\text{m}$ generally performed well, displaying only slight discoloration or blistering [5]. Polyphenylene sulfide (PPS) coatings performed particularly well, showing no discernible signs of corrosion after 5000 hours of immersion

in sulfuric acid [5]. The promising results led to the present research, which aims to optimize the thermal and mechanical performance of polymer coatings for low-temperature heat recovery applications.

The impact of polymers' low thermal conductivity on the thermal performance and overall economics of heat exchanger systems has also generated much interest [27], [34]. Studies conducted by Roach and Holtz focused on polymer-coated heat exchangers [5]. They determined that the impact of the thin polymer coatings on the heat transfer performance is relatively low, comparing the coatings to a thin layer of fouling which is routinely accounted for in heat transfer calculations [5]. They also estimated the cost of polymer-coated heat exchangers relative to corrosion resistant metal tubes. The cost of PPS coated tubes (500 μm thickness) is roughly 8% lower than corrosion resistant Hastelloy tubing [5]. The cost of PPS coated tubes was largely attributed to high labor costs due to a lack of large scale production methods, and is expected to decrease with modern coating techniques [5]. Furthermore, the increased fouling resistance of polymer coated tubes may lower annual maintenance costs [5], [27]. Lastly, Chen et al. reasoned that the thermal conductivity of polymer coatings must be compared to metals with alike corrosion resistance [34]. The thermal conductivity of corrosion resistant metals such as Hastelloy (17 W/mK) and Inconel (12 W/mK) are significantly lower than metals such as copper (391 W/mK) and aluminum alloys (alloy 3003, 169 W/mK) [34], [35]. Thus, the corrosion resistant properties of polymer coatings outweigh the drawbacks of their low thermal conductivity.

2.3 Polymer Composite Coatings

The addition of conductive filler materials to produce polymer composites is another common method to minimize the impact of protective coatings on the thermal performance of heat exchangers [33]. Polymer composites are comprised of the polymer, which may be referred to as the matrix, and one or more filler materials. Filler materials are added to the polymer matrix to increase the thermal performance, strength, and wear resistance of the composite. Several studies on metal [36], [37], carbon-based [38]–[40], and ceramic [41] filler particles have demonstrated improved electrical, thermal, and mechanical performance of polymer composite materials. The following section focuses on polymer composites dedicated to low-temperature waste heat recovery.

2.3.1 Selection of Polymer Matrix

He et al. [6] initiated research on fluoropolymer composite coatings for heat-exchange components exposed to the corrosive operating environments in low-temperature waste heat recovery. Preliminary studies identified perfluoroalkoxy (PFA) as a suitable material as the polymer matrix [6]. PFA is inert to most chemicals [42], has a relatively high operating temperature (~ 260 °C) [14], is commercially available, and is melt-processible [14], [43]. The melt-processability of PFA is particularly advantageous as it allows the formation of pinhole-free coatings using conventional coating methods [6]. Coating methods include electrostatic deposition of dry powder [6], solvent or water-based paint slurry coating technology [44], and flame or torch thermal spray processes [45]. Both electrostatic deposition and paint slurry coating methods must be cured at temperatures above the melting point of the material to set the polymer. Furthermore, the melt-processible nature of PFA allows the formation of relatively thinner coatings compared to

polymers with similar corrosion resistance but not melt-processible, such as Teflon (PTFE) [6]. This results in increased heat transfer performance and cost savings as the amount of material required is reduced.

2.3.2 Recent Advances in PFA-Composite Coatings

He et al. [3] analyzed PFA-based composite coatings and discussed the impact of conductive filler particles on the overall coating performance. Graphite was selected as a filler material due to its high thermal conductivity, excellent corrosion resistance, good wear resistance, and similar density to PFA [3]. The composite powder mixture was prepared by blending 10-50 wt% graphite powder into PFA powder using a tumble mixer for one hour. The powder was then used to make compression-molded disks for thermal property measurements. Electrostatic powder spray was employed to coat the composites onto stainless steel coupons to create coated samples for corrosion, mechanical and tribological testing. A primer powder was also applied to some coupons before the polymer composite top coating to analyze the impact of primer on the coating adhesion strength. Corrosion testing indicated that composite samples with a ~150 μm coating thickness provided adequate protection, while thinner coatings of 45-60 μm exhibited premature failure in the form of blistering [3]. The composite's thermal conductivity increased with increased graphite content, but filler contents greater than 30 wt% resulted in poor surface finish. The addition of graphite filler particles also increased the hardness, elastic modulus, and adhesion of the coating to the substrate. Coating adhesion was further enhanced by the application of the primer layer. Lastly, the electrostatically applied composite coating and primer layer increased the real contact area between the coating and the substrate as compared to the traditional Teflon film covering technologies [3]. The increased real

contact area, combined with the need for thinner coatings and the addition of filler particles, results in significant increases in the overall heat transfer rate [3].

Further research conducted in collaboration with the University of Windsor [7] was performed using various filler particles including: graphite, silicon carbide (SiC), alumina (Al_2O_3), and boron nitride (BN). Filler particle selection focused on identifying materials that would maintain the corrosion resistance of the polymer, while improving the coating properties such as adhesion and resistance to scratch and wear. Composite preparation and testing was consistent with previous work described above [3]. As shown in Figure 2.3, the addition of boron nitride and graphite filler particles resulted in the greatest increases in thermal performance. The thermal performance was analyzed with respect to temperature; all the composites experienced a peak in thermal conductivity at 75 °C, and then decreased with further temperature increases. At 75 °C the boron nitride composite exhibited a thermal conductivity of 2.8 times that of pure PFA. The thermal conductivity of composites may be influenced by several factors such as the thermal conductivity, content, shape, spatial distribution, and orientation of the filler particles within the matrix [7], [36], [46], [47]. Both graphite and boron nitride have lower densities than silicon carbide and alumina, thus the same weight percentage of filler results in higher volume fractions, leading to higher thermal conductivities [7].

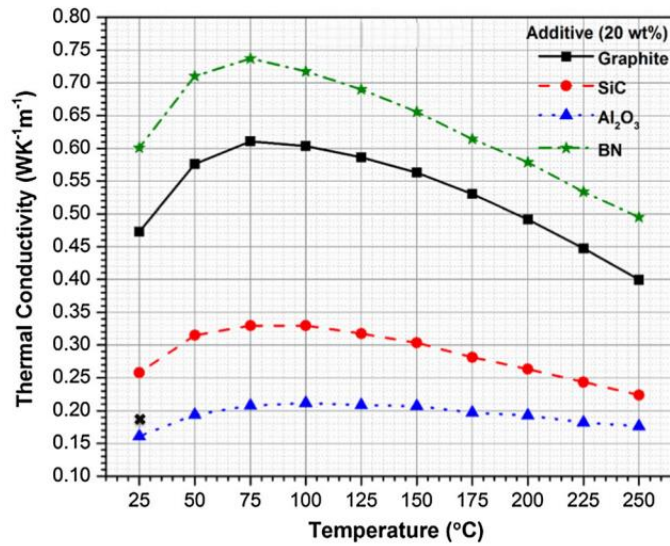


Figure 2.3 Thermal conductivity of PFA composites with respect to temperature (the "x" shows the thermal conductivity of pure PFA) [7].

Microscratch testing with progressive loading (0.03 to 28 N) was also conducted on the composite-coated samples discussed above to characterize the micromechanical properties and modes of failure [7]. Images of the scratch track on the PFA-20 wt% graphite composite coating are shown in Figure 2.4 to illustrate the scratch behavior. At low applied loads, an initial low deformation zone was observed where elastic and viscoelastic recovery prevented visible scratch tracks [7]. At higher applied loads plastic deformation of the coating occurred, resulting in the formation of lateral and frontal material pileups. Tensile stresses build up behind the indenter with increasing applied load [48], leading to failure in the form of micro-cracking (Fig. 2.4b), micro-voids, fibrillation along scratch direction, and delamination (Fig. 2.4c) [7]. Failure typically initiates at the interface between the matrix and filler materials, or imperfections within the matrix such as un-melted PFA particles [7]. The overall performance indicated that graphite and boron nitride filled composites displayed poor adhesion to the substrate and were delaminated at higher loads,

whereas alumina and silicon carbide filled composites exhibited strong interfacial adhesion [7].

The effect of alternating layers of coating composition (plain PFA, PFA-5 wt% graphite, PFA-10 wt% graphite) on the tribological properties of the coating was also investigated [49]. Coated coupons were prepared as outlined in previous research [3], [7]. However, each sample contained multiple layers of varying compositions (i.e. 3 layers of PFA-10 wt% graphite, 1 top layer of plain PFA). The results indicated that samples with graphite in their top layer have roughly 50% lower surface roughness values compared to samples with plain PFA top layers. Furthermore, samples with graphite top layers experienced roughly 30% lower wear rates than samples with plain PFA in the top layer. The effect of higher graphite concentrations in the top layer also increased the wear resistance of the coating [49]. Thus, a top layer of plain PFA decreases the tribological performance of the coating. It is postulated that applying a top layer containing 5-10 wt% graphite may improve the properties of samples that display poor surface finish (30 wt% graphite or higher).

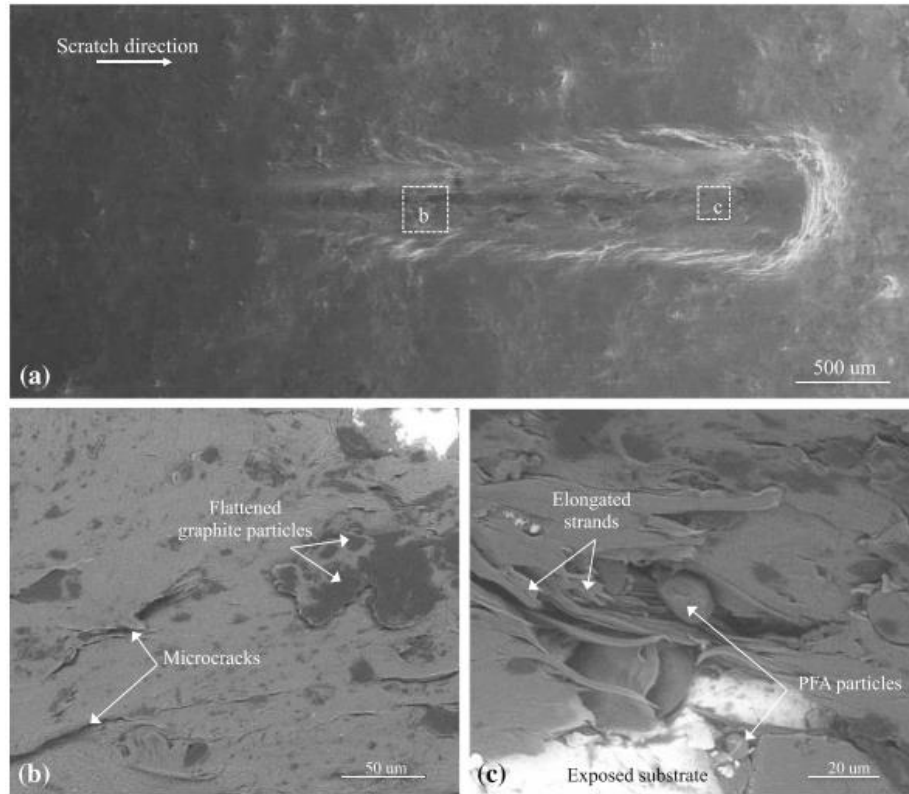


Figure 2.4 SEM images of the PFA-20wt% graphite samples following microscratch testing (0.03 to 28N loading, 3mm length scratch track). (a) Secondary electron (SE) image of the overall scratch morphology, with the enclosed areas illustrated at higher magnification. (b) back-scattered electron (BSE) image of location “b” in Figure 2.4(a) showing micro-crack initiation and flattening of graphite particles. (c) BSE image of location “c” in Figure 2.4(a) displaying failure exposed substrate indicating delamination of the polymer coating, elongated strands along the scratch direction, and un-melted PFA particles [7].

Recent research has focused on studying the suitability of graphene as a filler material in PFA composite coatings. The following sections review the properties of graphene, graphene-polymer composites, and processing methods for to optimize coating performance.

2.4 Graphene, Multi-Layer Graphene, and Graphite Nanosheets

Graphene, a single layer of graphite, has generated much interest in research since it was first successfully produced via mechanical exfoliation in 2004 [50]. By definition, graphene is a single layer of hexagonally arranged sp^2 -bonded carbon atoms, either freely

suspended or adhered to a substrate [51]. The unique structure of graphene provides an excellent electron carrier space, leading to its exceptional electrical [9], [52], and thermal [53] properties. The highest recorded thermal conductivity of single layer graphene is 5300 W/mK [53], far exceeding the thermal conductivity of well-known metal conductors such as pure copper (~400 W/mK) [54]. The primary mode of heat conduction through graphene is via acoustic phonons, the transfer of vibrations within a crystal lattice [54]. Superior phonon transfer is attributed to graphene's strong C-C covalent bonds, mitigating phonon scattering and optimizing heat transfer [52]. Graphene also exhibits superior mechanical properties: studies have reported it as the strongest measured material, i.e. with Young's Modulus of 1 TPa, and ultimate tensile strength of 130 GPa [55], [56]. Analysis of graphene's tribological performance has indicated a low coefficient of friction (COF), and relatively high wear resistance [57]. Furthermore, graphene is proven to be hydrophobic [58], chemically inert [59], and has potential to provide an effective corrosion barrier from chemical attack. Thus, graphene is a promising filler material to enhance the thermal, electrical, mechanical, tribological, and corrosion resistance of composite coatings.

When the number of graphene layers exceeds 1 (monolayer), it is recommended to classify graphene as multi-layer graphene (MLG, 2-10 well defined layers of graphene), or ultra-thin graphite nanosheets (typically less than 100 nm thick) [51]. Common graphene production methods, such as exfoliation of graphite, produce a combination of monolayer graphene, MLG, and graphite nanosheets [60]. MLG retains excellent thermal properties, but the thermal conductivity decreases as the number of graphene layers increases [61]. For instance, when the number of graphene layers increases from 2 to 4, the thermal conductivity decreases from 3000 W/mK to 1500 W/mK [62]. When the number of

graphene layers increases to 10, such as in graphite nanosheets, the thermal properties approach those of bulk graphite [61]. Graphite remains an ideal filler material due to its high thermal conductivity (25-470 W/mK) [63], [64], lubricating properties, and corrosion resistance to most chemicals [3], [6], [7]. The proper distinction between graphene and graphene-based materials (MLG, and graphite nanosheets) is necessary due to the variations in material properties. Despite the above recommendations, literature often refers to MLG as “graphene”; as such, the thickness of graphene should also be reported.

2.5 Graphene-Polymer Composites

The addition of graphene and graphene-based filler materials is a proven method to enhance the thermal [65]–[67], electrical [68]–[70], and mechanical [71], [72] properties of polymer-composite materials and coatings. This new area of research has led to the development of materials for a variety of applications, including strong lightweight polymer composites for the automotive and aerospace industry, and thermally conductive composites for thermal management systems in the electronic industry [52]. Two recent studies have analyzed PFA-graphene composites for potential use in low-temperature heat recovery applications [8], [73].

A recent study conducted by the University of Windsor and CanmetMATERIALS developed and analyzed the impact of graphene nanoplatelets (GNPs), and multi-walled carbon nanotubes (MWCNTs) as filler materials in PFA composite coatings [8]. Two different grades of graphene nanoplatelets (AO2-grade: 8 nm thickness/~22 layers, ~5 μ m lateral flake size; AO4-grade: 60 nm thickness, \leq 7 μ m lateral flake size) were selected to investigate the impact of GNP thickness on the composite performance. The composite powder mixture was prepared by blending 1-20 wt% filler material with PFA followed by

processing to create compression-molded disks and coated coupons, similar to the procedures previously reported by He et al. [3], [7], [8].

Microscopy was conducted on the compression-molded disks and coating cross-sections to analyze the filler distribution [8]. A matrix of interconnected GNPs was observed within the PFA matrix of the compression-molded disks for both grades of graphene. Conversely, the coating cross-section did not display any interconnection of the GNPs, and segregation of the filler particles was observed [8]. However, the discrepancy in filler dispersion may have been exaggerated due to differences in the microscope magnifications (the coating was analyzed at a much higher magnification). Microscopy of the samples containing MWCNTs revealed agglomeration of the filler particles in both the compression-molded disks and coating cross-sections, resulting in poor surface finish of the coating [8]. Composite disks were also used for thermal property measurements. The addition of GNPs resulted in greater increases in the composites' thermal performance, displaying a maximum thermal conductivity of 1.6 W/mK (20 wt%, both grades of GNPs); whereas the MWCNTs displayed a maximum value of 0.5W/mK (20 wt%) [8].

The coated coupons were analyzed for corrosion resistance, wear properties, and coating adhesion [8]. Corrosion testing showed minor mass gains and/or losses in all of the tested composites however, the MWCNT-filled composites displayed visible signs of corrosion (discoloration) [8]. Thus, MWCNT samples did not satisfy the long-term requirement for corrosion resistance and did not undergo further testing. Microscratch testing on the GNP-filled composites indicated excellent coating adhesion for both grades of graphene as no delamination occurred [8]. Pin-on-disk wear testing was conducted on the GNP-filled composites at both ambient and elevated (200 °C) temperatures to

characterize the wear behavior. Lower wear rates were observed at elevated temperatures. Ambient testing resulted in well-defined wear tracks, whereas elevated temperature testing resulted in less pronounced wear tracks with irregular edges [8]. Elevated temperatures at the point of contact between the coating and counter-face material [74] resulted in softening of the polymer, producing the irregular track edges [8]. At ambient temperature, the 8 nm-grade graphene experienced slightly lower wear rates as compared to the 60 nm-grade. Smaller filler particles result in stronger bonds between the filler and matrix, leading to increased hardness and wear resistance [75], [76]. Recorded COF values were higher during testing at ambient temperature, but remained within the range for PFA on steel [8][42]. Nonetheless, the slightly higher thermal and wear performance of the 8 nm-grade GNPs does not justify the much higher cost, thus the 60 nm-grade GNPs are the preferred filler material for low-temperature heat exchanger composite coatings [8].

A study conducted by Zhang et al. also developed and characterized PFA-graphene composites [73]. Few-layer graphene (1-3 layers) was ultrasonically treated to prevent aggregation and improve filler dispersion within the polymer matrix [73]. The composite powder mixture was hot pressed into composite disks for subsequent testing. Thermal property measurements revealed a maximum thermal conductivity of 5.017W/mK (20 wt% graphene), 20× higher than pure PFA. A positive relationship between graphene dispersion and thermal conductivity was observed; longer sonication times resulted in increased filler dispersion and higher thermal conductivities [73]. Reciprocating wear testing was conducted to analyze the composites tribological behavior. The COF gradually increased with increased graphene content, increasing from 0.0313 for pure PFA to 0.0334 for 15 wt% graphene [73]. The addition of graphene decreased the wear rate of samples up to 10

wt%, attributed to the lubricating properties of graphene forming a protective transfer film [73], consistent with previous studies on MWCNT polymer composites [77]. Further increases in graphene content above 10 wt% resulted in increased wear rates, presenting in the form of material peeling and the formation of wear debris [73]. Increased wear rates may be attributed to an aggregation of graphene particles and non-uniformity within the matrix resulting in weak regions susceptible to wear [73].

The addition of graphene filler materials is an effective method to improve the thermal performance and wear resistance of PFA-composite materials, while maintaining their corrosion resistance and substrate adhesion as coatings. It is evident that the performance of PFA-graphene composites, particularly the thermal performance, may be influenced by the graphene quality, quantity, and filler incorporation technique employed.

2.5.1 Factors Limiting the Thermal Performance of Graphene-Polymer Composites

Phonons are considered the primary mode of heat transfer in graphene [54], polymers [78], and graphene-polymer composites. As previously discussed in section 2.4, the unique structure of graphene allows for the rapid transmission of lattice vibrations, resulting in excellent thermal performance. In polymers the diffusion of heat occurs much slower, this may be attributed to disordered vibrations and rotation of atoms within the molecular chains as vibrations transfer from one atom to the next [11], [12]. When graphene is added to a polymer matrix, several interfaces are created between the graphene-polymer surfaces. These interfaces result in large interfacial thermal resistances; heat transfer experiences a bottleneck effect at the interface between the graphene and the polymer material due to the slower diffusion rates displayed by the polymer [79]. This effect is illustrated by Burger et al. in Figure 2.5 [12]. The interfacial thermal resistance

leads to phonon scattering, and decreases the heat transfer performance of the composite [11].

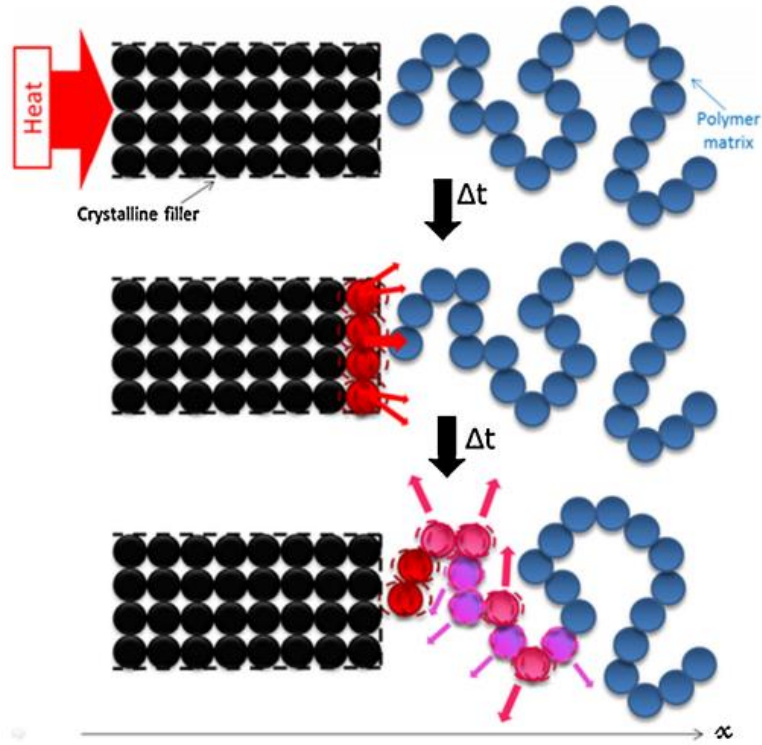


Figure 2.5 Schematic of thermal conductive mechanisms at the interface between graphene and polymer materials [12].

The efficiency of phonon energy transfer may be impacted by the method used to incorporate filler materials. Surface modification of graphene particles is a proven method to decrease interfacial thermal resistance, and improve the thermal performance of the composites [10], [11], [80], [81]. This reduces the interfacial thermal resistance by the formation of an interlayer that promotes phonon transfer between the graphene and polymer interfaces [11]. Studies have shown that incorporating filler materials via ball milling increases filler compatibility within the matrix, and reduces interfacial thermal

resistances [10], [82]–[85]. Thus, ball milling was selected as a filler incorporation method for the work presented in this thesis.

Phonon scattering is directly influenced by filler particle dimensions: fillers with small lateral dimensions have higher interface densities, directly correlating to increases in phonon scattering [86]. Shtein et al. comprehensively analyzed the effect of GNP thickness, lateral dimension, and defect density in GNP-polymer composites [86]. When comparing samples with similar layer thickness (~13 nm), those with larger lateral dimensions (~20 μm versus ~10 μm) repeatedly displayed better thermal performance [86]. The results also indicated that samples with higher defect densities displayed lower thermal conductivities [86], consistent with similar research focused on the increase of phonon scattering at graphene defects [87]. Higher thermal conductivity values were also observed in samples with larger thickness values (15-100 nm versus 9-20 nm), and similar lateral dimensions (~20 μm) [86]. This may be attributed to the interface density: to achieve the same volume fraction of filler particles more “thin” particles will be required, resulting in a higher interface density. These results are supported by several studies reporting an increase in thermal performance with larger GNP thickness and lateral dimensions [86], [88], [89].

The thermal conductivity of graphene-polymer composites is also influenced by the filler loading; higher percentages of graphene filler yield higher thermal conductivities [8], [86]. The thermal percolation threshold, the point at which thermal transport mainly occurs through a conduction pathway of interconnected filler materials, remains a debated topic in materials research [86], [90], [91]. Conversely, the electrical percolation threshold is clearly observed in graphene-polymer composites, as electrical conduction only occurs through the percolation network [90]. However, graphene-polymer composites conduct

heat regardless of the percolation threshold. Therefore whether the contribution of heat conduction is through the percolation network or through the matrix remains unknown [90]. Furthermore, some results indicate that thermal percolation thresholds (~30 vol%) occur at higher filler loading fractions than electrical percolation (~10 vol%) [90]. The filler loading value was previously determined as a limiting factor for PFA-graphite composites, as the coating surface finish becomes compromised at filler additions greater than ~20 wt% [3]. Thus, achieving thermal percolation is not a main purpose of this study.

The thermal performance of graphene-polymer composites is also influenced by the directional properties of graphene. Multi-layer graphene displays directional thermal properties. As previously discussed, graphene displays superior in-plane thermal conductivity resulted from the strong covalent bonds between carbon atoms [11], [53]. However, the out-of-plane thermal conductivity is significantly reduced as phonon scattering occurs at the weak van der Waals forces between graphene layers [11], [92]. Orienting graphene particles in the direction of the heat flux is a proven method to increase the thermal conductivity of the composite [11], [93], [94]. Magnetic functionalization of graphene particles is a proven technique to orient graphene fillers within a polymer matrix [13], [95]. Thus, filler alignment by magnetic functionalization was the second filler incorporation method selected for the work presented in this thesis.

2.5.2 Graphene Incorporation via Ball Milling

Ball milling has been identified as an efficient processing technique to increase compatibility of conductive filler materials within polymer matrices, yielding significant increases in the thermal performance of composites [10], [82]–[85]. This technique is of

particular interest in graphene-based filler materials as ball milling is reported to simultaneously: (i) exfoliate graphite to produce few-layer graphene; (ii) improve filler compatibility and interfacial resistance at the graphene polymer interface; and (iii) thoroughly combine the matrix and filler materials to create a homogenous mixture [10], [84], [96], [97].

Graphene production is generally divided into two main approaches: bottom-up, or top-down [98]. The top-down approach depends on the exfoliation of graphite and has demonstrated potential for cost efficient large-scale production of graphene [98]. Studies have shown that wet ball milling is an effective graphite exfoliation method; it involves dispersing graphite in a solvent, followed by grinding in a ball-mill containing grinding media for a set speed and length of time [98]–[101]. Zhao et al. suggest using a relatively low milling speed of 300 rpm to reduce intense shocks potentially damaging the graphite structure, and ensure shear stress is the dominant exfoliation mechanism [101]. Teng et al. describe the importance of using both large (2 mm) and small (0.2 mm) zirconium oxide (ZrO_2) grinding media to further promote the exfoliation of graphene sheets from large graphite particles through shear force [99]. Solvent selection is also an important factor for graphene exfoliation; solvents with similar surface tensions to graphene are more effective in enhancing graphene exfoliation [99], [102].

Wu et al. introduced a novel approach to use wet ball milling to exfoliate graphite into GNPs in the presence of polymer matrix solution, which simultaneously creates a homogenous polymer-graphene composite *in situ*, as shown schematically in Figure 2.6 [84]. This process is proven to disperse GNPs within the polymer matrix, and increase GNP compatibility within the matrix via strong interfacial interaction with the polymer

[10], [84], [96], [97]. Furthermore, newly exfoliated GNPs are wrapped in polymer matrix, preventing re-agglomeration and protecting the GNP structure [10].

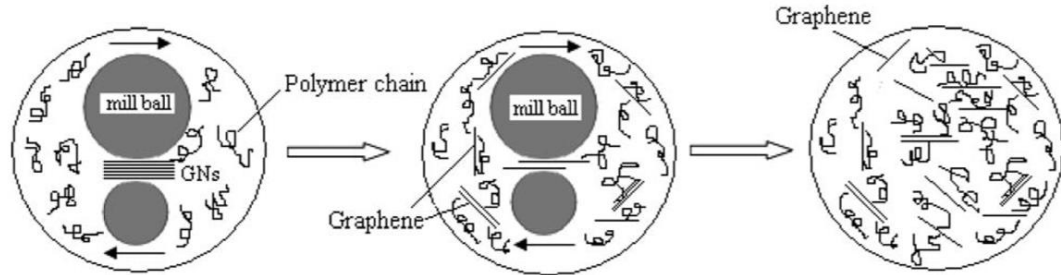


Figure 2.6 Schematic of the ball milling process incorporating the graphene and polymer powders [97].

Liu et al. produced GNP-epoxy composites using an enhanced ball milling method, and the results indicated increased mechanical performance. With 0.1 wt% GNPs the ultimate tensile strength (UTS) and Young's modulus of the composite increased 160% and 65%, respectively, as compared to pure epoxy [96]. At filler loading greater than 0.2 wt% the UTS and Young's modulus begin to level out, likely due to the reduced cross-linking density that weakens the epoxy [96], [103]. Similarly, the hardness of the composite reached a maximum of 50% increase at 0.5 wt% GNPs. Increases in the mechanical properties were due to the superior mechanical properties of graphene, and to the strong interfacial bond between the GNPs and epoxy matrix [96].

The enhanced ball milling method for polymer composite preparation has also demonstrated increases in both electrical and thermal properties. Composites prepared by ball milling displayed an electrical percolation threshold at 5.0 wt%, compared to 13.0 wt% in composites prepared by a traditional sonication technique [97]. Furthermore, the thermal conductivities of ball-milled samples were double those prepared by traditional sonication

mixing [10]. The GNP-epoxy composite reached a maximum thermal conductivity of 2.67 W/mK at 25 wt% of GNP, a 1422 % increase as compared to pure epoxy [10]. Studies also indicated that ball milling time was a critical factor influencing the composite's thermal performance. Composites containing 20 wt% GNPs displayed maximum thermal performance after 24 hours of ball milling [10]. Thermal performance increased with milling times from 0 to 24 hours, as longer milling times resulted in higher GNP yield. However, after 24 hours additional milling resulted in structural defects within the GNPs, restricting further increases in thermal performance [10].

SEM and high-resolution transmission electron microscopy (HRTEM) were conducted to study the microstructure of microtomed samples. SEM images of the ball-milled sample revealed uniformly dispersed GNPs and excellent adhesion at GNP-polymer interfaces. Conversely, the sonicated sample contained several GNP agglomerates, and flaking at GNP-polymer interfaces [10]. Unlike SEM, HRTEM may be used to identify the number of layers in GNP samples, directly indicating the extent of exfoliation [10], [85], [96], [97]. The extent of graphene exfoliation is further validated through Raman spectroscopy [10], [84], [96]. The Raman spectra of graphene exhibits three main peaks; changes in the peak shape, position, and intensity may indicate the number of graphene layers (after 10 layers, the spectra becomes indistinguishable from bulk graphite) [104]. Through both HRTEM and Raman analyses, several studies confirmed the successful exfoliation of MLG (1-10 layers) in polymer composites through the enhanced ball milling technique [10], [84], [96].

2.5.3 Graphene Incorporation via Magnetic Functionalization

Graphene filler materials exhibit superior in-plane thermal properties, while the performance in the out-of-plane direction is inferior [53]. Studies have proven that improved thermal performance in graphene-polymer composites may be achieved by aligning graphene particles in the direction of heat flux [12], [13], [95]. Wu et al. also reported improvements in electrical performance by aligning graphene particles in an epoxy composite; the electrical conductivity increased 7-8 orders of magnitude, and the percolation threshold was lower than randomly oriented composites [105]. Furthermore, graphene displays superior in-plane mechanical properties, leading to increases in UTS, Young's modulus [106], and overall fracture toughness in composites containing aligned graphene [93], [105].

Magnetic functionalization is a proven technique to orient thermally anisotropic nano-filler materials such as boron nitride [107], [108], carbon nanotubes [109], [110], and graphene [13], [95], [111] in polymer composites. Magnetically responsive graphene particles are incorporated into the polymer matrix and aligned by applying an external magnetic field to orient particles during curing. Magnetic alignment is a facile [95], [111], economically viable and scalable approach [13], with the potential for implementation in coating applications [109].

Balandin et al. applied a unique polymer wrapping technique (PWT) and layer-by-layer (LBL) self-assembly process to attach magnetic nanoparticles onto the graphene surface through non-covalent interactions, as illustrated in Figure 2.7 [13]. This approach was first applied to carbon nanotubes; the non-covalent attachment of nanoparticles demonstrates unique advantages as it preserves the structure and the associated electrical

and thermal properties of the material [112], [113]. The process begins by dispersing graphene in an aqueous solution of poly(sodium 4-styrene sulfonate) (PSS) [13]. The PSS acts as a wrapping polymer and serves as a negatively charged primer for the subsequent adsorption of the cationic poly-dimethyl-diallylammonium chloride (PDDA) [13], [112], [113]. The negatively charged PDDA layer ensures the final adsorption of the magnetic nanoparticles through electrostatic interactions [13], [112], [113]. The resulted magnetically functionalized graphene particles were incorporated into an epoxy matrix, and subjected to a magnetic field during curing to facilitate graphene alignment [13].

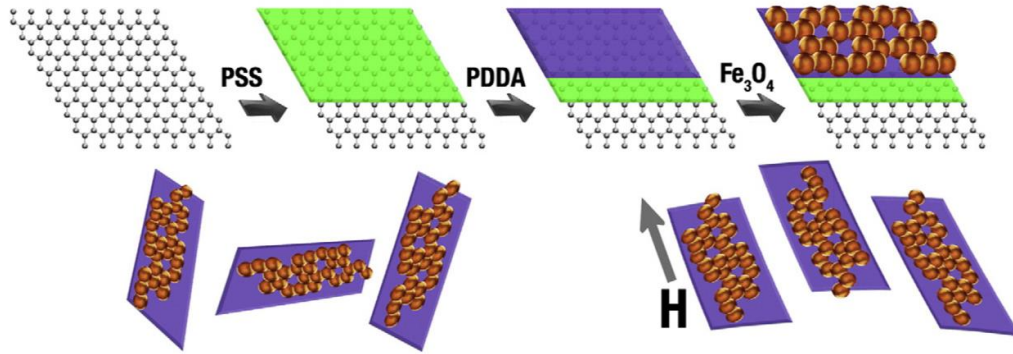


Figure 2.7 Schematic illustration of graphene magnetic functionalization process [13].

Optical microscopy and TEM were conducted on the resulted graphene-epoxy composites; attachment of magnetic nanoparticles was observed through TEM, and graphene filler alignment was clearly confirmed through optical microscopy [13]. Thermal conductivity measurements were conducted to analyze the thermal properties; at 1 wt% loading, the oriented graphene fillers display an apparent thermal conductivity 2× greater than randomly oriented fillers [13]. Apparent thermal conductivity accounts for thermal contact resistances of connecting surfaces, thus greater enhancements would be expected for bulk material [13].

Studies have shown excellent corrosion resistance of magnetically functionalized graphene (graphene-Fe₃O₄) composites in water and aqueous sodium chloride solutions [114], [115]. However, the corrosion resistance of magnetically functionalized graphene in highly acidic environments, such as sulfuric acid, remains unknown. The present study aims to identify if the proposed method, alignment of graphene fillers via magnetic functionalization, leads to increases in the thermal performance of PFA-graphene composites. Future studies regarding the corrosion resistance of graphene-PFA composites containing magnetic nanoparticles are recommended if the present study is successful in improving thermal performance.

CHAPTER 3: MATERIALS AND EXPERIMENTAL METHODS

The methodology is composed of three steps: (i) filler incorporation, (ii) sample preparation, and (iii) sample analysis, as summarized in Figure 3.1. Filler incorporation was conducted by two different methods (ball milling, and magnetic functionalization); both methods produced a blended powder mixture containing 1-20 wt% graphite/graphene filler and PFA. The blended powder mixtures were used to prepare disk samples through compression molding and to coat stainless coupons through electrostatic spraying. Sample analysis of the compression-molded disks included microscopy, thermal property measurements, and Raman spectroscopy. Analysis of the electrostatically coated coupons included microscopy, surface topography, and wear testing. Both (i) filler incorporation and (ii) sample preparation were conducted at CanmetMATERIALS, and (iii) sample analysis was conducted at the University of Windsor.

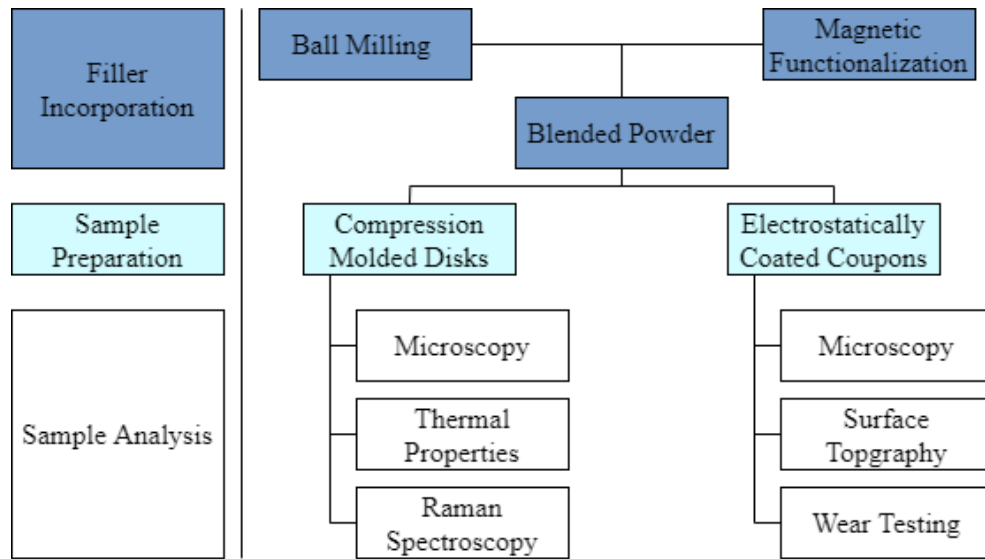


Figure 3.1 Schematic illustration of the experimental methods and procedures used in this research, divided into three steps: filler incorporation, sample preparation, and sample analysis.

3.1 Bulk Materials

The materials used in this study include NEOFロン PFA powder (AC-5600 grade, Daikin America Inc., NY), two forms of graphite (~ 9 μ m, and ~ 44 μ m particle size), and multi-layered graphene (~60 nm thickness, \leq 7 μ m lateral size; Graphene Supermarket). Selected properties of the PFA and filler materials are listed in Table 3.1.

Table 3.1 Selected properties and dimensions of PFA and graphite filler materials [42], [64], [116].

Property	PFA (AC-5600)	Graphite (4014 Grade, Asbury Carbon)	Graphite (Alfa Products)	MLG (AO-4 Grade)
Particle Size/ Thickness	~44 μ m	9.01 μ m	44 μ m	60 nm
Lateral Size	N/A	N/A	N/A	\leq 7 μ m
Thermal Conductivity	0.19 W/mK	25-470 W/mK	25-470 W/mK	25-470 W/mK
Density	2.12-2.17 g/cm ³	2.09-2.30 g/cm ³	2.09-2.30 g/cm ³	2.09-2.30 g/cm ³
Corrosion Resistance	Excellent	Excellent	Excellent	Excellent
Cost (CAD)	~\$57 /lb	~\$31 /lb	~\$17 /lb	~\$1474 /lb

Additional materials were purchased specifically for the magnetic functionalization process. Ferric chloride (FeCl₃), ferrous sulfate (FeSO₄), ammonium hydroxide (28-30 wt% NH₄OH aqueous solution), tetramethylammonium hydroxide solution (25 wt% C₄H₁₃NO aqueous solution), Poly(sodium 4-styrenesulfonate) (PSS powder, M_w= ~70 000), and poly-(diallyldimethylammonium chloride) (20 wt% PDDA aqueous solution, M_w= 400 000-500 000), were all purchased from Sigma Aldrich. Hydrochloric acid (36.5-38 wt% HCl aqueous solution) was acquired from Fisher Scientific. Lastly, according to related literature, Milli-Q water (~18.2 M Ω) was used for the PWT and LBL self-assembly processes [117].

3.2 Filler Incorporation Methods

3.2.1 Ball Milling

Ball milling was conducted in a Retsch Planetary Ball Mill PM 100 (Germany) at various filler weight fractions, initial filler particle sizes, and milling times to analyze their effects on the thermal properties of the resulted composites. The degree of mechanical exfoliation of the filler particles may vary based on the initial size of the graphite particles used, and the overall milling time. The ball milling schedule, including filler type, weight percentage, and overall milling time, is listed in Table 3.2.

The PFA powder and 5-20 wt% filler material were dispersed in acetone via sonication for 0.5 hour at room temperature. A 3:1 ratio of acetone to composite powder was used. Sample quantity and ball charge were determined based on the Retsch Mall Mill recommendations for wet grinding. A sample quantity of 80 mL (acetone and composite powder solution) was added to a 250 mL stainless steel grinding jar, with approximately 150 mL (550 g) of zirconium oxide (ZrO_2) grinding media [118], [119]. The remaining volume is essential to permit the free movement of grinding media during milling. A 1:1 mass ratio of small and large diameter (~0.2 mm, 3 mm) ZrO_2 grinding media were used to ensure the exfoliation of graphite through shear force [10], [99]. The solution was ball milled at a speed of 300 rpm for 5-30 hours, according to the schedule in Table 3.2.

Following ball milling, the solution was poured over a sieve coupled with a sieve shaker and thoroughly rinsed with ethanol to separate the composite powder mixture and milling media. The composite powder mixture was then placed in an oven at ~60 °C overnight to remove the acetone and ethanol solvent. The dried composite powder mixture was processed through a 300 μ m sieve to break down any agglomerates formed during

drying; the resulted composite powder mixture was then ready for sample preparation. Between ball milling procedures, the grinding media was sonicated for 0.5 hour, thoroughly washed with a neutral detergent, rinsed with water and ethanol, and dried.

Table 3.2 Schedule of ball milling experiments: time, filler type and weight percentage.

Filler	Graphite (~9 μ m particle size)			Graphite (~44 μ m particle size)			Multi-Layer Graphene (60nm thickness)			
	wt. (%)	10	15	20	10	15	20	10	15	20
Milling Time (hours)	25	25	5	25	25	25	25	25	25	20
			10							20
			15							25
			20							30
			25							
			30							

A portion of the blended powder mixture with the 9 μ m graphite particles (20 wt% filler, 25 hours milling time) underwent additional processing. An extra sample was prepared by “diluting” the 9 μ m graphite blended powder mixture (20 wt% filler, 25 hour milling time) with unprocessed PFA powder to create a sample with 10 wt% filler (20 wt% filler “diluted” to 10 wt% filler with unprocessed PFA). The “diluted” powder mixture was blended in a laboratory Inversina Tumbler Mixer (Bioengineering Inc.) at room temperature for 1 hour. The 9 μ m graphite sample may be compared to an “undiluted” sample with 10 wt% filler to analyze the impact of ball milling on the PFA particles i.e., better tribological performance of the diluted sample may indicate that the ball milling process damaged the PFA particles.

Lastly, to establish a baseline for comparison, blended powder mixtures were created with each graphite filler type and wt% without ball milling. Filler particles were incorporated by mixing in the Inversina Tumbler Mixer for 1 hour.

3.2.1.1 Naming System for Ball Milled Samples

To clearly identify specific ball-milled samples, the following naming system is used: graphite type – filler wt% – processing time. For example, the PFA polymer composite sample containing 10 wt% 9 μm graphite filler ball milled for 25 hours will be referred to as: 9 μm -10wt%-25h. The 20 wt% 9 μm graphite sample diluted to 10 wt% filler will have an ‘M’ added at the beginning to indicate that the sample contains a mixture of both processed and unprocessed PFA (M9 μm -10wt%-25h).

3.2.2 Magnetic Functionalization

The MLG magnetic functionalization process consists of two main steps: preparation of magnetic nanoparticles, and the PWT and LBL self-assembly process to attach the magnetic nanoparticles onto the MLG surface. The magnetic nanoparticles (Fe_3O_4 - γ - Fe_2O_3) were synthesized through the co-precipitation of ferric and ferrous ion solutions, according to Massart’s method and related literature [112], [117], [120]. A ferric/ferrous mixture was created by combining 1 mole (M) FeCl_3 (20 mL, in water) and 2 M FeSO_4 (5 mL, in 2 M HCl solution) [117], [120]. The ferric/ferrous mixture was added to 0.7 M NH_4OH (250 mL, in water), and underwent rapid mechanical stirring using a magnetic stirring rod for 30 minutes [117], [120]. Following stirring, the magnetic nanoparticles (Fe_3O_4 - γ - Fe_2O_3) were precipitated. The precipitate is collected via magnetic decantation and re-dispersed in distilled water (50 mL). A stable alkaline solution of negatively charged magnetic nanoparticles is created by adding three aliquots of 1 M $\text{C}_4\text{H}_{13}\text{NO}$ (10 mL, in water) to the precipitate solution, under rapid mechanical stirring [117], [120]. Water is added to the final solution up to a total volume of 250 mL [117].

The PWT and LBL self-assembly process is completed in compliance with the methods used in related literature [13], [112], [113], [117]. The PWT is conducted by creating a 1 wt% PSS solution (1 L, in Milli-Q water), and dispersing MLG (Trial one: 0.15 g, Trial two: 2 g) in the solution by a combination of mechanical mixing, and sonication for 30 minutes [117]. The PSS-MLG solution is stored at 50 °C for 12 hours to ensure the adsorption of the negatively charged PSS onto the MLG surface [117]. Excess PSS is removed by three centrifugation and re-dispersion cycles [117]; the solution is centrifuged at 5000 rpm for 1.5 hours, and re-dispersed in Milli-Q water by brief sonication. The quantity of graphene was increased from 0.15 g in Trial one to 2 g in Trial two to investigate if the process can achieve a higher yield of magnetically functionalized MLG (MF-MLG).

The positively charged PDDA layer is subsequently added by mixing 1 wt% PDDA solution (1 L, in 0.5 M NaCl aqueous solution) with the PSS-coated MLG via sonication for 30 minutes [117]. Excess PDDA is removed by three centrifugation and re-dispersion cycles, as specified above. The final layer of magnetically functionalized nanoparticles is added by dispersing the PSS-PDDA coated MLG in 0.2 M NaCl (750 mL), and incorporating the negatively charged magnetic nanoparticle solution (250 mL) by mechanical stirring using a magnetic stirring rod for 1 hour [117]. The solution underwent another three-centrifugation and re-dispersion cycles as specified above to remove excess magnetic nanoparticles. As described in Section 2.6, the adsorption of each layer (PSS, PDDA, and magnetic nanoparticles) occurs through the electrostatic interactions between positive and negatively charged layers [13], [112].

The final solution was heated to $\sim 100\text{ }^{\circ}\text{C}$ while stirring with a magnetic stirring rod to evaporate the remaining water, followed by drying in an oven ($\sim 60\text{ }^{\circ}\text{C}$) overnight. The dried MF-MLG particles were processed through a $300\text{ }\mu\text{m}$ sieve to break down any agglomerates formed during drying. The MF-MLG particles were exposed to an external magnetic field to ensure that the particles are magnetically responsive, shown in Figure 3.2. Lastly, blended powder mixture was prepared by mixing the PFA powder with the MF-MLG particles (1 wt% and 10 wt% filler, based on the graphene content) in a laboratory Inversina Tumbler Mixer at room temperature for 1 hour. The determination of graphene content is described in Section 3.2.2.1 below.

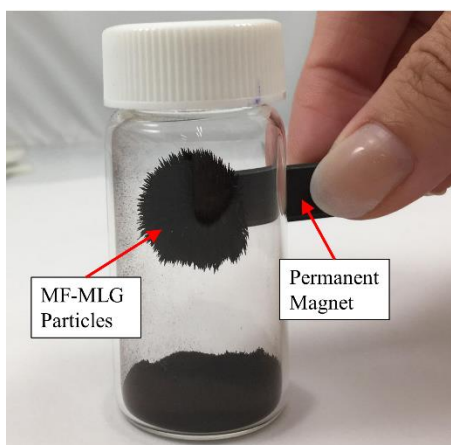


Figure 3.2 Photograph of the dried MF-MLG particles attracted to an external magnetic force. The MF-MLG particles produced from both trial 1 and trial 2 were magnetically responsive.

3.2.2.1 Determination of Graphene Content in MF-MLG

During magnetic functionalization, graphene is coated by PSS, PDDA, and finally magnetic nanoparticles. Therefore, the coated graphene particles weigh more than the uncoated graphene particles. Calculation of graphene content is important when comparing MF-MLG composites to composites containing regular (not functionalized) graphene. The graphene content in the MF-MLG particles is calculated, and the MF-MLG is added to the

PFA composite such that the composite contains the desired wt% graphene (i.e., a composite containing 1 wt% graphene may require 10 wt% MF-MLG filler depending on the graphene content). It is assumed that no graphene is lost during processing. The mass of MF-MLG produced is compared to the mass of graphene added to the mixture, as shown in Table 3.3.

Table 3.3 Calculation of the graphene content in the produced MF-MLG.

	$m_{\text{graphene added}}$	$m_{\text{MF-MLG produced}}$	$\text{wt\%}_{\text{graphene}} = \frac{m_{\text{graphene added}}}{m_{\text{MF-MLG produced}}} \times 100$
Trial 1	0.15 g	1.48 g	10.14 %
Trial 2	2 g	3.98 g	50.25%

The amount of MF-MLG added to a composite containing 1 wt% graphene and 10 wt% graphene is then calculated based on Equations 3.1a and 3.1b, respectively. Due to the extremely low yield of graphene in the MF-MLG powder produced from trial 1, a PFA composite containing only 1 wt% graphene was studied. Trial 2 produced a significantly higher yield of graphene, thus composites with a higher filler weight fraction (10 wt%) were studied.

$$m_{\text{MF-MLG, 1wt\%}} = \frac{m_{\text{composite}} \times 0.01}{\text{wt\%}_{\text{graphene}}} \quad (3.1a)$$

$$m_{\text{MF-MLG, 10 wt\%}} = \frac{m_{\text{composite}} \times 0.1}{\text{wt\%}_{\text{graphene}}} \quad (3.1b)$$

3.2.2.2 Naming System for Magnetically Functionalized Samples

To clearly identify the magnetically functionalized samples, the following naming system is used: graphite type (MF-MFG) – quantity of graphene added during functionalization (Trial 1: 0.15 g, or Trial 2: 2 g) – filler wt%. The filler wt% denotes the wt% of graphene in the composite. For instance, the PFA polymer composite sample

containing 1 wt% MF-MFG filler (based on graphene content) produced from Trial one (0.15 g graphene added during functionalization) will be referred to as: MF-MFG-0.15g-1wt%.

3.3 Sample Preparation Process

3.3.1 Compression-Molded Disks

The blended powder mixtures were loaded into a cylindrical die to form compression-molded disks (\varnothing 31.75 mm \times 2 mm). The die was wrapped with an electrical band heater to heat the powder during molding. The formation of defect-free disks was achieved by following the compression molding scheme reported in a previous study [7], as shown in Figure 3.3(a). An initial pressure of 0.4 MPa was first applied to the die at room temperature to compact the loaded powder. The temperature was then gradually increased to 350 °C to melt the polymer; and the pressure was increased to 10 MPa to remove air bubbles that might form during the melting process. The temperature and pressure was maintained at 350 °C and 10 MPa for 18 minutes, then the die (with the disk sample inside) was cooled to room temperature and the sample was removed from the die.

Disk sample preparation for the MF-MLG composite used the same temperature and pressure during compression molding. However, additional measures were taken to align the MF-MLG particles. A new die made of non-magnetic stainless steel was fabricated to prevent the magnetization of the die. The MF-MLG composite blended powder mixture was loaded into the die, pressurized to the initial pressure of 0.4 MPa, and then placed on a permanent magnet (K&J Magnetics, N52-grade) for 5 minutes to facilitate

filler alignment, as shown schematically in Figure 3.3(b). The die was carefully removed from the magnet, and the compression molding process was continued as described above.

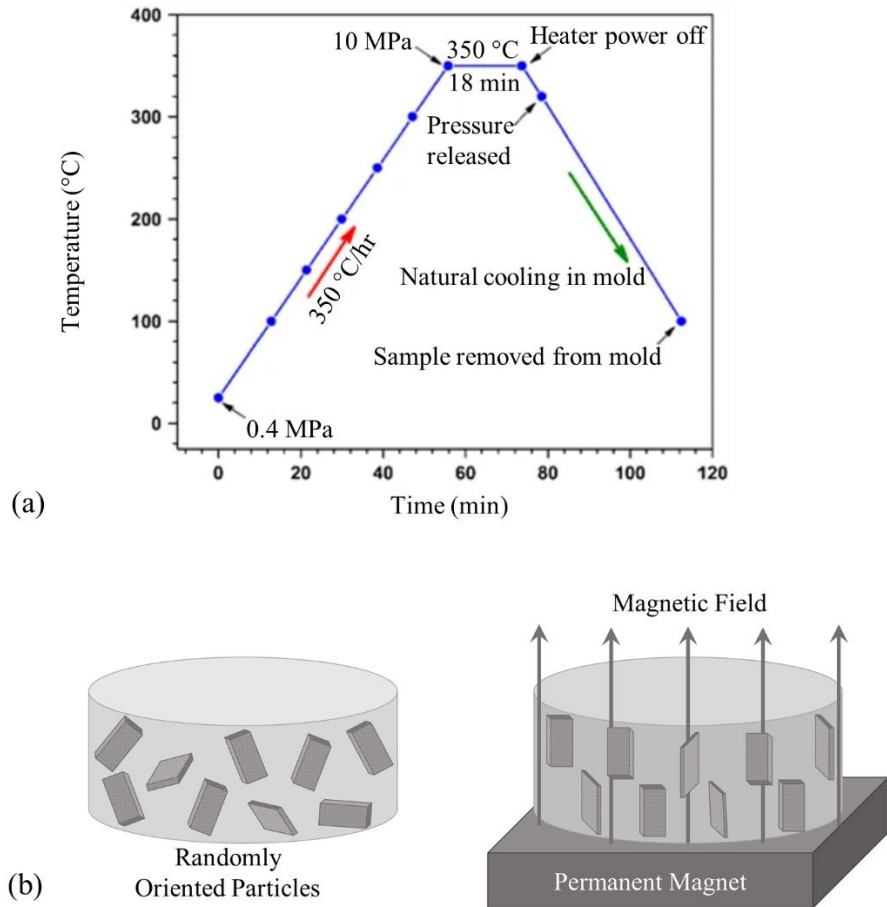


Figure 3.3 (a) Curing scheme for the compression-molded disks [7], and (b) schematic of magnetic alignment of filler particles in composite disk.

Waterjet was used to section the compression-molded disks into smaller pieces for thermal property measurements and microscopy, as shown in Figure 3.4a. Thermal property measurements require smaller disks for the laser flash method (\varnothing 12.7 mm \times 2 mm), and differential scanning calorimetry (\varnothing 6 mm \times 2 mm). Lastly, a small (2 mm \times 2 mm \times 15 mm) piece was cut for microscopy (Fig. 3.4b).

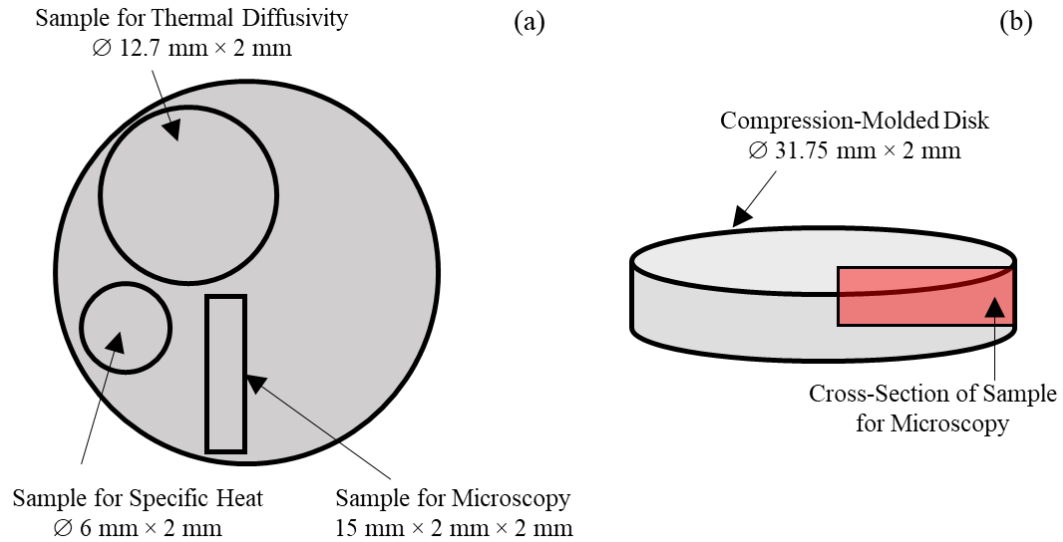


Figure 3.4 Schematic of the compression molded samples: (a) waterjet cutting schemes, and (b) cross-section of the samples for microscopy.

3.3.2 Electrostatically Sprayed Coupons

The blended powder mixtures were also electrostatically applied to 316 stainless steel coupons to create coated samples for testing. This was completed for selected powder mixtures including: ball-milled samples containing 60 nm MLG (60nm-20wt%-25h), 9 μm graphite (9 μm -20wt%-25h, 9 μm -10wt%-25h, M9 μm -10wt%-25h), 44 μm graphite (44 μm -20wt%-25h), and a sample containing magnetically functionalized MLG (MF-MLG-2g-10wt%). The MLG and graphite samples with 20 wt% were selected for comparison with previous studies [3], [7], [8], and a 25 hour ball milling time was selected to focus on the impact of ball milling on the coating performance. The filler produced from Trial 2 (MF-MLG-2g filler) was selected for creating the coating as it produces a significantly higher yield of MF-MLG particles, which is required for the electrostatic spray coating process. Furthermore, the MF-MLG particles produced from both processes were responsive to an external magnetic field as shown in Figure 3.2.

Waterjet was used to cut coupons ($50 \times 25 \times 3$ mm) from a large stainless steel sheet; a small hole (\varnothing 5 mm) was made at the top of the coupons to facilitate the spray coating process. The sharp edges and corners of the coupons were removed by grinding. The coupons were then sandblasted, and thoroughly washed with neutral detergent and dried.

The coupons were coated on one side or both sides during the spray coating process. Electrostatic spray was conducted using a Wagner Prima (Wagner International AG, Switzerland) coating system. The coupons were first coated with a primer powder (ACP-5909 BK, Daikin American, Inc.) to form a $50 \mu\text{m}$ primer layer, and cured in a furnace following the curing scheme identified in previous research, as shown in Figure 3.5a [7]. Top coatings of the blended powder mixtures were then applied up to a total thickness of $150\text{-}250 \mu\text{m}$ (5-7 layers) and cured in a furnace. The MF-MLG composite samples were placed on top of a permanent magnet (K&J Magnetics, N52-grade) for 5 minutes to facilitate alignment of filler particles before curing each layer, as shown schematically in Figure 3.5c.

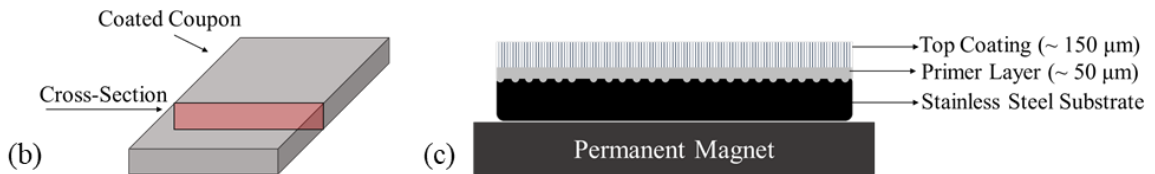
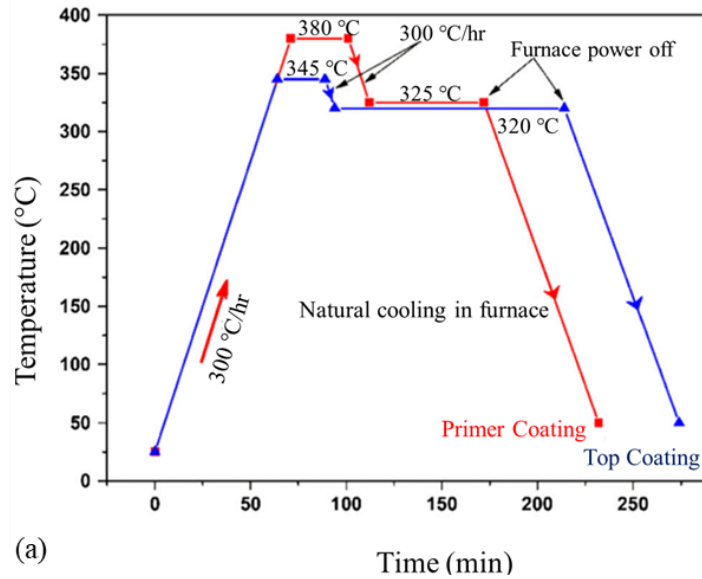


Figure 3.5 (a) Curing scheme for electrostatically coated primer powder and blended powder mixtures [7], (b) schematic illustration of the coating cross-section, and (c) schematic illustration of the cross-section of the primer and top coating layers, and the magnetic alignment of MF-MFG filler particles within the top-coat layer.

3.4 Sample Analysis Methods

3.4.1 Microscopy

3.4.1.1 Sample Preparation for Microscopy

Compression-molded disks and electrostatically coated coupons were prepared as described in Section 3.3. A small piece of each of the compression-molded disks (2 mm × 2 mm × 15 mm) was cut using waterjet and mounted in epoxy for microscopy (cross-section exposed, Fig. 3.4b). A small section of the electrostatically sprayed coupons (~15 × 25 × 3 mm) was cut using a wire electrical discharge machine (WEDM, 0.254 mm wire) and mounted in epoxy for microscopy (cross-section of coating and stainless steel substrate

exposed, Fig. 3.5b). Significant grinding was performed at 180 grit to ensure complete removal of any damage from sample cutting. The samples were then carefully ground using an incremental grit scheme from 180P, 320P, 400P, 600P, 800P, 1500P, 2500P, and 4000P. Lastly, the samples were polished using 1 μm diamond suspension to remove remaining scratches. Samples were rinsed with soapy water, ethanol, and dried between each grinding stage to prevent the transfer of grinding particles between steps.

3.4.1.2 Microscopy and Image Analysis

Microscopy was performed on the polished samples using an optical/ laser scanning microscope (Keyence, VK-X100 series). Three micrographs were taken at 500 \times magnification at different locations for each sample. Scanning electron microscopy (SEM), equipped with an x-ray dispersive spectrometer (EDS), was also performed on the uncured blended powder mixtures to observe changes in the graphite and PFA particles resulted from ball milling, and to analyze the morphology of the MF-MLG particles.

Subsequent analysis of the filler particle distribution within both the compression molded disks and electrostatically coated coupons was performed using the ImageJ software. The software converts the micrographs to a 'binary mask', producing an image featuring the filler particles in black, and the matrix area in white [121], [122], as shown in Figure 3.6. The scale must be set within the Image J software corresponding to a known distance, such as the scale bar automatically produced during microscopy, to ensure accurate measurements. The 'analyze particle' function was then selected, and a summary file is produced containing a quantitative analysis of the filler particle area percent [121], [122]. This process is repeated for three micrographs (taken at different locations) per

sample, and the average results were reported. Particle analysis of the electrostatically coated samples excluded the area containing the ~50 μm primer layer and stainless steel substrate.

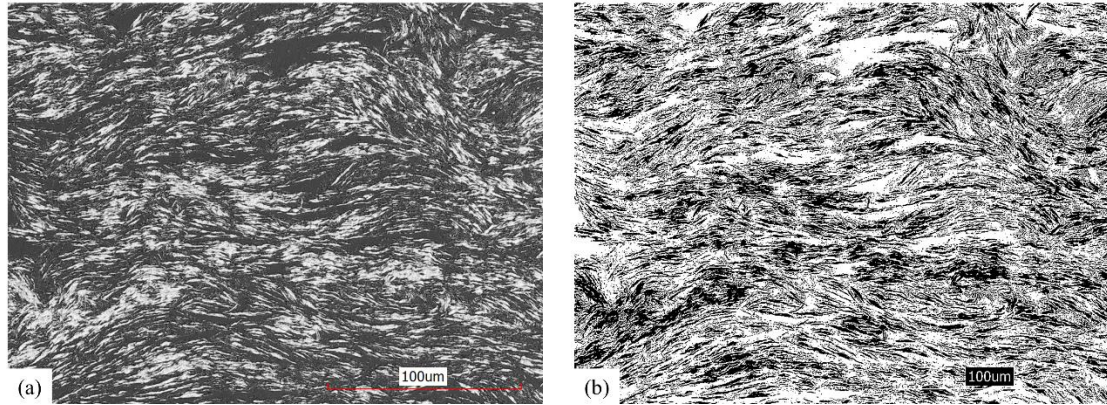


Figure 3.6 (a) Micrograph of the PFA composite with 20 wt % 60 nm MLG filler ball milled for 25 hours (60nm-20wt%-25h), and (b) the micrograph produced using the ImageJ software by applying a binary mask.

3.4.2 Surface Topography

The surface topography of the electrostatically coated samples was examined using an optical/laser scanning microscope (Keyence, VK-X100 series) before durability testing. Three micrographs (100 \times magnification, 1000 \times 1400 μm^2 area) were taken per sample at different locations. The VK Analyzer software was then used to analyze the arithmetic mean height surface roughness (R_a) and root mean square roughness (R_q). The average value from the three micrographs was reported.

3.4.3 Thermal Property Analysis

The compression-molded disks are used for the thermal property measurements. This provides an understanding of the bulk thermal properties of the composite material,

which is consistent with techniques used in related research [3], [7], [8]. The thermal diffusivity measurements were conducted via the laser flash method (LFA 457 Microflash, Netzsch) according to ASTM E1461-01 [123]. The specific heat measurements were performed by the differential scanning calorimetry technique with sapphire as the reference material (ASTM E1269-11) [124]. The values are measured between 25 °C and 250 °C, at 25 °C intervals. The thermal conductivity (λ) is then calculated based on the relationship between the density (ρ), specific heat (C_p), and thermal diffusivity (α) of the composite material [125]:

$$\lambda = \rho C_p \alpha \quad (3.2)$$

3.4.4 Wear Testing

The durability and tribological performance of the electrostatically coated coupons was analyzed via pin-on-disk wear testing. A stainless steel ball was selected as the counter-face material and was positioned perpendicular to the flat test sample (coated coupon). The stainless steel ball was rigidly held in position and the coated sample was securely mounted onto the base of the machine. The machine base rotates the coupon, resulting in a circular sliding pattern at the point of contact with the stainless steel ball. The stainless steel ball and coated coupons were cleaned prior testing. The coated samples were carefully cleaned with soapy water, rinsed, and dried. The mirror-like stainless steel balls were ultrasonically cleaned in ethanol and dried. The samples were weighed before and after testing to the nearest 0.0001 g using a Sartorius LE225D scale. All samples were handled with gloves to prevent contamination.

Ball-on-disk wear tests were conducted at ambient conditions against 6 mm diameter stainless steel balls using a Bruker's UMT machine. The applied load and sliding speed were 10 N and 0.1 m/s, respectively, and each test ran for a total of 8 hours (4.05 mm radius). Wear test parameters were selected according to the procedure outlined in ASTM G99-05 [126] and related literature [3][127].

3.4.4.1 Wear Test Analysis

The Bruker's UMT tribometer recorded the tangential force (F_T) and normal force (F_N) during each test. This data is analyzed to calculate the coefficient of friction (COF, $\mu = F_T/F_N$), and is subsequently plotted to illustrate the COF fluctuations with respect to sliding distance. The average COF in the steady state region is estimated.

Micrographs of the wear track were captured using an optical/laser scanning microscope (Keyence, VK-X100 series). To ensure accuracy, four micrographs at different locations were taken per sample (Figs. 3.7 a, b). The VK-Analyzer software is used to analyze the micrographs to extract the wear track profiles and the corresponding wear area. Six profiles were extracted from each micrograph (Fig. 3.7c), and then the average wear area from all 24 profiles was used for further calculations. The volume wear rate was then calculated as [128]:

$$\tilde{W} = \frac{2 \pi r A}{S} \quad (3.3)$$

where 'r' is the radius of the wear track, 'A' is the average worn area, and 'S' is the total sliding distance.

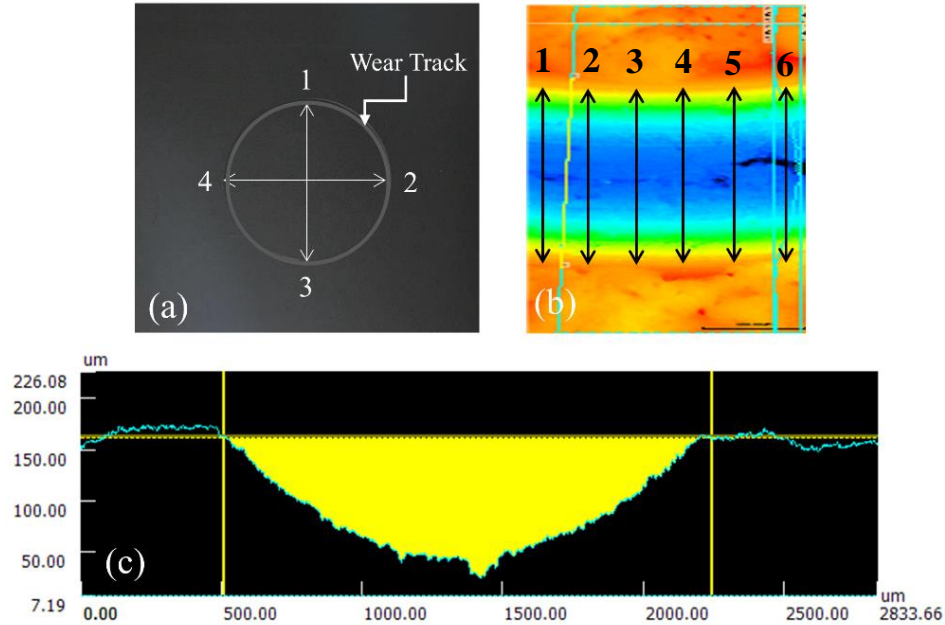


Figure 3.7 (a) Schematic of the wear track, with micrographs taken at the 4 locations indicated. (b) Micrograph of the wear track, with wear profiles extracted at the 6 locations indicated, and (c) A wear profile taken at 1 of the 6 indicated locations.

The wear tracks were further examined using an environmental scanning electron microscope (ESEM, FEI-Quanta 200FEG) with an x-ray dispersive spectrometer (EDS) detector. Low vacuum (~70 Pa) was used to reduce the effect of charging on the surface during imaging.

3.4.5 Raman Spectroscopy

Raman spectroscopy was completed on the compression-molded disks made from the ball-milled composites to analyze the degree of mechanical exfoliation on the graphite particles. Raman spectroscopy is a non-destructive vibrational technique that detects specific ‘fingerprints’ for different geometric structures and bonding within molecules [129]. Changes in the Raman spectra may be analyzed to distinguish between graphene and graphite particles [129]. Raman spectroscopy was conducted using a Confocal Raman

Spectrometer with a 532 nm laser excitation (2 MW laser power, 2 second integration time, 20 accumulations), over a Raman Shift range of 900 – 4000 cm^{-1} wavenumbers. Graphene exhibits three main peaks: a D peak at $\sim 1350 \text{ cm}^{-1}$, a G peak at $\sim 1580 \text{ cm}^{-1}$, and a 2D peak at $\sim 2700 \text{ cm}^{-1}$ [10]. The resulted Raman Spectra were analyzed using Project FOUR software to determine specific peak locations, intensities, and to overlay and compare spectra from different samples.

It is well known that the 2D band of graphene and graphite display notable differences in both their band shape and intensity, as shown in Figure 3.8a [104], [130]. Graphene displays one distinctive 2D band that has a significantly higher intensity than the G peak; conversely the 2D band of graphite is much broader and has a lower intensity than the G peak. The gradual evolution of the 2D band from monolayer graphene to graphite is illustrated in Figure 3.8b; after about 10 layers the Raman spectra of MLG becomes indistinguishable from that of bulk graphite [104], [130].

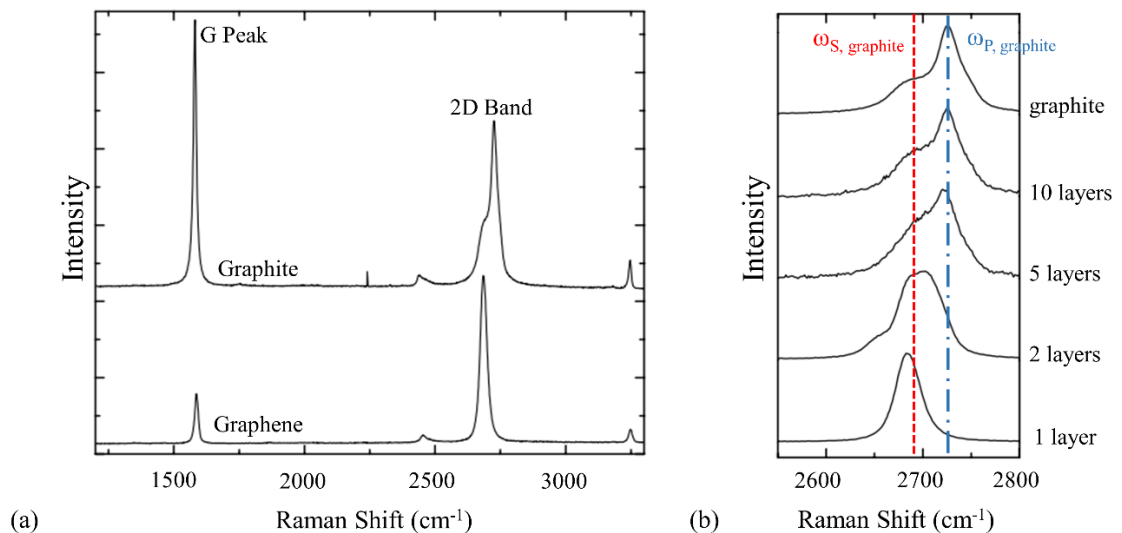


Figure 3.8 (a) The Raman spectra (514 nm excitation) of graphene compared to bulk graphite, with the main peak locations marked, and (b) The Raman spectra (514 nm excitation) of the 2D band as it evolves from monolayer graphene to bulk graphite, with the shoulder (red) and peak (blue) locations labelled (graphs reproduced from Ferrari et al. [130]).

Paton et al. suggested a method to quantitatively estimate the number of graphene layers based on the shape of the 2D band of graphene relative to the shape of the 2D band of the bulk graphite material [131]. This method will be used to estimate the resulted flake thickness of the ball milled graphite particles. First, the ratio of the graphene 2D peak intensity versus the graphite 2D peak intensity is calculated, known as metric ‘M’ [131]:

$$M = \frac{I_{2D,graphene}(\omega=\omega_{P,graphite}) / I_{2D,graphene}(\omega=\omega_{S,graphite})}{I_{2D,graphite}(\omega=\omega_{P,graphite}) / I_{2D,graphite}(\omega=\omega_{S,graphite})} \quad (3.4)$$

where $I_{2D,graphene}(\omega=\omega_{P,graphite})$ is the Raman intensity of graphene at the graphite 2D peak location, $I_{2D,graphene}(\omega=\omega_{S,graphite})$ is the Raman intensity of graphene at the graphite 2D peak shoulder location, $I_{2D,graphite}(\omega=\omega_{P,graphite})$ is the Raman intensity of the graphite at its 2D peak, and $I_{2D,graphite}(\omega=\omega_{S,graphite})$ is the Raman intensity of graphite at the shoulder of its 2D peak [131]. The graphite peak and shoulder locations are indicated in Figure 3.8b. The graphite shoulder is located at: $\omega_S = \omega_{P,graphite} - 30 \text{ cm}^{-1}$ [131]. The number of graphene layers (N_G) is directly related to metric ‘M’ [131]:

$$N_G = 10^{0.84 M + 0.45 M^2} \quad (3.5)$$

Graphene samples containing defects exhibit a D-band, commonly known as the disorder or defect band. The defect intensity ratio (intensity of the D-band relative to the G band, I_D/I_G) may be used to indicate the level of defects in a graphene sample [10], [131], [132]. A higher defect intensity ratio means there are more defects within the graphene, leading to increased phonon scattering and lower thermal performance. The resulted graphene/graphite particles are analyzed at 3 different locations per sample. The average N_G and I_D/I_G ratio calculated based on the three locations is reported in the results.

CHAPTER 4: EXPERIMENTAL RESULTS

The experimental results are presented in five sections: microscopy, surface topography, thermal properties, wear, and Raman spectroscopy.

4.1 Microstructural Analysis

The microstructural analysis is divided into four categories: laser/optical microscopy of the compression-molded disks and electrostatically sprayed coupons, particle analysis using the ImageJ software, and scanning electron microscopy of the blended powder mixtures.

4.1.1 Microstructural Analysis of Compression-Molded Disks

Micrographs of the compression-molded disks (cross-sections) captured using a laser/ optical microscope are shown in Figures 4.1 – 4.5. The micrographs highlight the effect of ball milling on the filler particle shape and distribution with increasing ball milling times, and with different filler particle types (60 nm MLG, 9 μm graphite, 44 μm graphite). To establish a baseline for comparison, the ball-milled samples are all compared to a sample prepared by traditional processing methods (blended in a tumbler mixer for 1 hour). In the micrographs the graphite particles appear as light gray flakes, and the PFA matrix appears black.

The cross-sections of the compression-molded composites containing 20 wt% 60-nm MLG filler are shown in Figure 4.1, comparing the microstructure of the sample without ball milling (Figs. 4.1 a, c) to the sample after ball milling for 25 hours (Figs. 4.1 b, d). The micrographs of the samples without ball milling are from previous research [8]; it is important to note that the high magnification micrograph (Fig. 4.1c) is of an

electrostatically sprayed coupon rather than a compression molded disk. At both high and low magnification, it was observed that the sample that underwent no ball milling has uneven particle distribution, showing large portions of PFA with no MLG particles, and an overall random orientation of the MLG particles within the PFA matrix. Conversely, the filler particles in the ball-milled sample appear evenly distributed and oriented horizontally within the sample. At high magnification (Figs. 4.1 c, d), no obvious changes in the size of the filler particles after ball milling are observed. However, it is important to note that minor particle stacking is observed between some of the MLG particles in the ball milled sample. At low magnification (Figs. 4.1 a, b) the filler particles appear smaller after ball milling; this is likely due to filler particle agglomeration and networking observed in the sample without ball milling.

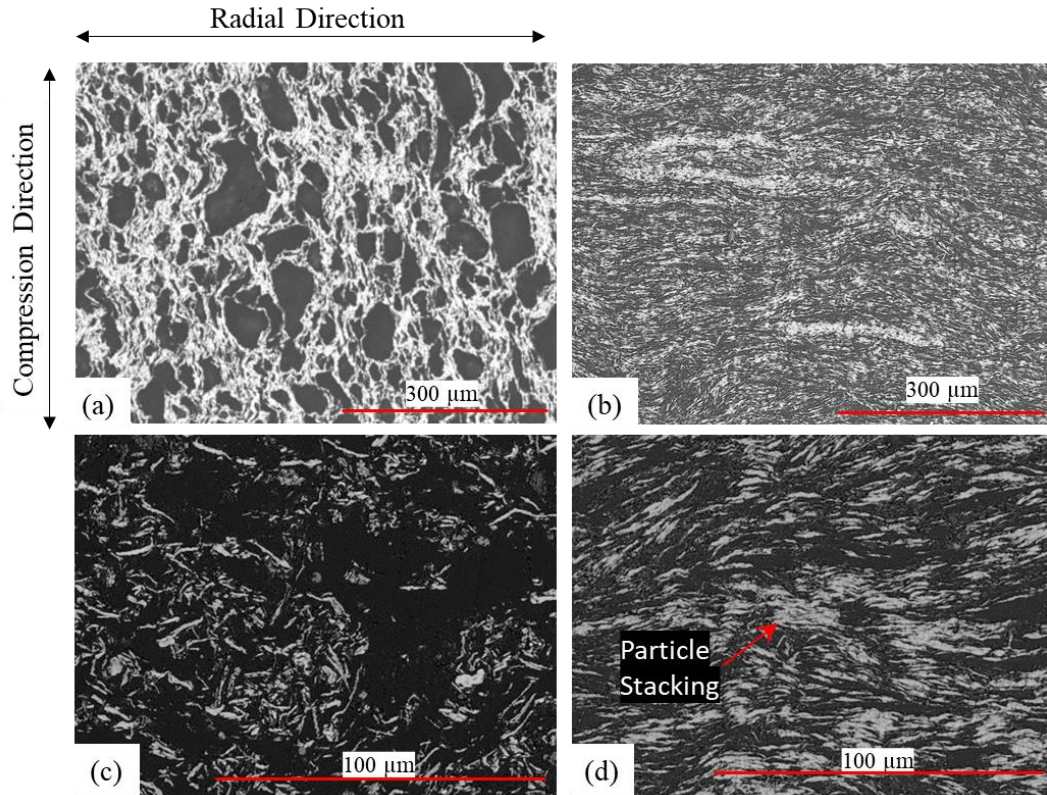


Figure 4.1 Laser/optical micrographs of the PFA- 60 nm MLG composite samples: (a) 60nm-20wt%-0h at low magnification [8], (b) 60nm-20wt%-25h at low magnification, (c) 60nm-20wt%-0h at high magnification [8], and (d) 60nm-20wt%-25h at high magnification. It is important to note that all the micrographs are of compression molded disks except Figure 4.1c, which is an electrostatically coated coupon.

Figure 4.2 compares the cross-sectional micrographs of the PFA composite samples containing 20 wt% 9- μm graphite filler. Samples with various milling times (0 – 30 hours, 5 hour intervals) are compared to evaluate the impact of ball milling time on the filler particles and the resulted microstructure. Consistent with the 60nm-20wt%-0h sample, the 9 μm -20wt%-0h sample without ball milling (Fig. 4.2a) appears to have an uneven distribution of filler particles and random particle orientations. After 5 hours of ball milling (Fig. 4.2b) the graphite particles appear to be oriented horizontally within the sample, with improved particle distribution. No obvious change in the filler particle size or distribution is observed when the ball milling time is increased to 10 hours or more (Figs. 4.2c-4.2g).

All the ball-milled samples maintain good filler particle distribution, with a common orientation of graphite particles along the horizontal direction. Similar to the 60nm-20wt%-25h sample, minor particle stacking is observed between some of the 9- μ m graphite particles in the ball milled samples (Figs. b, c, f).

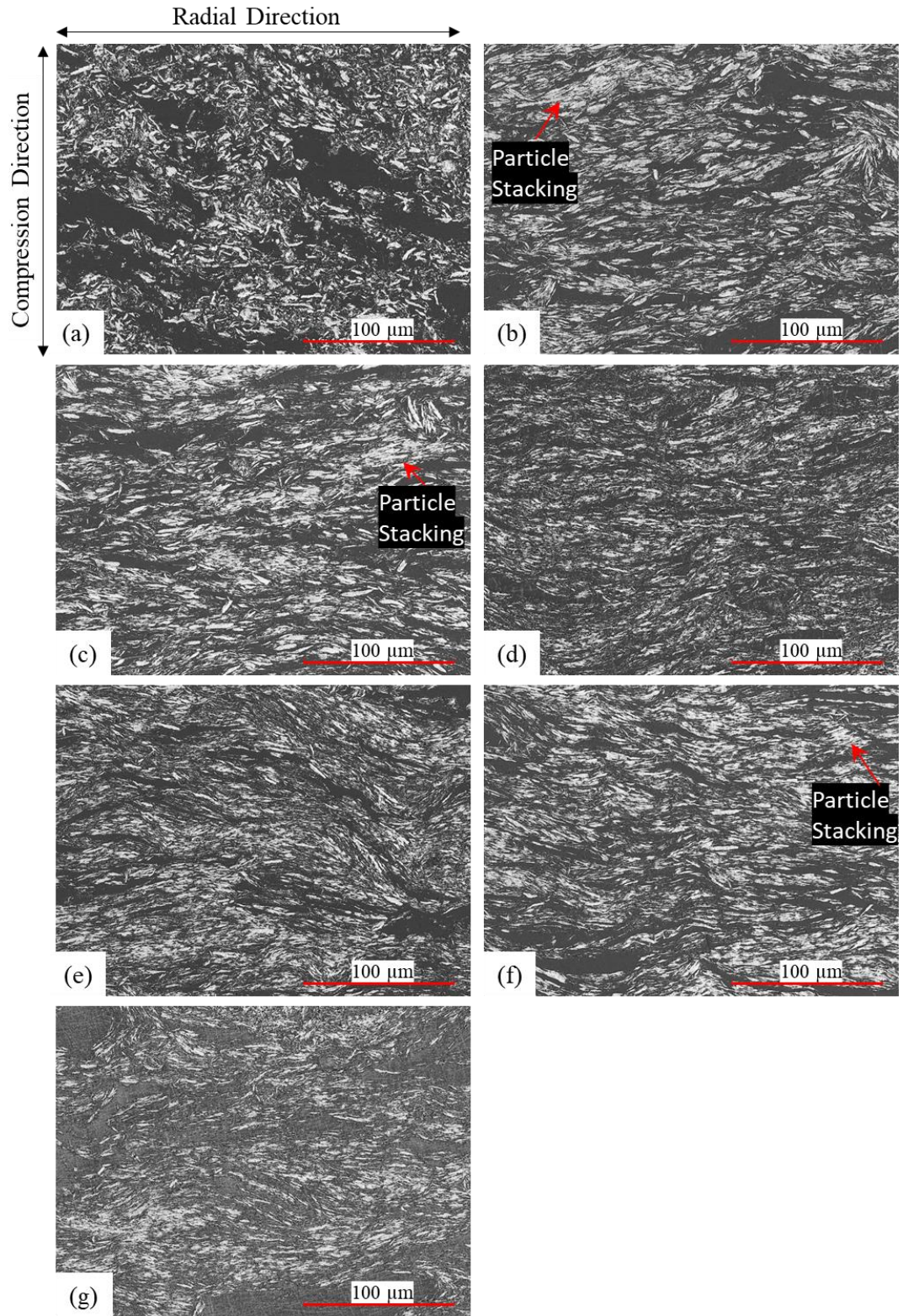


Figure 4.2 Laser/optical micrographs of the PFA- 9 μm graphite composite compression molded samples containing 20 wt% filler with increasing ball milling times: (a) 0 hours, (b) 5 hours, (c) 10 hours, (d) 15 hours, (e) 20 hours, (f) 25 hours, and (g) 30 hours.

The cross-sectional micrographs of the PFA composite samples containing 20 wt% 44 μm graphite are shown in Figure 4.3. The 44- μm graphite has the largest particle size among the fillers studied and shows the most significant change in particle size after ball milling. The sample without ball milling (Fig 4.3a) exhibits randomly oriented, unevenly distributed, and inhomogeneous graphite flakes in the matrix. After ball milling for 25 hours (Fig 4.3b) the graphite particles appear evenly distributed, horizontally aligned, and are more homogeneous in size.

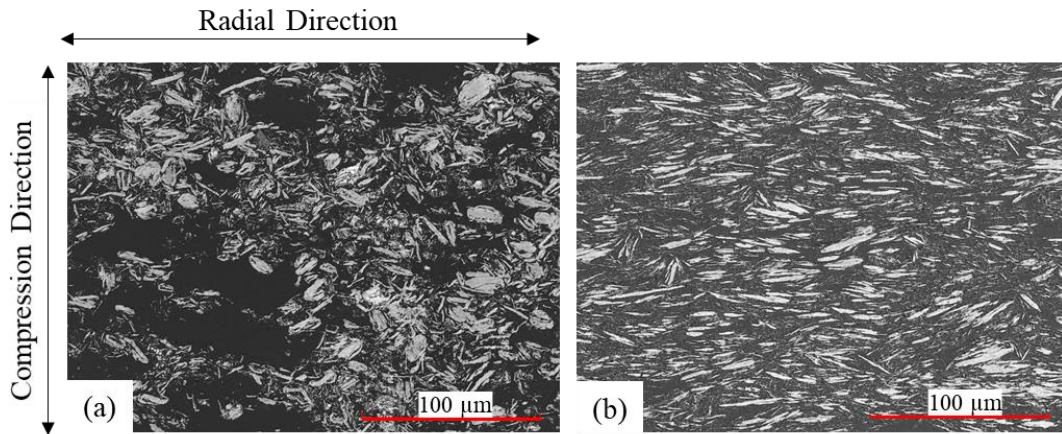


Figure 4.3 Laser/optical micrographs of the PFA-44 μm graphite composite compression molded samples: (a) 44 μm -20wt%-0h, (b) 44 μm -20wt%-25h.

The micrograph of the M9 μm -10wt%-25h sample (9 μm -20wt%-25h diluted with unprocessed PFA to 10 wt%) is compared to the undiluted sample (9 μm -10wt%-25h) in Figure 4.4. The graphite particles in the sample without ball milling (Fig. 4.4a) displayed an uneven particle distribution (with large clusters of plain PFA and no graphite particles), and random graphite particle orientation. After ball milling for 25 hours, the undiluted sample (Fig. 4.4b) showed evenly dispersed graphite particles oriented in the horizontal direction. The ball-milled sample diluted with unprocessed PFA (Fig. 4.4c) exhibited a general graphite orientation in the horizontal direction. However, the graphite particles

were not evenly dispersed as they formed a loose network around large clusters of plain PFA. Thus, introducing unprocessed PFA particles into the ball-milled composite reduced the uniformity of the particle distribution and the overall homogeneity of the composite.

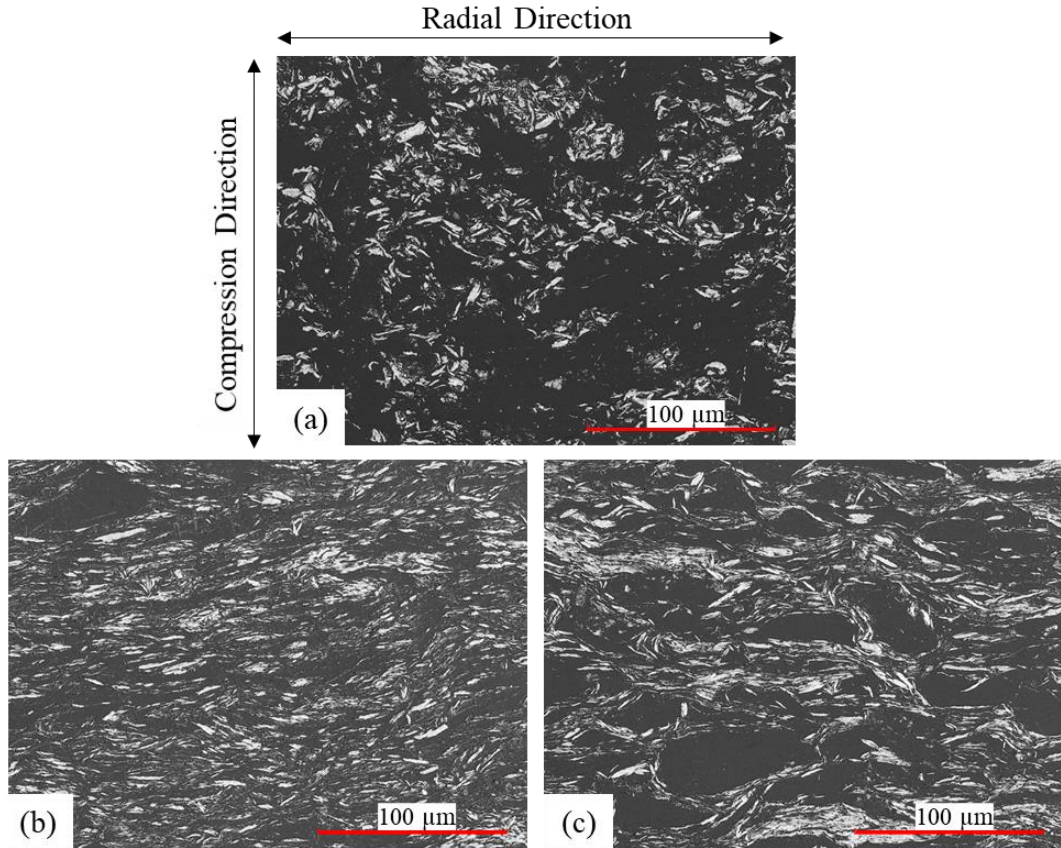


Figure 4.4 Laser/optical micrographs of the PFA- 9 μm graphite composite compression molded samples: (a) 9 μm -10wt%-0h, (b) 9 μm -10wt%-25h, and (c) M9 μm -10wt%-25h.

Figure 4.5 displays the cross-sectional micrographs of the PFA compression-molded disks containing MF-MLG filler particles. As shown in Figure 3.3b, it was expected that the magnetic field will align the MF-MLG particles vertically. Micrographs of the composite containing MF-MLG particles produced from Trial 2 (MF-MLG-2g-10wt%) are shown in Figures 4.5a and 4.5b. At low magnifications (Fig. 4.5a), large agglomerates of MF-MLG particles and random filler particle alignment are observed. At

high magnifications (Fig 4.5b), the large agglomerates appear very porous, and alignment of the graphene particles within the agglomerates is not clear. The composite containing MF-MLG particles produced from Trial 1 (MF-MLG-0.15g-1wt%) are shown in Figures 4.5c and 4.5d. At low magnifications (Fig. 4.5c) some of the filler particles appear to be aligned in the horizontal direction. As the alignment of the MF-MLG particles by the external magnetic field should occur in the vertical direction, this alignment is not due to the magnetic functionalization of the MLG particles. At high magnifications (Fig. 4.5d), it is observed that the agglomerates produced from Trial 1 (MF-MLG-0.15g) are very dense, and the alignment of the graphene particles within the agglomerates is not clear.

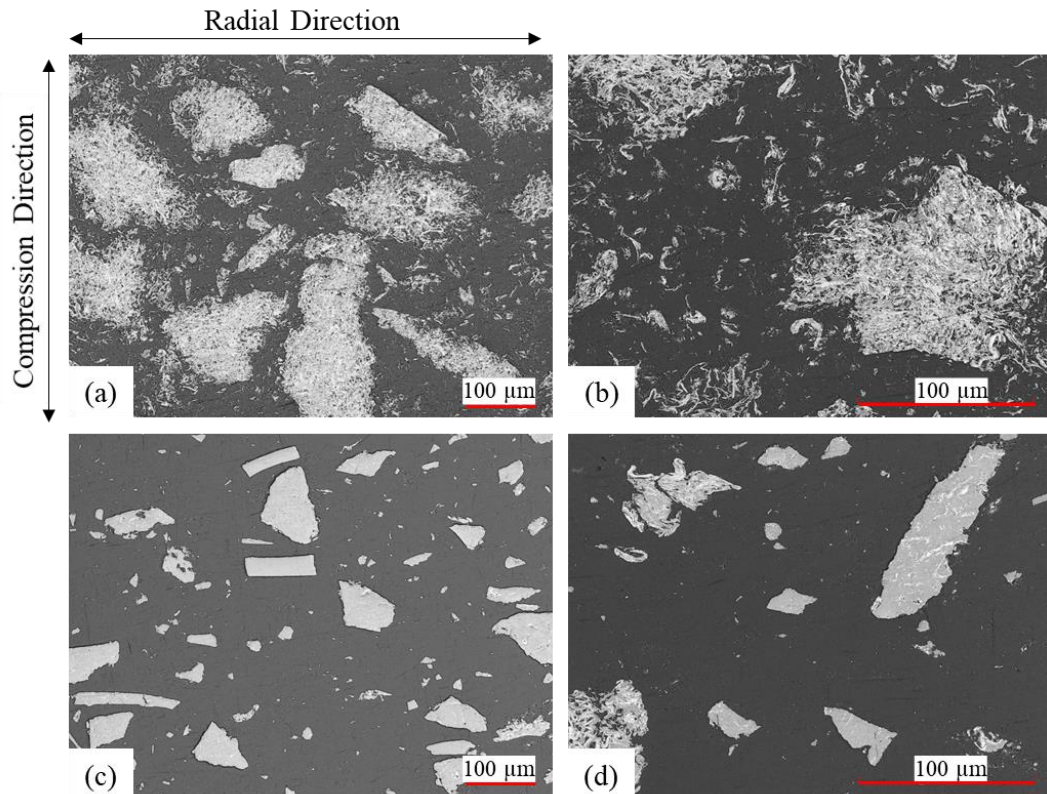


Figure 4.5 Laser/optical micrographs of the PFA- MF-MLG composite compression molded samples: (a) MF-MLG-2g-10wt% at $200\times$ magnification, (b) MF-MLG-2g-10wt% at $500\times$ magnification, (c) MF-MLG-0.15g-1wt% at $200\times$ magnification, and (d) MF-MLG-0.15g-1wt% at $500\times$ magnification.

4.1.2 Microstructural Analysis of Electrostatically Sprayed Composite Coatings

Figure 4.6 displays the cross section of an electrostatically coated coupon, sample 9 μm -10wt%-25h, labelling the different layers observed. The light gray area at the bottom of the micrograph is the stainless steel substrate, which is followed by a $\sim 50\ \mu\text{m}$ thick black primer layer, then a $\sim 150\text{-}250\ \mu\text{m}$ thick PFA-composite top layer. The mounting epoxy appears at the top of the micrograph. The light gray flake-like particles in the top layer are the graphite particles, and the light gray spheres within the primer layer are the mounting epoxy transferred from the mount to the sample during polishing. Cross-sectional micrographs of the electrostatically coated coupons of various composites are shown in Figure 4.7–4.9.

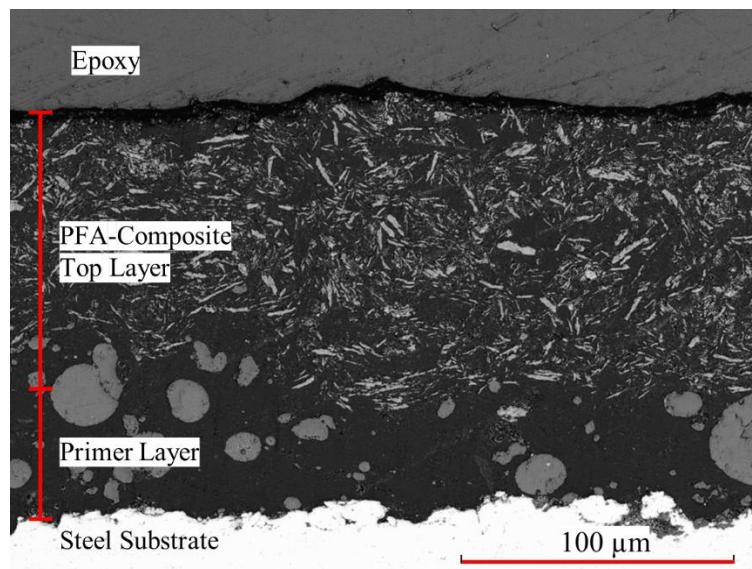


Figure 4.6 Example of the cross section of an electrostatically coated coupon (9 μm -10wt%-25h) displaying the steel substrate followed by a $\sim 50\text{-}\mu\text{m}$ primer layer and a subsequent $\sim 150\text{-}250\ \mu\text{m}$ PFA-composite top layer.

Micrographs for the samples containing 20 wt% filler are shown in Figure 4.7. The graphene particles in the 60nm-20wt%-25h (Fig. 4.7a) sample are mostly oriented along the horizontal direction. The 9 μm -20wt%-25h (Fig. 4.7b) and 44 μm -20wt%-25h (Fig.

4.7c) samples also appear to have a general alignment of particles along the horizontal direction, but the particles are not as ordered as the 60nm-20wt%-25h sample. All samples containing 20 wt% filler display good particle distribution of within the polymer matrix. The surface finish of the samples may be visually analyzed at the interface between the PFA composite top layer and the epoxy. All the samples with 20 wt% filler appear to have a rough surface, as displayed by the large peaks and valleys at the composite-epoxy interface. This is worsened by the loosely bonded filler particles directly protruding from the coatings.

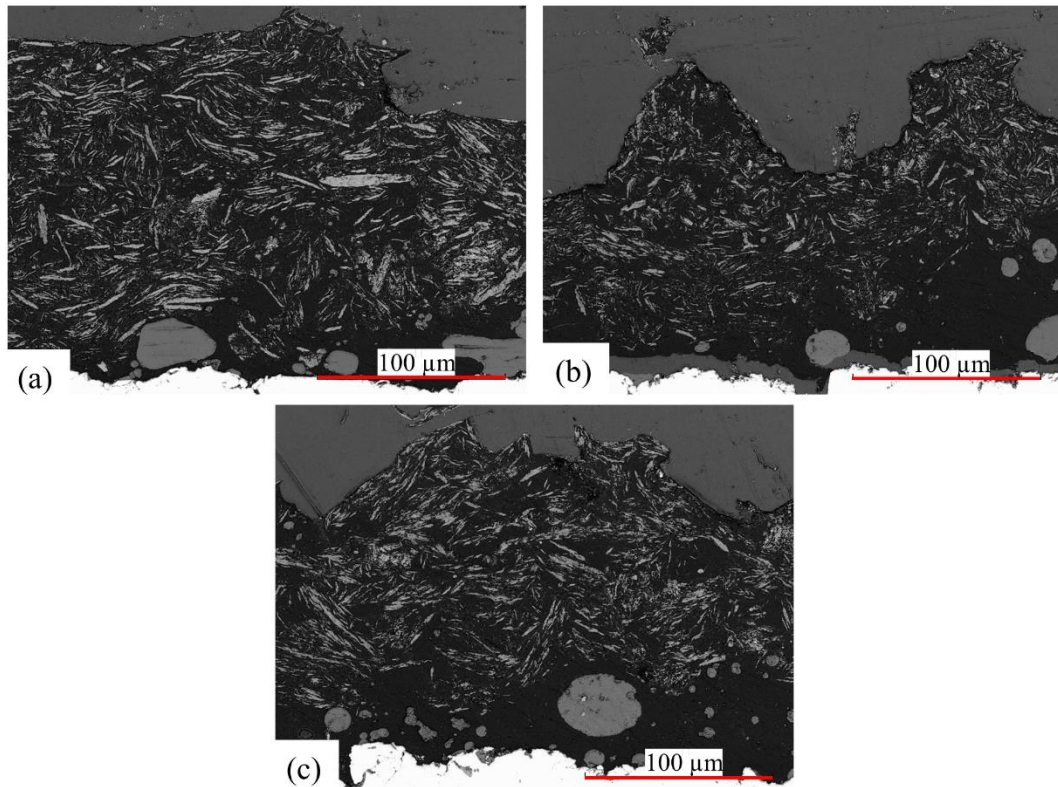


Figure 4.7 Laser/optical cross-sectional micrographs of the electrostatically coated PFA-composite coupons: (a) 60nm-20wt%-25h, (b) 9µm-20wt%-25h, and (c) 44µm-20wt%-25h.

Cross-sectional micrographs of the 9µm-10wt%-25h and M9µm-10wt%-25h electrostatically coated composite samples are shown in Figures 4.8a and 4.8b,

respectively. It is observed that the graphite particles in both samples are generally aligned in the horizontal direction. However, the particle alignment appears less ordered than in the compression-molded samples. The particle distribution in the sample diluted with unprocessed PFA (M9 μ m-10wt%-25h) contains small pockets of plain PFA. The undiluted sample (9 μ m-10wt%-25h) displays better homogeneity between the graphite filler and the matrix PFA. The surface of the diluted sample (M9 μ m-10wt%-25h) appears to be slightly rougher than the undiluted sample (9 μ m-10wt%-25h), but both coatings show much smoother surfaces than the coatings with 20 wt% filler.

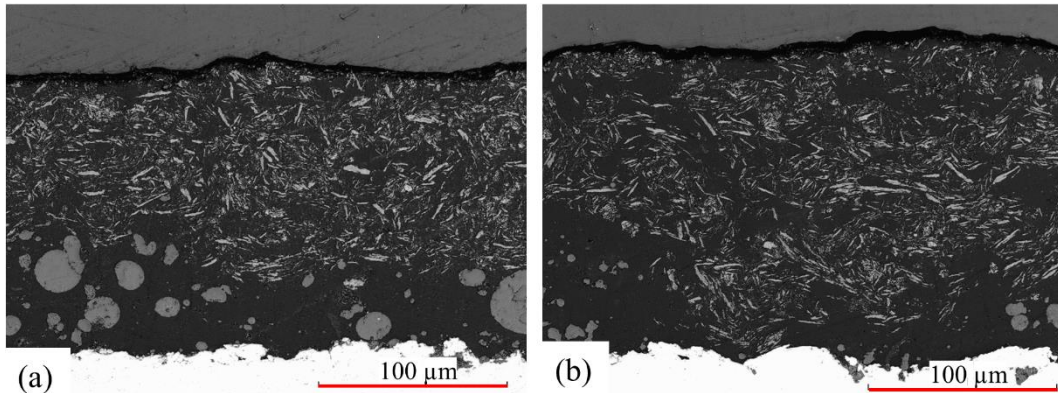


Figure 4.8 Cross-sectional laser/optical micrographs of the electrostatically coated PFA-composite samples: (a) 9 μ m-10wt%-25h, and (b) M9 μ m-10wt%-25h.

Micrographs of the coating containing the MF-MLG-2g filler are shown in Figure 4.9. Similar to the compression-molded disk, the MF-MLG particles in the cross section of the coated coupon also appear in large agglomerates with no obvious alignment of the filler particles to a specific direction. The surface of the MF-MLG filled composite coating appears to be quite smooth (Fig. 4.9a), but rough patches are observed when the MF-MLG agglomerates occur at the coating surface (Fig. 4.9b).

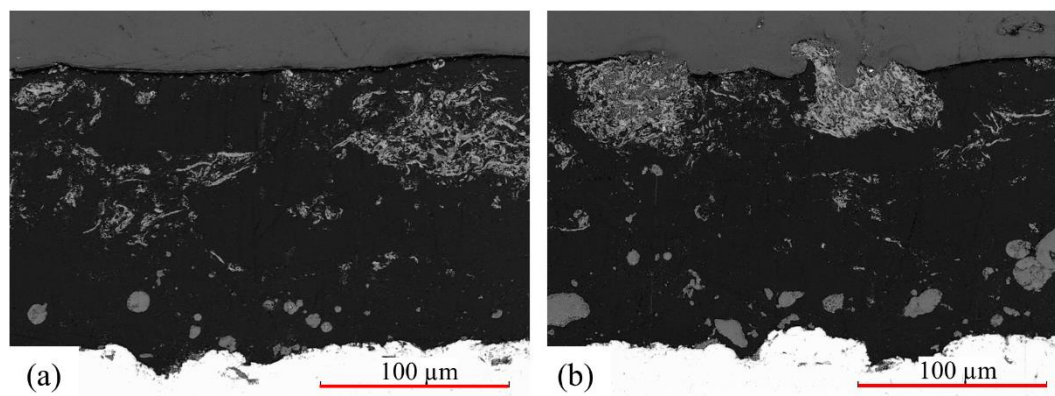


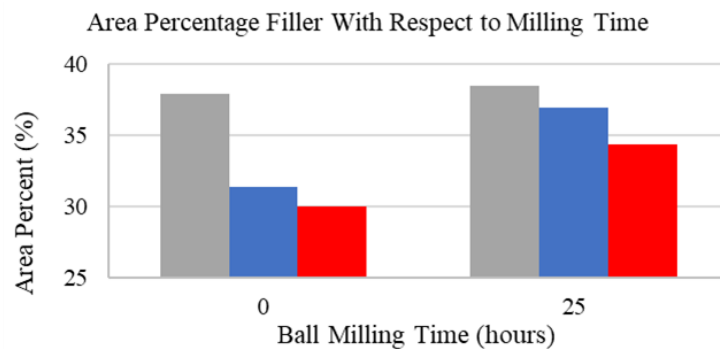
Figure 4.9 Cross-sectional laser/optical micrographs of the electrostatically coated MF-MFG-2g-10wt% composite sample at two different locations: (a) the filler particle distribution and alignment, and (b) MF-MFG particle at the surface of the coating, leading to higher surface roughness values.

4.1.3 Microscopy Image Analysis

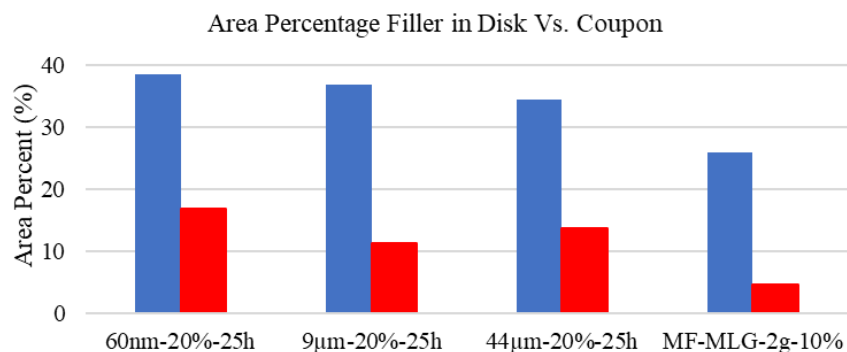
The cross-sectional micrographs of the compression-molded disks and electrostatically coated coupons were analyzed (as described in Section 3.4.1.2) to “quantitatively” evaluate the distribution of the filler in the matrix. The area percentages of fillers for the compression-molded disk samples with 20 wt% filler (60 nm, 9 μm, 44 μm) after ball milling for 0 and 25 hours are shown in Figure 4.10a. It is observed that the area percent of filler in samples without ball milling (0 hours) decreases as the graphite particle size increases. The sample with 60 nm MLG particles has the highest area percent of filler, followed by the 9-μm graphite particles, and then the 44-μm graphite particles. After ball milling for 25 hours, the area percent of filler increases in all samples. The area percent of the 60 nm MLG particles only increased slightly, but the area percent of the 9-μm and 44-μm graphite particles increased substantially. As smaller particle sizes yield larger filler area percentages, the substantial increase in the area percentages of the 9-μm and 44-μm graphite indicates that the particles were exfoliated into smaller particles during

ball milling. It appears that ball milling had little impact on the 60 nm MLG particles since these are already very small.

Table 4.1 summarizes the area percentages of fillers for both the compression-molded disks and electrostatically-coated samples. The 60nm-20wt%-25h coating has the largest area percent. However, the 44 μ m-20wt%-25h coating has a slightly higher area percent of filler than the 9 μ m-20wt%-25h coating despite having a smaller initial filler particle size. The area percent of filler of the compression molded disks is compared to the electrostatically sprayed coupons in Figure 4.10b. It is observed that the area percent of filler is consistently lower in the electrostatically coated samples compared to the compression molded disk samples. It should be noted that the area percent of filler particles in the electrostatically coated samples is more difficult to evaluate using the ImageJ software relative to the compression molded samples. The area percent of coated samples must be carefully evaluated to avoid the primer layer and epoxy at the edge of the surface.



(a) ■ 60 nm MLG ■ 9 μm Graphite ■ 44 μm Graphite



(b) ■ Compression-Molded Disk ■ Electrostatically-Coated Coupon

Figure 4.10 The area percentage of filler: (a) for compression-molded disk samples (60nm-20wt%, 9μm-20wt%, 44μm-20wt%) after 0 and 25 hours of ball milling, and (b) for the compression molded disks versus electrostatically coated coupons.

Table 4.1 The area percentages of fillers calculated using the ImageJ software for various fillers, weight percentages, and ball milling times.

Filler Type	Weight Percent (%)	Milling Time (Hours)	Area Percent (%) (Disk Sample)	Area Percent (%) (Coated Sample)
60 nm Multi-Layer Graphene	20	0	37.92	12.51
		25	38.50	16.79
9 μm Graphite	10	0	16.52	-
25		24.83	10.07	
9 μm Graphite (mixture)*		25	27.29	12.19
9 μm Graphite	20	0	31.38	-
		5	36.91	-
		10	33.90	-
		15	37.78	-
		20	39.32	-
		25	36.98	11.32
		30	29.04	-
44 μm Graphite	20	0	30.04	-
		25	34.41	13.67
MF-MLG-0.15 g Sample	1	0	10.25	-
MF-MLG-2.0 g Sample		0	25.90	4.64

4.1.4 Morphology and Compositional Analysis of Blended Powders

SEM characterization was conducted on the blended powder mixtures to examine the impact of the processing method on the filler and matrix particles. Figure 4.11 shows SEM images of the blended powder mixtures (not cured) containing PFA and 20 wt% 44 μm graphite with increasing milling time. After ball milling for 20 hours, the graphite particles are indistinguishable from the PFA particles, and the morphology of the particles become very flat and flake-like. No apparent changes in particle distribution and morphology are noticed with further increase of the milling time from 25 h to 30 h. Figure 4.12 displays the SEM images for the PFA-44 μm graphite blended powder mixture (not cured) with increasing filler weight percentage. Again, no obvious variations in particle morphology are observed when the filler amount increases from 10 wt% to 20 wt%. Energy dispersive spectroscopy (EDS) mapping was performed on the 44 μm -20wt%-30h sample, and the element overlay is shown in Figure 4.13. PFA consists of fluorine (F) and carbon (C), whereas graphite consists of only carbon. Thus, the large clusters of purple (carbon) regions in the EDS map indicate graphite particles. The purple patches still contain small specks of fluorine (yellow). Furthermore, the purple clusters identified in the EDS overlay are indistinguishable when viewed in the corresponding SEM images. Thus, the graphite particles appear thoroughly dispersed, and lightly coated with PFA, within the PFA matrix.

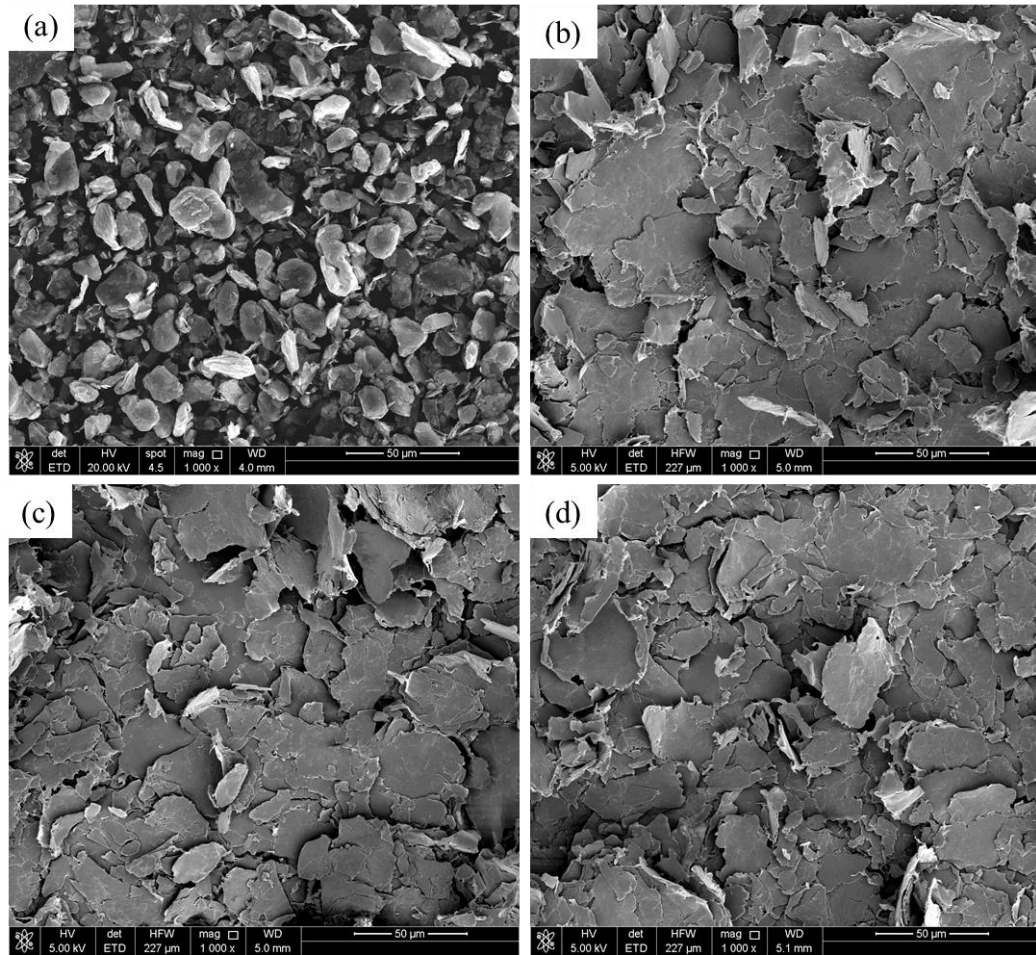


Figure 4.11 SEM images of the PFA-20 wt% 44 μm graphite powder mixture (before curing): (a) before ball milling, (b) after ball milling for 20h, (c) after ball milling for 25h, and (d) after ball milling for 30h.

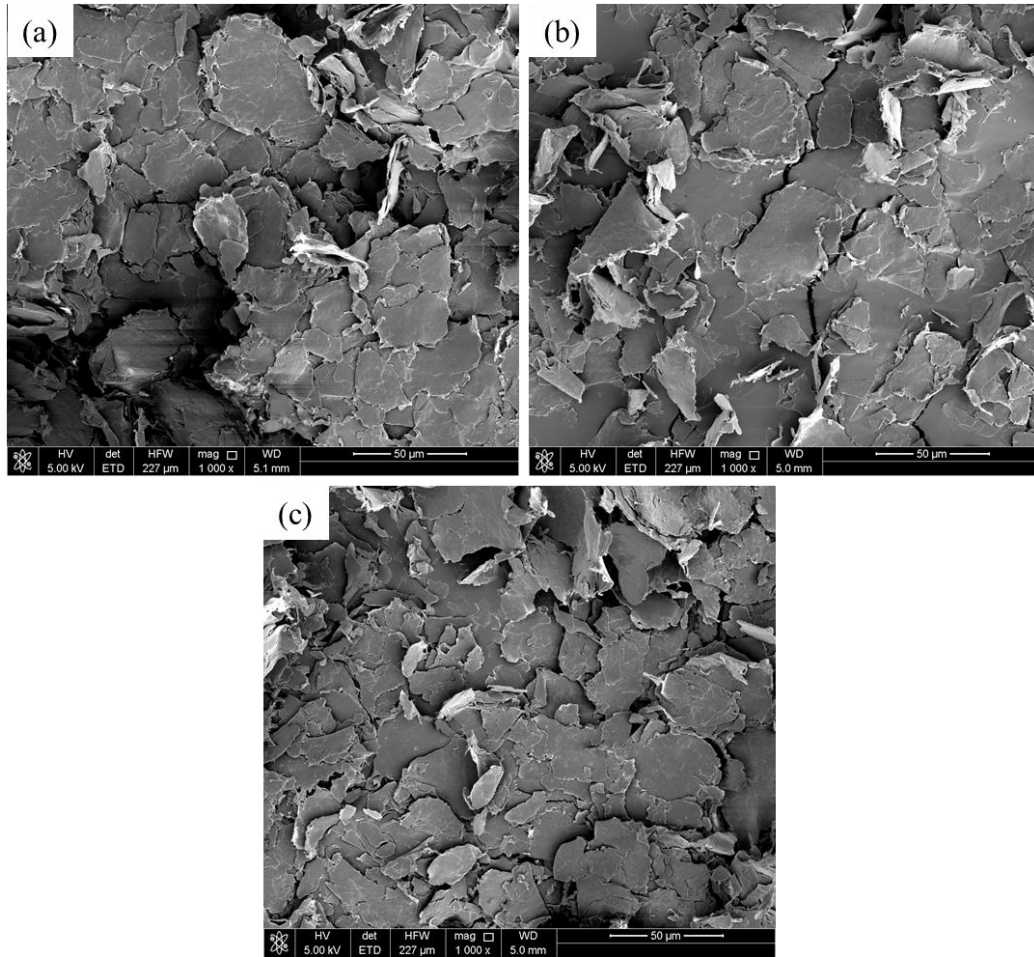


Figure 4.12 SEM images of the blended powder mixture (before curing) after ball milling for 25 hours containing various amounts of 44 μm graphite filler: (a) 10 wt% , (b) 15 wt%, and (c) 20 wt%.

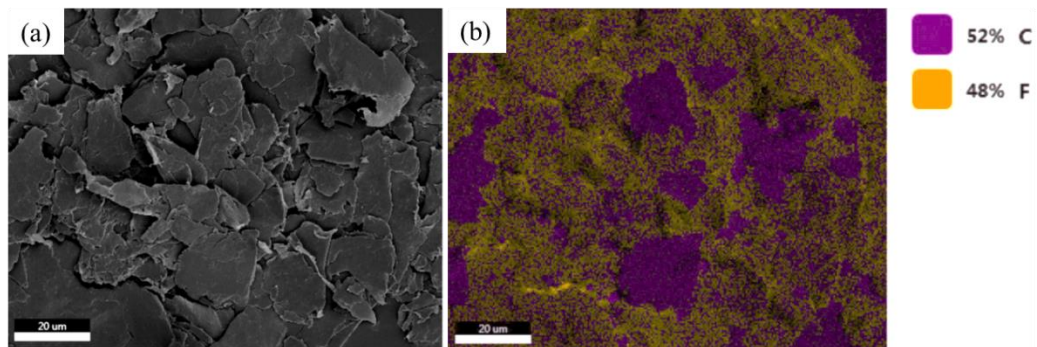


Figure 4.13 Energy dispersive spectroscopy analysis of the powder mixture containing 20 wt% 44 μm graphite after ball milling for 30 hours (before curing): (a) SEM image, and (b) EDS element overlay map.

Figure 4.14 shows the SEM images of the blended powder mixture containing 10 wt% MF-MLG (without ball milling). The PFA matrix appears as small relatively smooth spherical particles, whereas the MF-MLG filler particles appear significantly larger, irregularly shaped, and rough. The EDS spectra taken at Spot 1 and Spot 2 are displayed in Figure 4.14(c) and 4.14(d), respectively. The EDS spectrum at Spot 1 confirms that the irregularly shaped particle is the MF-MLG filler (C, O, and Fe elements, characteristic of the magnetic nanoparticles), and the spherical particle is the PFA matrix (C and F elements). Figure 4.14(b) shows a higher magnification view of the MF-MLG particle, exemplifying the rough surface and apparent excess of magnetic nanoparticle surrounding the MLG.

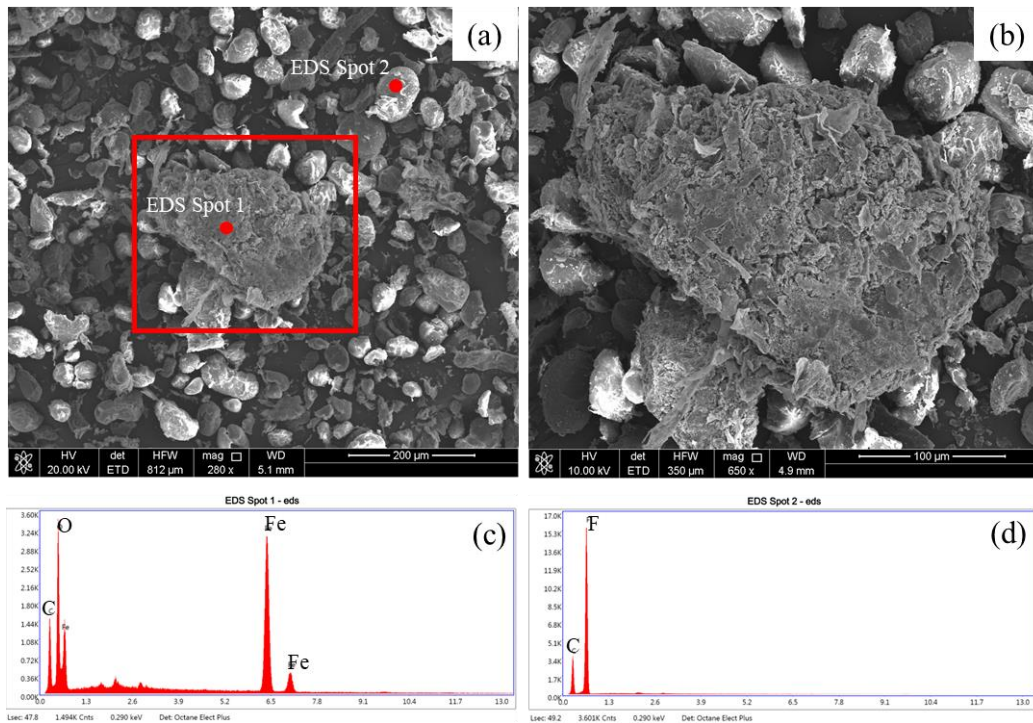


Figure 4.14 SEM images and EDS spectra of the blended powder mixture (before curing, without ball milling) containing PFA and 10 wt% MF-MLG (MF-MLG-2g-10wt%): (a) SEM image at a lower magnification showing the PFA and MF-MLG particles, (b) a higher magnification SEM image of the area outlined in (a), showing the rough surface of the MF-MLG particle, (c) the EDS spectrum for ‘EDS Spot 1’ shown in (a), (d) the EDS spectrum for ‘EDS Spot 2’ shown in (a).

4.2 Surface Topography Analysis

The arithmetic mean height surface roughness (R_a) and root mean square surface roughness (R_q) values for the electrostatically coated composite coupons are summarized in Table 4.2. The surface roughness is higher in samples with smaller initial graphite particle sizes (before ball milling). The coating containing 60 nm MLG filler particles has the largest surface roughness, followed by the coating with 9- μm graphite filler particles, and then the coating with 44- μm filler particles. Furthermore, the surface roughness increases with increasing filler content. For instance, the surface roughness of the coating containing 9- μm graphite filler increased roughly 7 times when the filler content was increased from 10 wt% (9 μm -10wt%-25h, $R_a = 8.08 \pm 0.03$) to 20 wt% (9 μm -20wt%-25h, $R_a = 56.37 \pm 1.49$).

Table 4.2 The arithmetic mean height surface roughness (R_a) and root mean square roughness (R_q) values obtained from optical /laser microscopy (scan area: $1000 \times 1400 \mu\text{m}^2$).

Sample Type	R_a (μm)	R_q (μm)
60nm-20wt%-25h	68.50 ± 3.27	85.21 ± 3.97
9 μm -20wt%-25h	56.37 ± 1.49	71.04 ± 2.44
44 μm -20wt%-25h	50.92 ± 1.28	61.63 ± 1.79
MF-MLG-2g-10wt%	10.03 ± 4.06	14.06 ± 4.98
9 μm -10wt%-25h	8.08 ± 0.03	10.11 ± 0.26
M9 μm -10wt%-25h	13.07 ± 0.60	16.19 ± 0.23

Three-dimensional laser-optical profiles of the coatings are shown in Figure 4.15. The optical laser micrographs for the 20 wt% filler samples (Figs. 4.11 a, b, c) display a very rough surface, with uneven pits and peaks throughout the samples. Conversely, the 9 μm -10wt% samples (Figs. 4.11 1d, e, f) appear very smooth, with subtle variations in height throughout the samples. The sample containing the MF-MLG filler particles (Fig. 4.11 d) appears smooth, with random peaks leading to a rise in the surface roughness. The

peaks are likely attributed to large MF-MLG particles at the surface, as shown in Figure 4.9c.

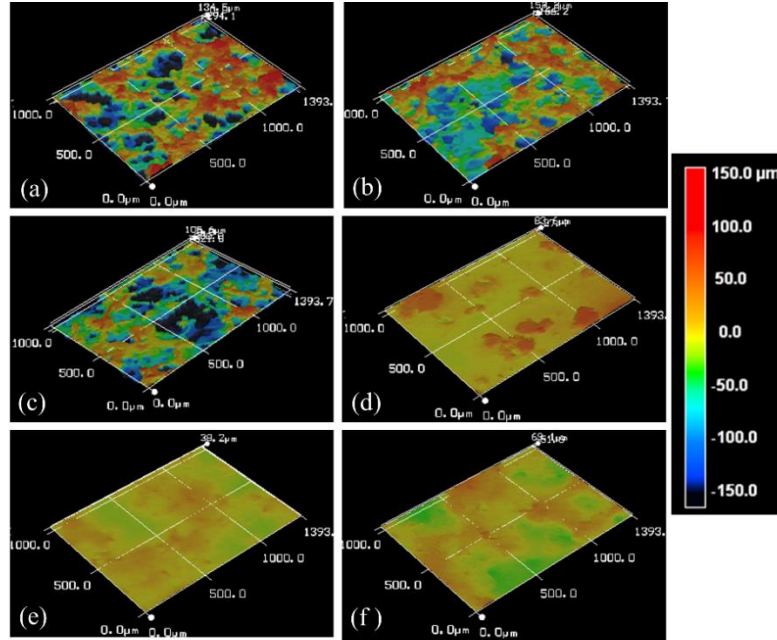


Figure 4.15 Three-dimensional optical/laser profiles of the composite coatings: (a) 60nm-20wt%-25h, (b) 44µm-20wt%-25h, (c) 9µm-20wt%-25h, (d) MF-MFG-2g-10wt%, (e) 9µm-10wt%-25h, (f) M9µm-10wt%-25h.

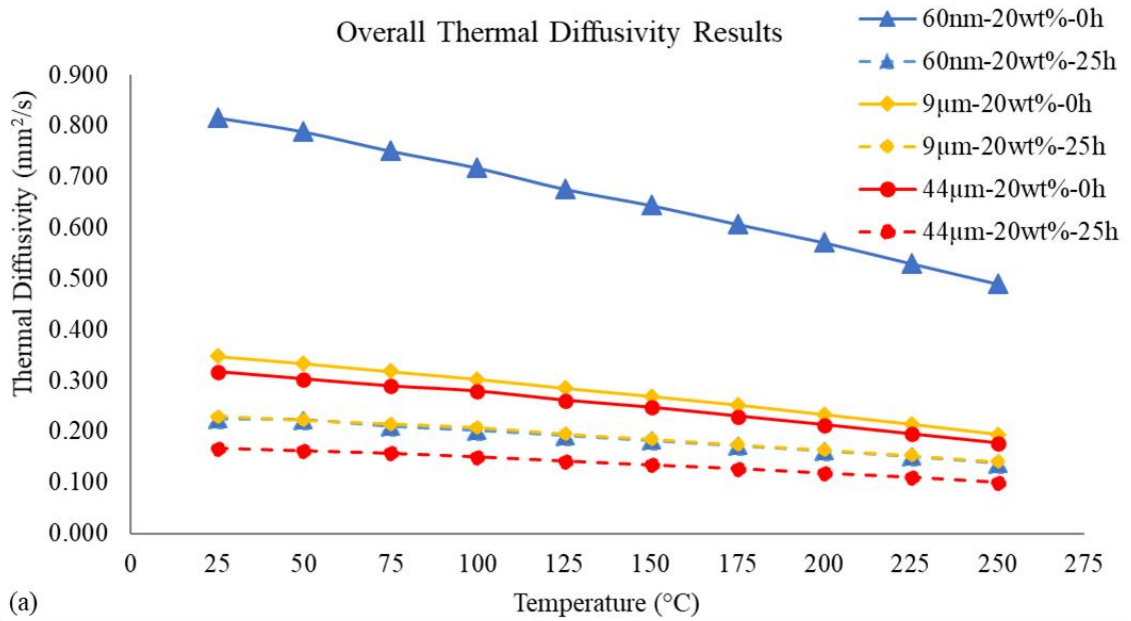
4.3 Thermal Analysis

The thermal conductivities of the compression-molded disks are calculated as a function of the material's thermal diffusivity, specific heat, and density, as described in Section 3.4.3 (Eq. 3.2). The thermal conductivities from 25 °C to 250 °C for all the samples are shown in Figures 4.16 - 4.21.

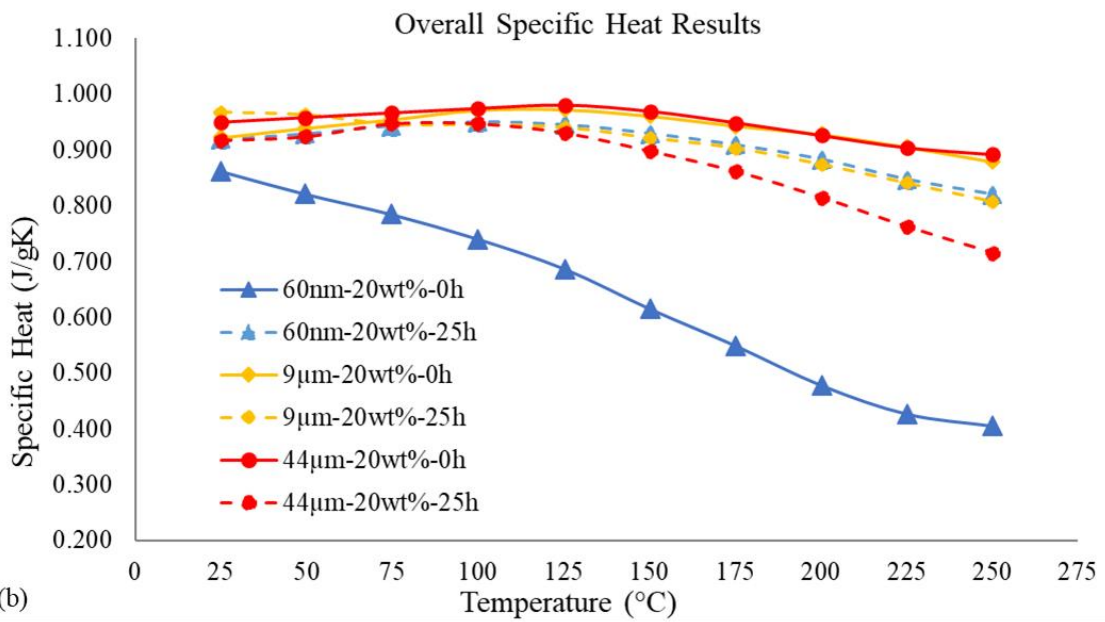
Figure 4.16 and Figure 4.17 summarize the overall thermal property results for samples containing 20 wt% filler that were ball milled for 0 and 25 hours (60nm MLG, 9 µm graphite, and 44 µm graphite). Generally, the thermal diffusivity values gradually decrease as the temperature increases (Fig. 4.16a). For composites without ball milling, the thermal diffusivity shows significant differences among the composites filled with

different particles. The thermal diffusivity decreases with the increase of filler particle size: the 60nm-20wt%-0h sample has the highest thermal diffusivity values, which are about 2× of the 9μm-20wt%-0h and 44μm-20wt%-0h samples. After ball milling for 25 hours, the thermal diffusivity of the 60nm-20wt% MLG composite dropped significantly, while the 9μm-20wt%-25h and 44μm-20wt%-25h samples moderately dropped. The specific heat values are shown in Figure 4.16b. The 60 nm MLG filled composite (without ball milling) exhibits a substantial and gradual decrease in specific heat with the increase of temperature, while all the other samples show essentially the same specific heat until the temperature reached 125 °C, starting from which the specific heat also decreases with the temperature.

The overall thermal conductivity (Fig. 4.17) values similarly decrease as the temperature increases. The 60nm-20wt%-0h sample displayed the highest thermal conductivity value, followed by the 9μm-20wt%-0h sample, and then the 44μm-20wt%-0h sample. Thus, smaller graphite particles exhibit higher thermal conductivity values. However, all the samples exhibit a significant decrease in thermal conductivity after undergoing ball milling for 25 hours. Like the samples that did not undergo ball milling, the milled samples with smaller initial graphite particles exhibited higher thermal conductivity values.



(a)



(b)

Figure 4.16 The overall thermal property results from 25 °C to 250 °C for the composite samples containing 60 nm MLG, 9 µm graphite, and 44 µm graphite filler particles (no ball milling, and milled for 25 hours). The graphs summarize the: (a) thermal diffusivity values, and (b) specific heat values.

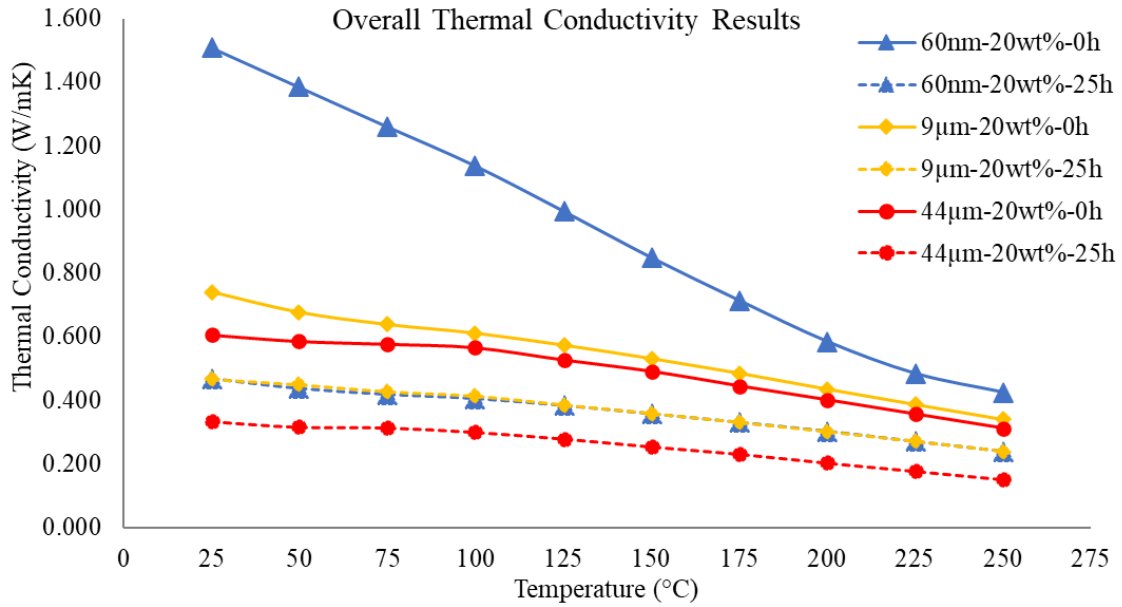


Figure 4.17 The overall thermal conductivity results from 25 °C to 250 °C for the composite samples containing 60 nm MLG, 9 µm graphite, and 44 µm graphite filler particles (no ball milling and milled for 25 hours).

The thermal conductivity values for samples containing different fractions (10wt%, 15wt%, and 20wt%) of the 60 nm MLG filler are shown for and milling times (0h, 25h) in Figure 4.18(a). The thermal conductivity values increase with higher filler weight fractions. All samples experience a decrease in thermal conductivity after ball milling for 25 hours. The effect of increasing ball milling time on the samples thermal conductivity is shown in Figure 4.18(b). As previously observed, the thermal conductivity is significantly higher in samples that underwent no ball milling. The thermal conductivity values appear the same for samples undergoing 20 hours, 25 hours, and 30 hours of ball milling.

The thermal conductivity values for composite samples containing 9 µm filler with different filler weight fractions (1 0wt%, 15 wt%, 20 wt%) and ball milling times (0h, 25h) are summarized in Figure 4.19. Samples containing higher weight fraction of filler

displayed higher thermal conductivity values. All samples displayed a decrease in thermal conductivity after ball milling. Interestingly, the M9 μm -10wt%-25h sample that was diluted with unprocessed PFA powder displays better thermal property results than the undiluted sample (9 μm -10wt%-25h). The diluted sample (M9 μm -10wt%-25h) displays very comparable thermal conductivity values to the sample that did not undergo ball milling (9 μm -10wt%-0h). Figure 4.19(b) shows the thermal conductivity values with increasing ball milling times (0h, 5h, 10h, 15h, 20h, 25h, 30h). The samples that underwent ball milling displayed similar thermal conductivity values, with no clear influence of ball milling time on the resulted thermal performance.

The thermal conductivity values for the composites containing 44 μm graphite filler are shown in Figure 4.20(a) with different filler weight fractions (10wt%, 15wt%, 20wt%) and ball milling times (0h, 25h). Consistent with previous results, the thermal conductivity increases with increases in filler weight fraction and decreases after the sample undergoes ball milling. The effect of ball milling time on the thermal conductivity is shown in Figure 4.20(b). The sample that underwent no ball milling displays a significantly higher thermal conductivity. The samples that were ball milled for 20-30 hours display very similar thermal conductivity values, with no clear trend between thermal conductivity and milling time.

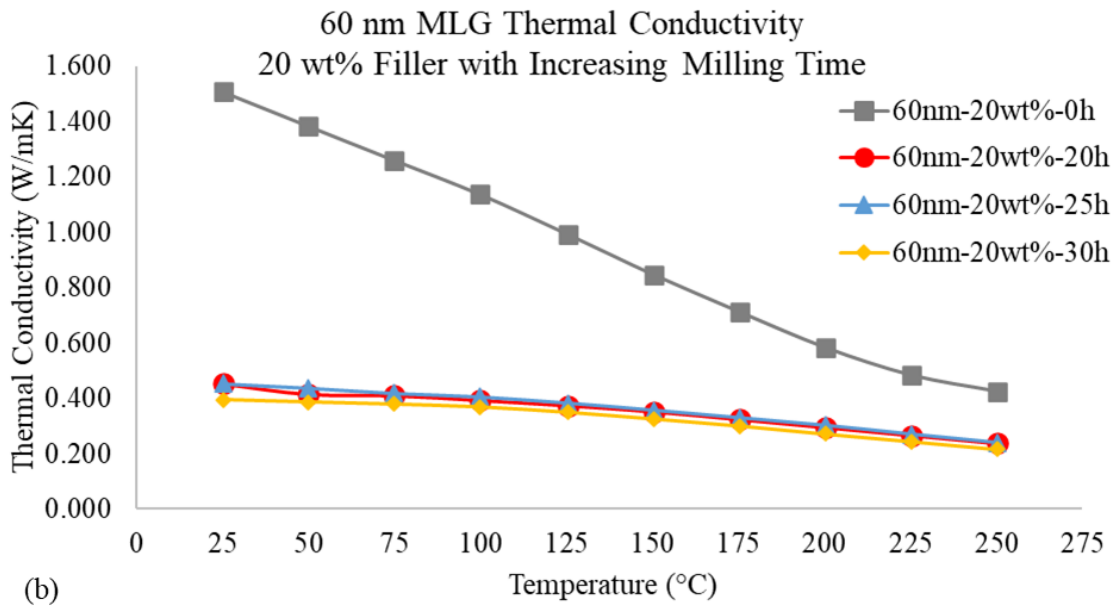
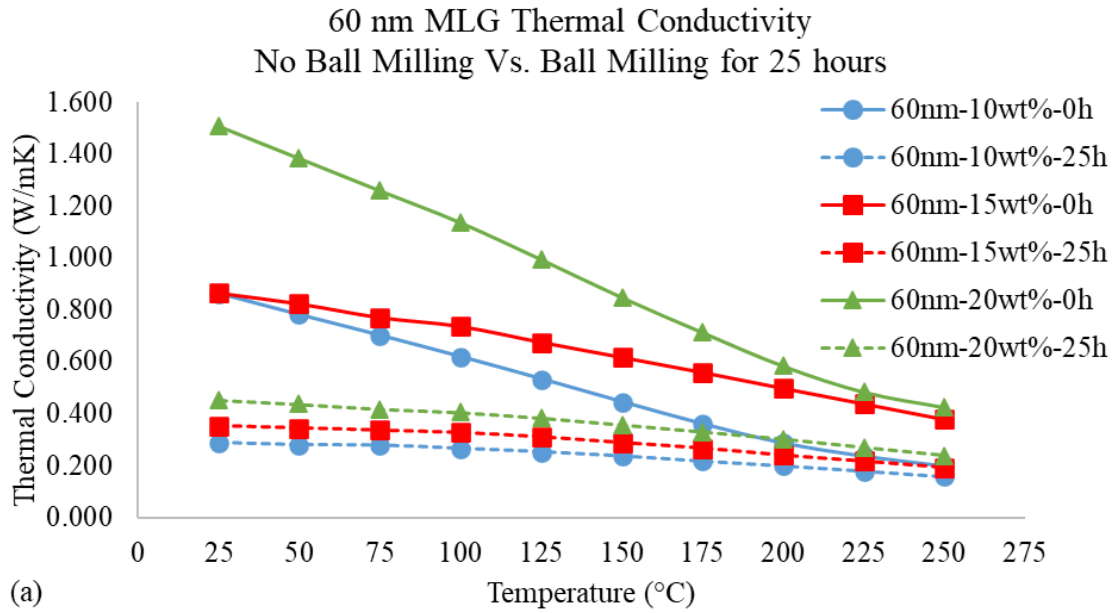


Figure 4.18 The thermal conductivity values from 25 °C to 250 °C for the 60 nm MLG filled composites with: (a) increasing filler weight percent (10wt%-20wt%) for samples that underwent no ball milling, versus ball milling for 25 hours, and (b) increasing ball milling time (0-30 hours) for samples with 20 wt% filler.

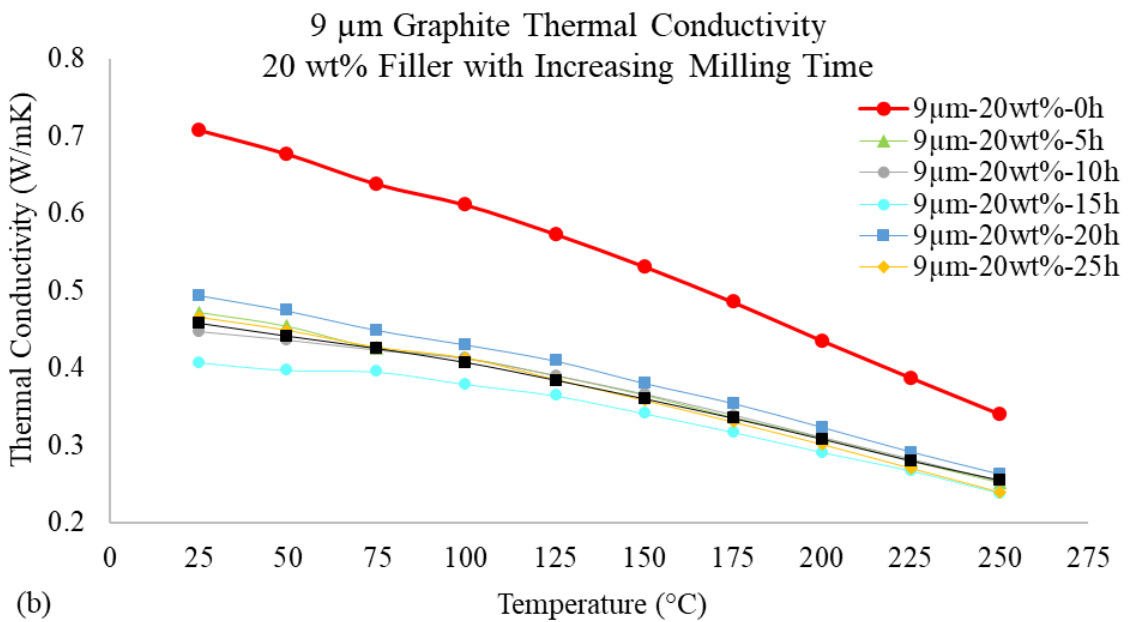
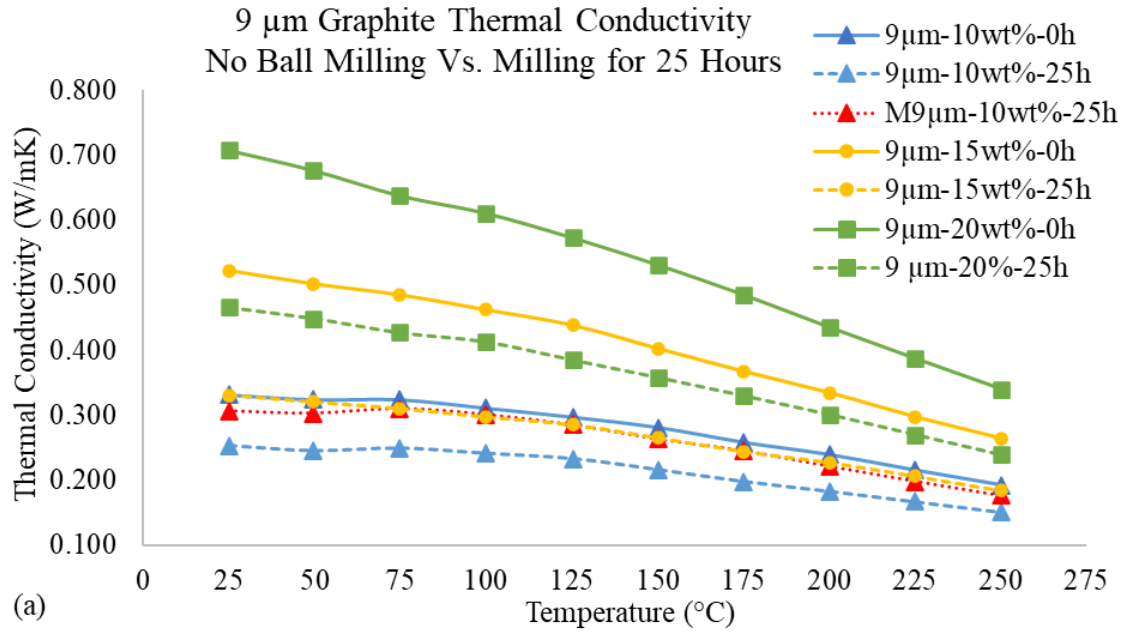


Figure 4.19 The thermal conductivity values from 25 °C to 250 °C for the 9 μm graphite filled composites with: (a) increasing filler weight percent (10wt%-20wt%) for samples that underwent no ball milling, versus ball milling for 25 hours, and (b) increasing ball milling time (0-30 hours) for samples with 20 wt% filler.

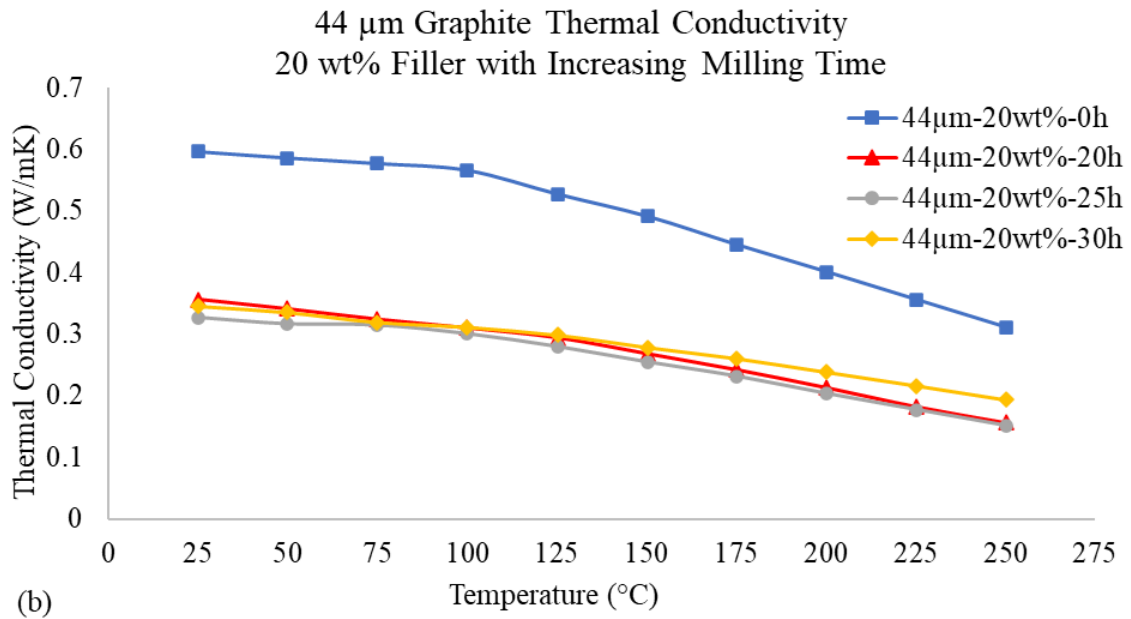
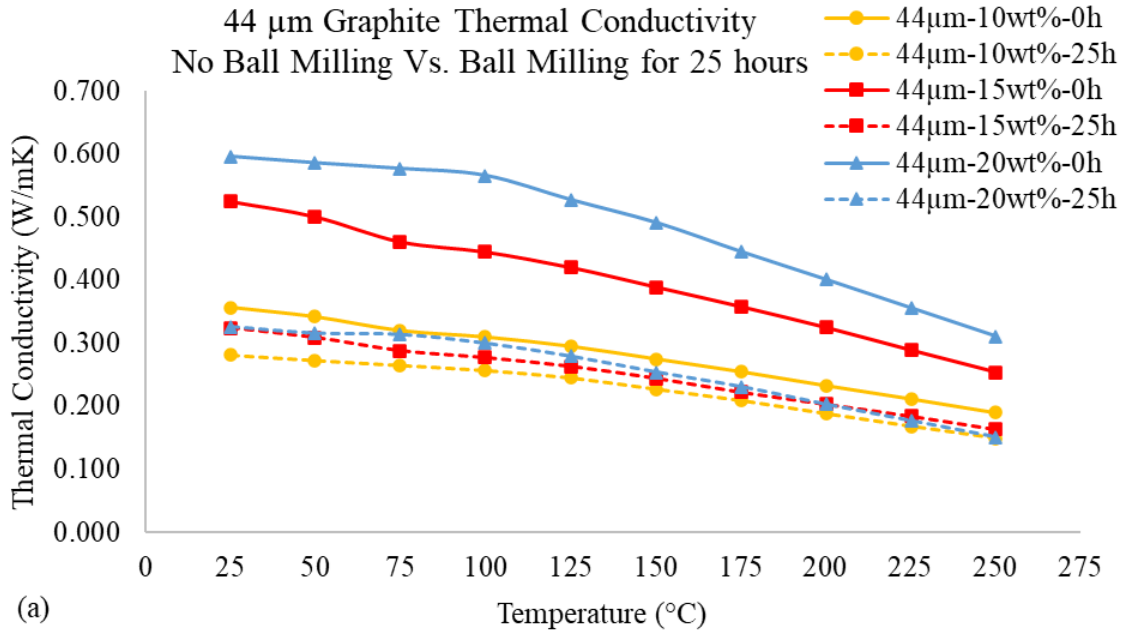


Figure 4.20 The thermal conductivity values from 25 °C to 250 °C for the 44 μm graphite filled composites with: (a) increasing filler weight percent (10wt%-20wt%) for samples that underwent no ball milling, versus ball milling for 25 hours, and (b) increasing ball milling time (0-30 hours) for samples with 20 wt% filler.

The thermal conductivity of the MF-MLG filled samples is compared to samples containing randomly oriented graphene particles, shown in Figure 4.21. For both weight fractions of MLG (1wt% and 10wt%), the composite samples containing randomly oriented MLG have a higher thermal conductivity from 25 °C to ~120 °C. At ~120 °C the thermal conductivity values for the composites containing randomly oriented MLG and the composites containing MF-MLG breakeven, after which the MF-MLG values display higher thermal conductivity values with further increases in temperature. The thermal conductivity for all samples decreases with increases in temperature however, the samples containing randomly oriented MLG decrease at a greater rate resulting in the breakeven point. The thermal conductivity of the samples containing 10 wt% filler is higher than the samples containing 1 wt% filler.

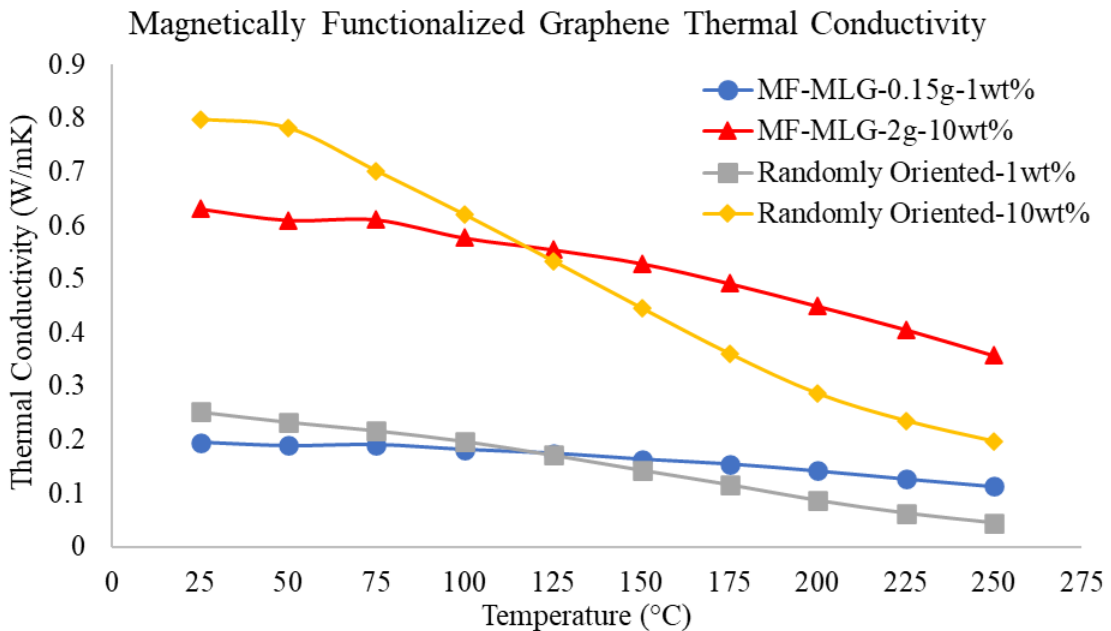


Figure 4.21 The thermal conductivity values from 25 °C to 250 °C for the PFA composites containing MF-MLG-0.15g, MF-MLG-2g, and randomly oriented graphene filler particles.

4.4 Wear Test Results

4.4.1 Coefficient of Friction and Wear Rates

Pin-on-disk wear testing was conducted on composite coated samples as described in section 3.4.4. The variation of the coefficient of friction (COF) versus sliding distance for composite coatings containing various filler particles (60nm-20wt%-25h, 9 μ m-20wt%-25h, 44 μ m-20wt%-25h, MF-MLG-10wt%) are shown in Figure 4.22. All samples display a running-in period for the first ~250 m where the COF rapidly increases with the sliding distance. After the initial running-in period, the samples that underwent ball milling experience a slight decrease in COF and begin to enter a steady state. However, all samples experienced slight fluctuations in COF values throughout the testing, even during their 'steady state' period. The 44 μ m-20wt%-25h sample had the lowest COF value throughout the testing, followed by the 60nm-20wt%-25h, 9 μ m-20wt%-25h, and finally the MF-MLG-10wt% samples. The COF for the 44 μ m-20wt%-25h sample experienced an abrupt increase and extremely unsteady COF values at ~2000 m. The 9 μ m-20wt%-25h sample displayed a substantial drop and sudden rise in the COF, followed by extreme fluctuations in COF values after ~1750 m. Conversely, the 60nm-20wt%-25h sample did not experience any sudden peaks in COF throughout the testing. The MF-MLG-2g-10wt% sample experiences several sudden drops and rises in the COF value throughout the testing. Wear debris was observed after roughly 5 minutes of testing for all samples, further accumulating throughout the testing.

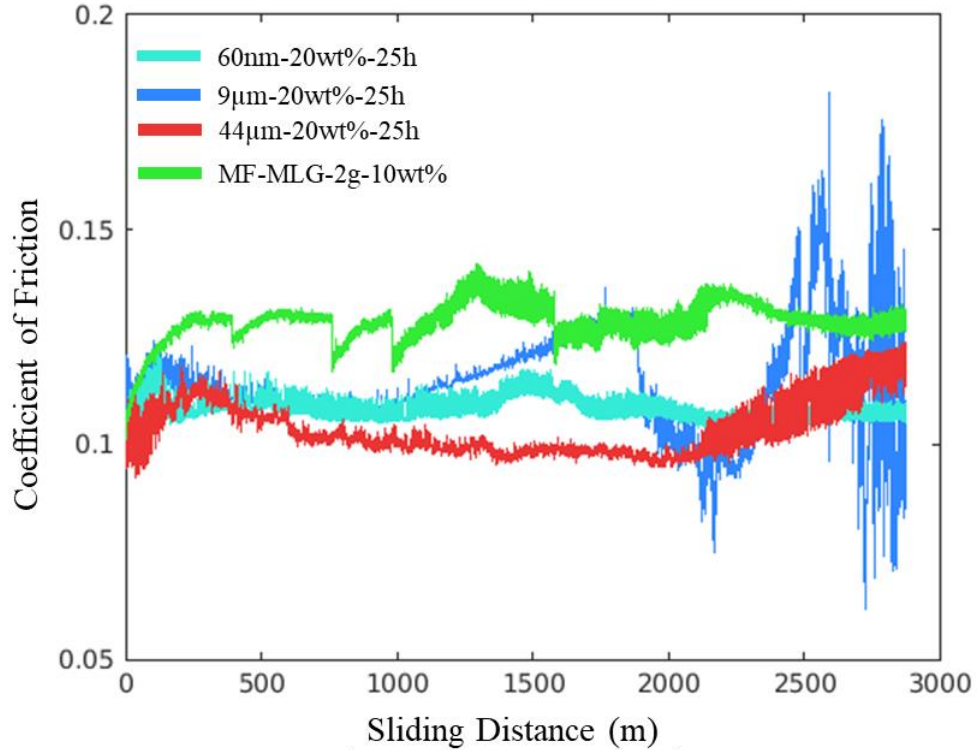


Figure 4.22 The coefficient of friction (COF) versus sliding distance curves for composite-coated samples: 60nm-20wt%-25h, 9µm-20wt%-25h, 44µm-20wt%-25h, and MF-MLG-10wt%.

Figure 4.23 displays the variation of COF with respect to sliding distance for composite samples containing 9-µm graphite filler (9µm-20wt%-25h, 9µm-10wt%-25h, M9µm-10wt%-25h). The composite samples containing 10 wt% 9-µm graphite filler remain in steady state throughout the testing. However, the fluctuation in the COF values gradually increases with the sliding distance.

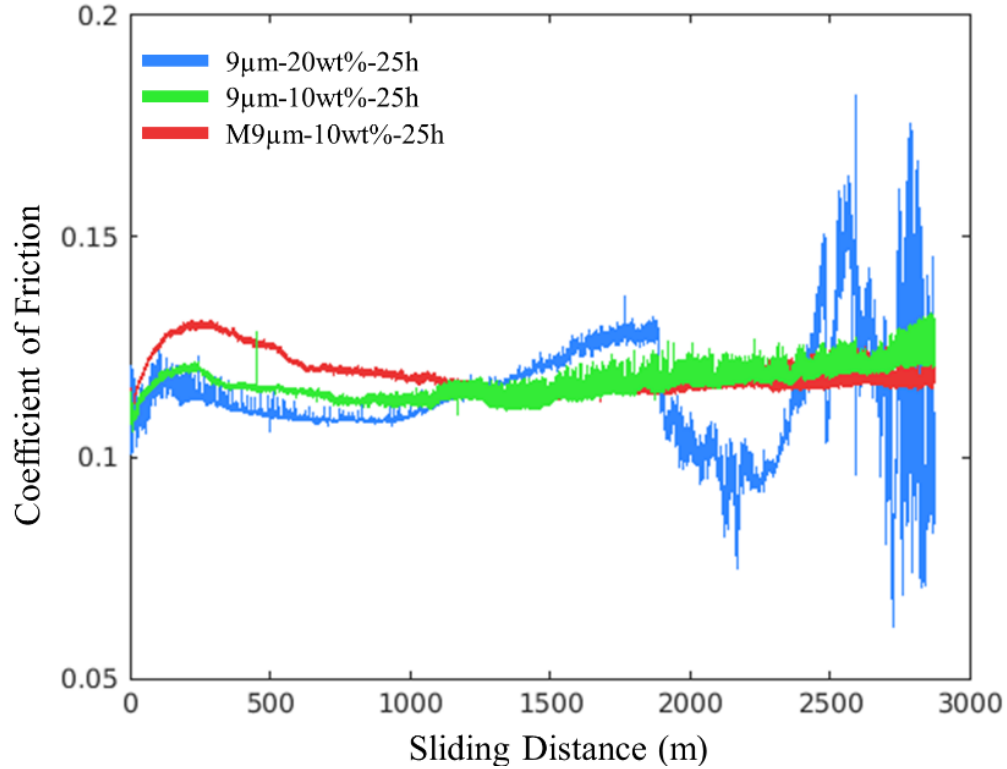


Figure 4.23 The variation of the coefficient of friction with respect to sliding distance for composite-coated samples: 9µm-20wt%-25h, 9µm-10wt%-25h, M9µm-20wt%-25h.

The average COF's of all the tested samples were calculated from the steady-state regions and shown in Figure 4.24. The average COF values (0.10-0.13) are all very similar and fall within the range for PFA on steel (0.1-0.2) [42]. The samples containing 20 wt% filler display slightly lower COF values, with the 44µm-20wt%-25h sample being the lowest. The 10 wt% sample diluted with unprocessed PFA particles (M9µm-10wt%-25h) exhibits a slightly higher average COF than the undiluted sample (9µm-10wt%-25h). The MF-MLG-2g-10wt% sample shows the highest COF during steady state.

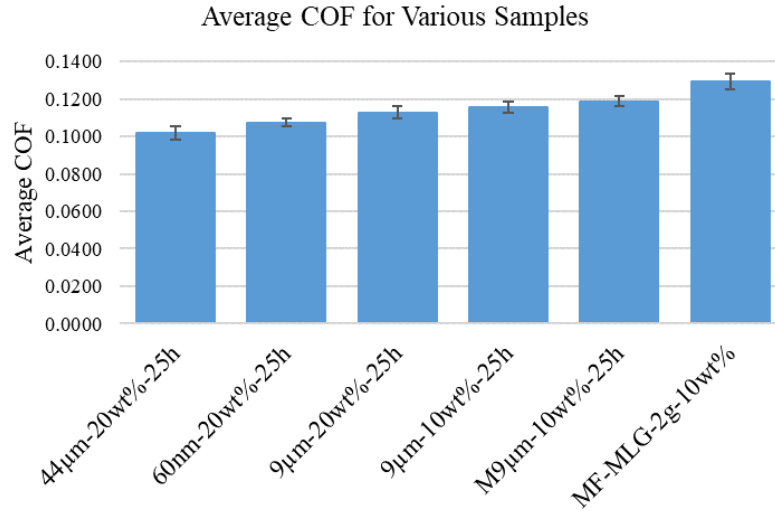


Figure 4.24 The average coefficient of friction in the steady-state region (9µm-20wt%-25h: ~250m to 1750m; 44µm-20wt%-25h: ~250m to 2125m; 9µm-10wt%-25h and M9µm-10wt%-25h: ~250m to 2500m; 60nm-20wt%-25h and MF-MLG-2g-10wt%: ~250m to 2800m) for composite-coated samples during pin-on-disk wear testing.

The coated samples and stainless steel counter-face were weighed before and after testing. The calculated mass loss or gain after testing is shown in Table 4.3. Micrographs for the corresponding counter-face stainless steel balls are shown in Figure 4.25. All the coupons experienced a decrease in mass after wear testing, indicating wear of the coating. The 9µm-20wt%-25h sample displayed the highest coupon mass loss and counter-face wear (Fig. 4.25a). Generally, the composite samples containing 10 wt% filler showed the lowest wear for composite coatings, except for the MF-MLG-2g-1wt% sample which had the second highest mass loss. Scratch marks along the sliding direction are observed on all the worn surfaces of counter-face samples (Figure 4.25). Dark patches of wear debris are also shown adhered to the counter-face surface, as shown in Figure 4.25c. Wear debris adhered to the counter-face may balance out the mass loss, or even result in the counter-face balls displaying a mass gain after testing.

Table 4.3 The mass loss or gain of both the composite-coated samples and the stainless steel counter-face ball.

Sample Name	Mass Loss/ Gain (g)	
	Coupon	Ball
60nm-20wt%-25h	-0.0102	0.0000
9 μ m-20wt%-25h	-0.0145	-0.0003
44 μ m-20wt%-25h	-0.0100	-0.0004
9 μ m-10wt%-25h	-0.0099	0.0003
M9 μ m-10wt%-25h	-0.0100	0.0004
MF-MLG-2g-10wt%	-0.0117	0.0000

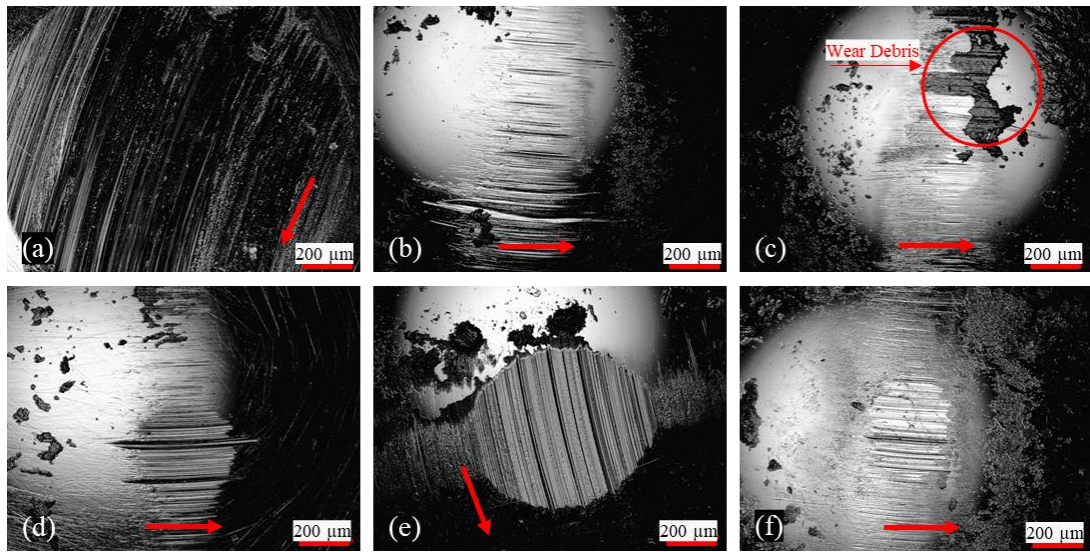


Figure 4.25 Micrographs of the stainless steel counter-face balls after wear testing: (a) 9 μ m-20wt%-25h, (b) 9 μ m-10wt%-25h, (c) M9 μ m-10wt%-25h, (d) 44 μ m-20wt%-25h, (e) 60nm-20wt%-25h, (f) MF-MLG-2g-10wt%. The red arrow indicates the sliding direction.

Following pin-on-disk testing, the wear tracks were analyzed using a laser/optical microscope to extract the wear track profiles, as described in section 3.4.4.1. The calculated wear area, wear volume, and wear rates for all the worn samples are shown in Table 4.4. The volumetric wear rate with respect to sliding distance is further illustrated in Figure 4.26. The composite samples containing 10 wt% filler showed consistently lower wear rates than the samples with 20 wt% filler. The 9 μ m-10wt%-25h sample displayed the

lowest wear rate, followed by the M9 μ m-10wt%-25h sample, and then MF-MLG2g-10wt%. The wear rate for the 20 wt% composite samples directly correlated to the coupon mass loss; the 9 μ m-20wt%-25h sample has the highest wear rate, followed by the 60nm-20wt%-25h, and then the 44 μ m-20wt%-25h sample. The three-dimensional optical/laser micrographs of all the worn samples are shown in Figure 4.27. Very severe abrasive wear is observed on the 20 wt% samples (Figs. 4.27 a, d, e), as indicated by the large height difference between the coating surface and the wear track.

Table 4.4 The average wear area, wear volume, and corresponding wear rate (in terms of volume removed over sliding distance) for various composite-coated samples after pin-on-disk wear testing.

Sample	Wear Area (μm^2)	Wear Volume (mm^3)	Wear Rate (mm^3/m)
60nm-20wt% -25h	425915.21	10.84	3.76×10^{-3}
9 μ m-20wt% -25h	649821.23	16.54	5.74×10^{-3}
44 μ m-20wt% -25h	347368.82	8.84	3.07×10^{-3}
9 μ m-10wt% -25h	139977.77	3.56	1.24×10^{-3}
M9 μ m-10wt% -25h	169461.10	4.31	1.50×10^{-3}
MF-MFG-10wt% -25h	213512.33	5.43	1.89×10^{-3}

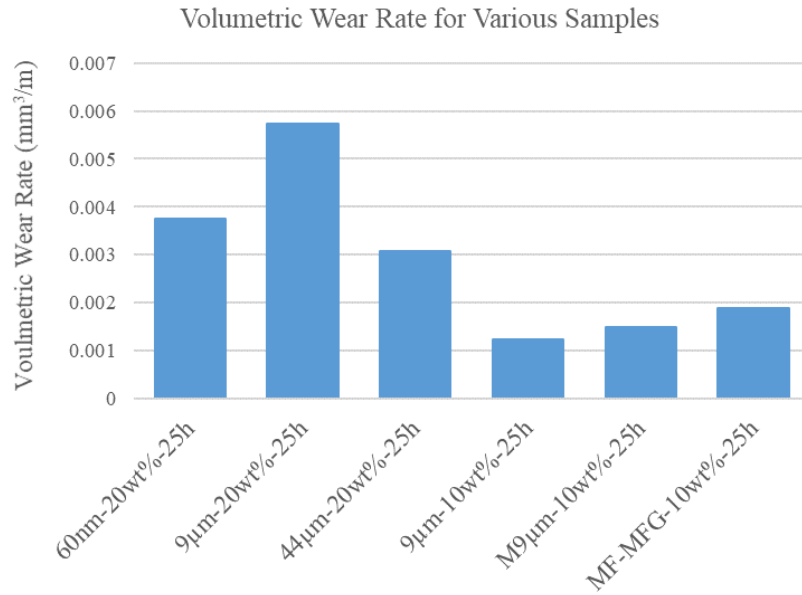


Figure 4.26 The average volumetric wear rate (in terms of volume removed over sliding distance) for various composite-coated samples after pin-on-disk wear testing.

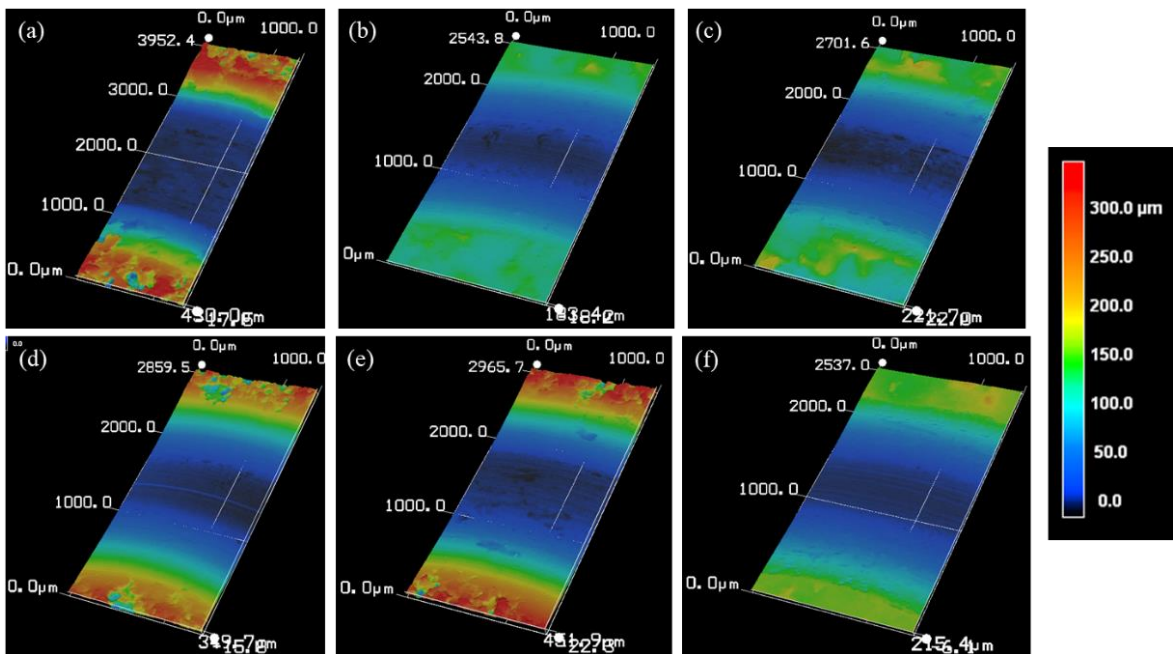


Figure 4.27 Three-dimensional optical/laser profiles of the wear tracks on the composite-coated samples: (a) 9µm-20wt%-25h, (b) 9µm-10wt%-25h, (c) M9µm-10wt%-25h, (d) 44µm-20wt%-25h, (e) 60nm-20wt%-25h, (f) MF-MLG-2g-10wt%.

4.4.2 Microscopy Analysis of Worn surfaces

Back-scattered electron (BSE) images of the wear tracks of various samples are shown in Figure 4.28. Coating delamination can be identified in BSE images, typically illustrated as lighter patches within the coating (indicating a different material, i.e., stainless steel substrate). Coating delamination is further examined via EDS for each sample. It is observed that the samples containing 20 wt% filler (both graphite and graphene) are significantly more worn compared to the 10 wt% samples, as exemplified by large patches of lighter areas at the centre of the wear track for both the 60nm-20wt%-25h and 9 μ m-20wt%-25h samples. The wear track in the 20 wt%-filler coatings is readily distinguished as the rough surface finish appears significantly smoother on the worn areas. Conversely, the wear track in the 10 wt%-filler samples is more difficult to distinguish as the coating surface finish is relatively smooth, and no major material pile-ups or coating deformation occurs at the edge of the track.

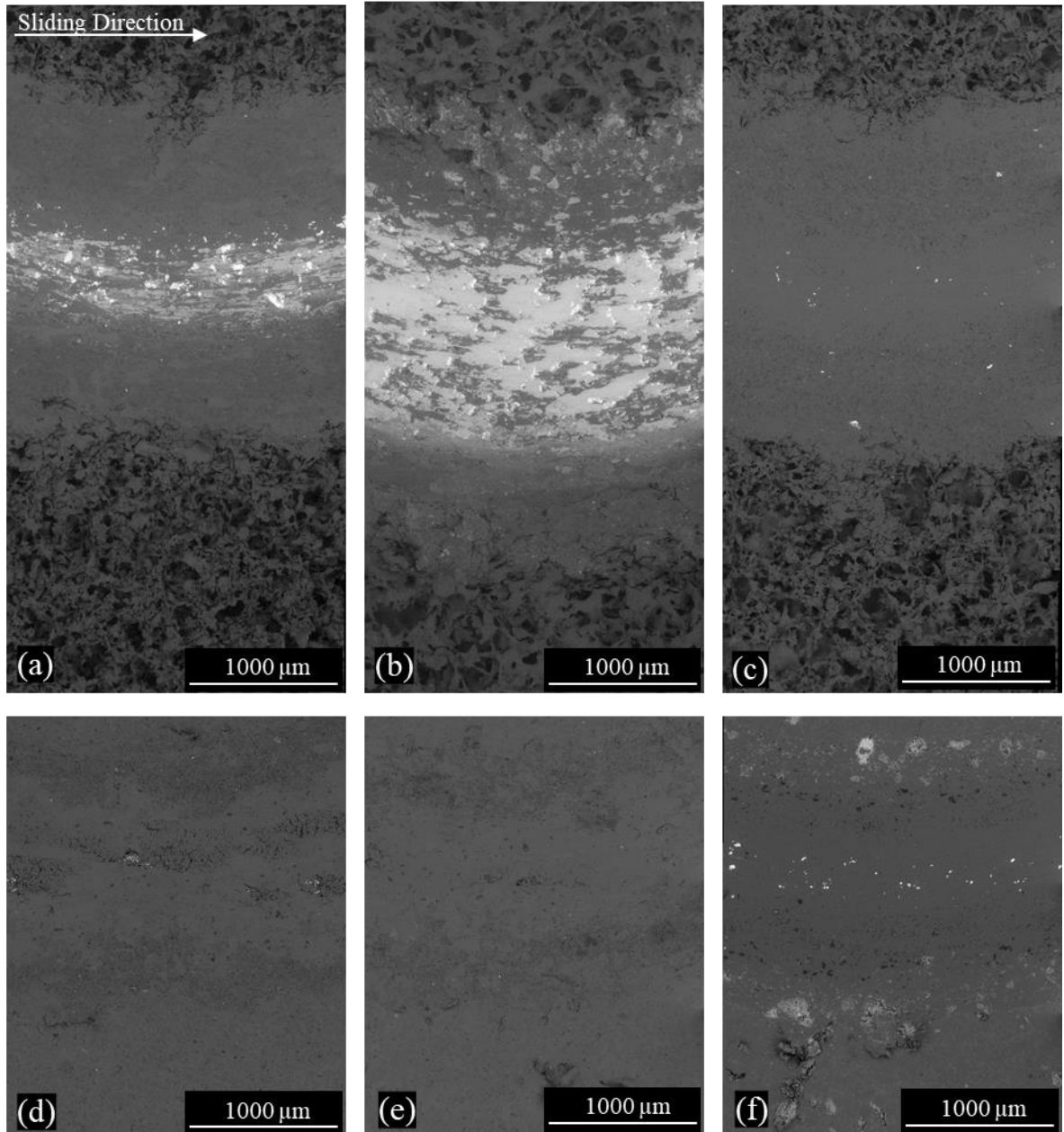


Figure 4.28 Backscattered electron (BSE) images of wear tracks on the surfaces of composite coatings after 8 hours of testing: (a) 60nm-20wt%-25h, (b) 9μm-20wt%-25h, (c) 44μm-20wt%-25h, (d) 9μm-10wt%-25h, (e) M9μm-10wt%-25h, and (f) MF-MLG-2g-10wt%.

SEM images of the wear track on the 60nm-20wt%-25h coated sample are shown in Figure 4.29. The secondary electron (SE) image reveals significant smoothing of the coating at the wear track edges, and rougher patches near the center of the wear track, as

characterized by severe wear and coating failure in the form of cracking (Figs. 4.29 a, c). BSE images at the severely worn areas display 3 different material phases (Fig 4.29b), and EDS analysis was performed to determine their compositions. The light gray/ white patches (EDS Spot 1) contain iron, chromium, silicon, aluminum, and nickel elements present in the substrate material), and traces of fluorine, sulfur, carbon, and oxygen (elements present in the PFA primer layer). The medium gray (EDS Spot 2) patches contain a mixture of elements from the substrate material (iron, chromium), and traces of the primer layer (fluorine, sulfur, carbon, and oxygen). Lastly, the dark gray patches (EDS Spot 3) are composed of PFA top layer (fluorine, carbon, and oxygen), and traces of iron (substrate material).

Figure 4.30 shows SEM images of the wear track on the 9 μ m-20wt%-25h sample. The SE image displays smoothing of the coating at the outer edges of the wear track, severe abrasive wear at the center of the wear track, and coating failure through tearing and fibrillation of the polymer (Figs. 4.30 a, c). Three different material phases were observed in the BSE image at the center of the wear track (Fig. 4.30b). The light gray, medium gray, and dark gray phases displayed similar compositions to the phases observed in the 60nm-20wt%-25h sample. The light gray patches (EDS Spot 2) contain elements from the substrate (iron, chromium, silicon, aluminum, nickel), and traces of the PFA primer layer (fluorine, sulfur, carbon, and oxygen). The medium gray patches (EDS Spot 1) contain a mixture of substrate material (iron), and the PFA top layer (fluorine, carbon, and oxygen). Conversely, the dark gray phase (EDS Spot 3) is composed of the PFA primer layer (fluorine, sulfur, carbon, and oxygen), and traces of the substrate material (iron).

SEM images of the wear track on the 44 μm -20wt%-25h coating are shown in Figure 4.31. The SE image displays smoothing of the coating on the worn surfaces, and small cracks within the coating near the center of the wear track (Figs. 4.31 a, c). Two phases are observed in the BSE images of the coating, as further examined through EDS (Fig. 4.31b). The light gray fragments (EDS Spot 1) contain elements from the substrate material (iron, chromium, aluminum), and traces of the PFA primer layer (fluorine, carbon, oxygen, and sulfur). The dark gray area (EDS Spot 2) is the PFA primer layer (fluorine, sulfur, carbon, and oxygen).

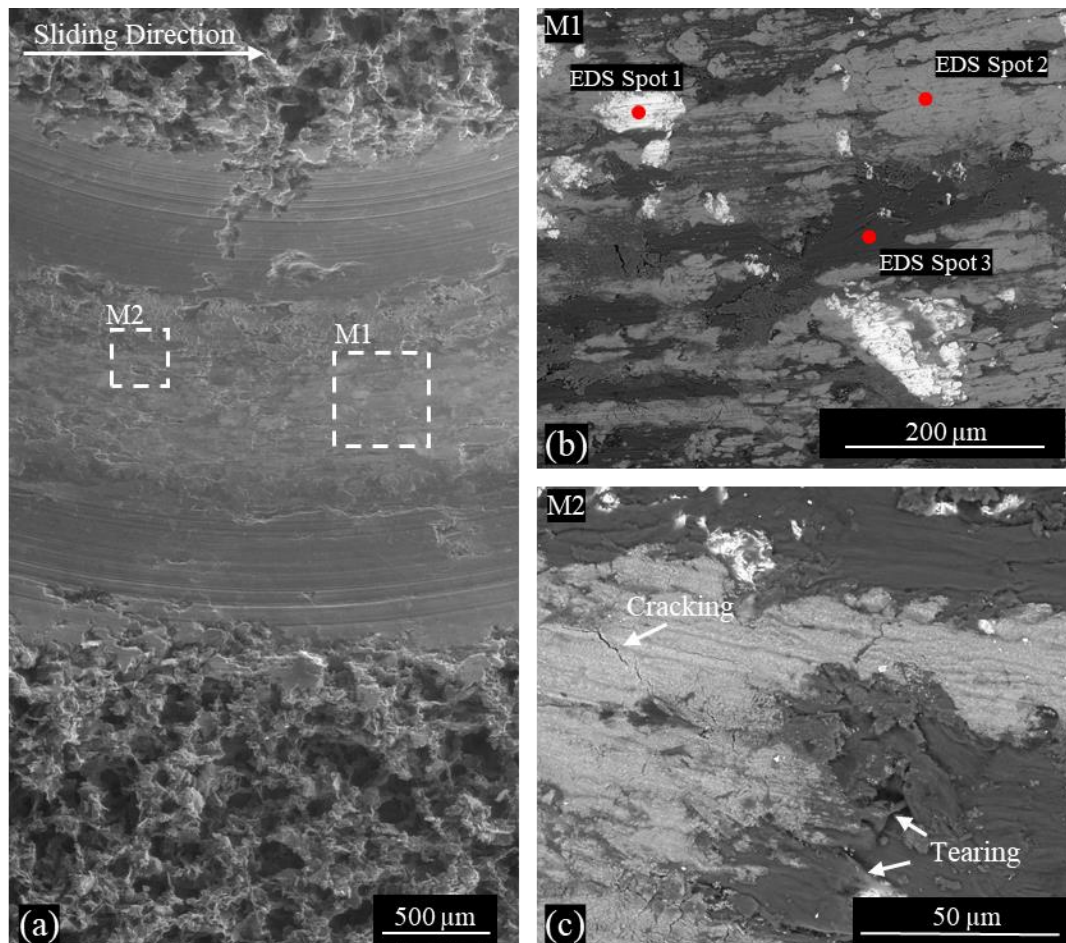


Figure 4.29 SEM images of the wear track on the 60nm-20wt%-25h coated sample: (a) SE image of the wear track, (b) a higher magnification BSE image of the area ‘M1’ outlined in (a), with EDS spectra taken at the 3 locations indicated (EDS Spot 1: Fe, Cr, Si, Al, Ni, F, S, C, O; EDS Spot 2: Fe, Cr, F, S, C, O; EDS Spot 3: F, C, O, Fe), (c) a higher magnification BSE image of the area ‘M2’ outlined in (a), showing coating failure in the form of cracking and tearing.

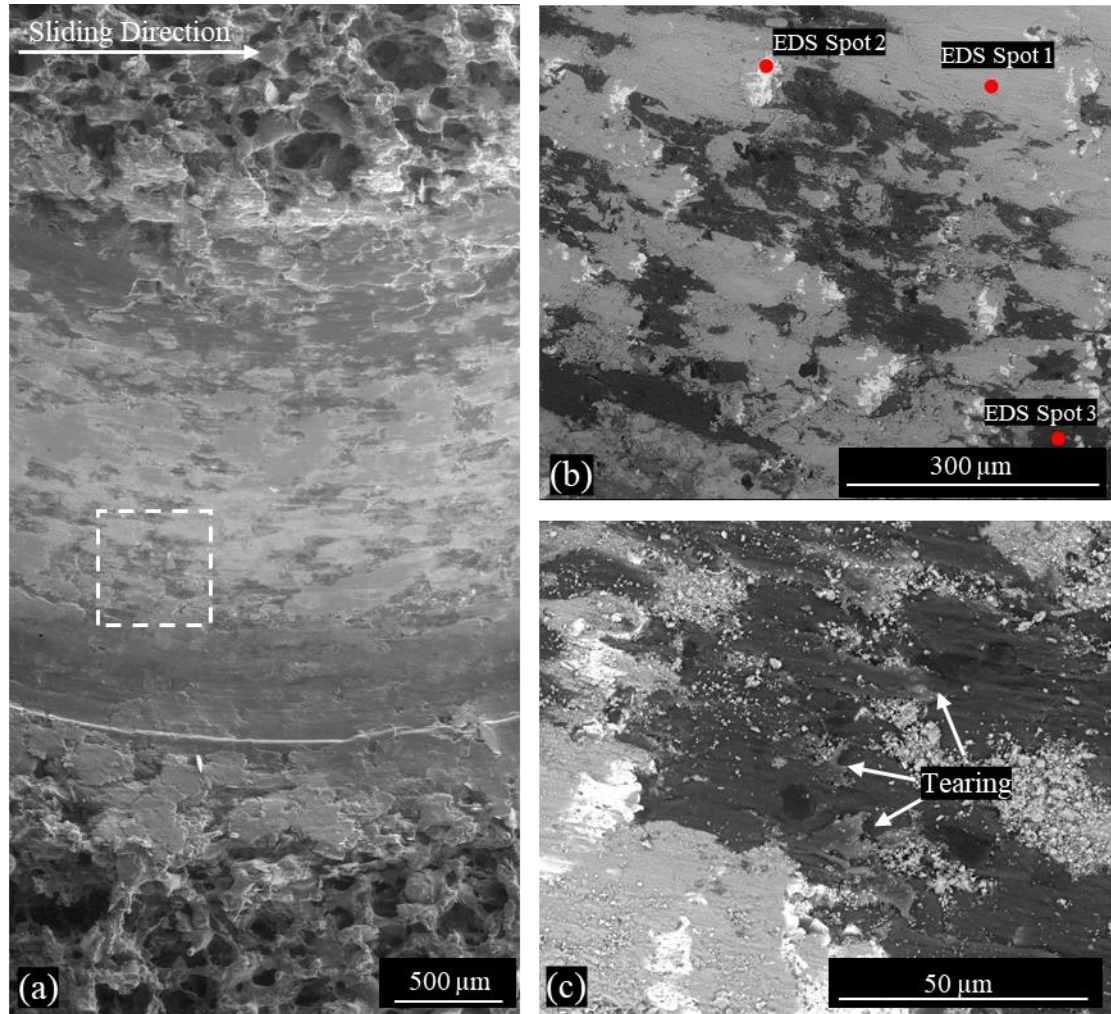


Figure 4.30 SEM images of the wear track on the 9 μm -20wt%-25h coated sample, (a) SE image of the wear track, (b) a higher magnification BSE image of the area outlined in (a), with EDS spectra taken at the 3 locations indicated (EDS Spot 1: Fe, F, C, O; EDS Spot 2: Fe, Cr, Si, Al, Ni, F, S, C, O; EDS Spot 3: F, S, C, O, Fe), (c) an even higher magnification BSE image of the area outlined in (a), showing coating failure in the form of tearing.

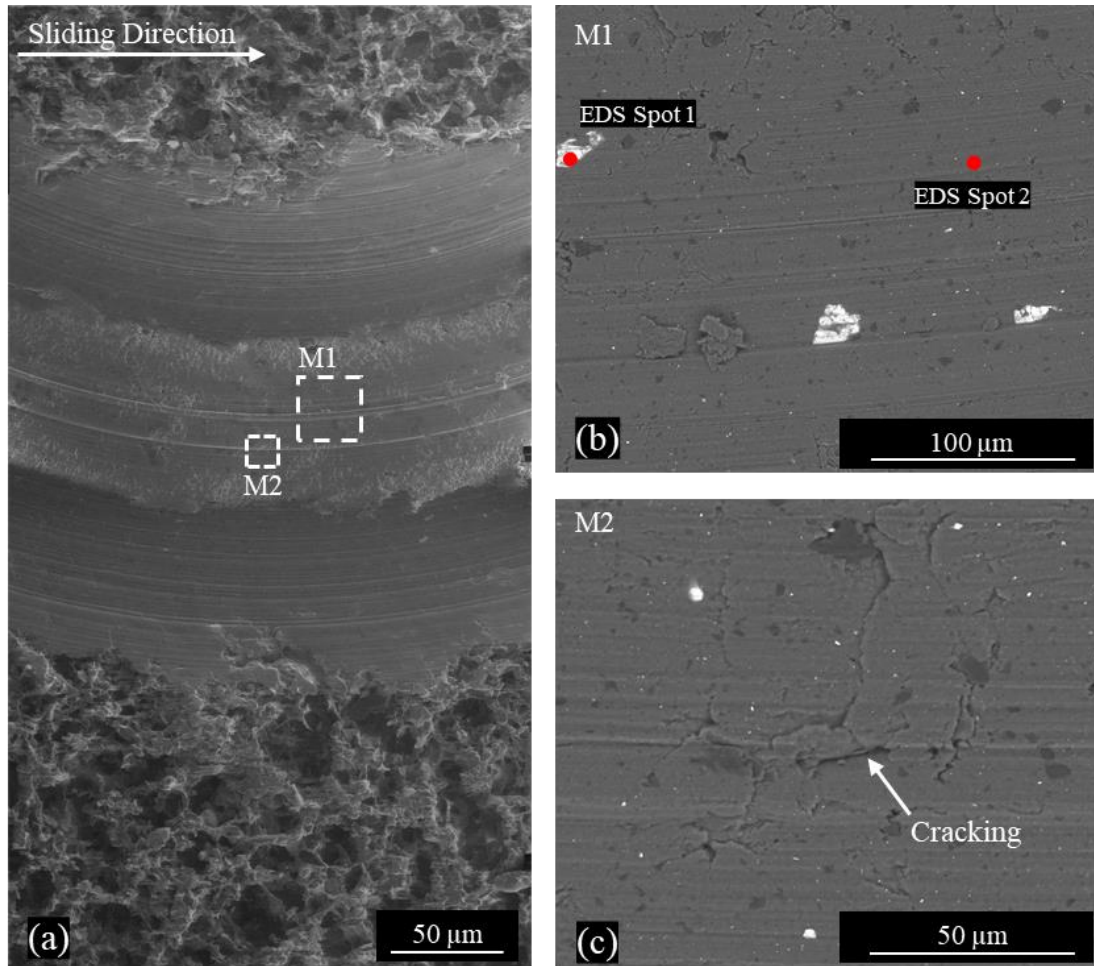


Figure 4.31 SEM images of the wear track on the 44 μ m-20wt%-25h coated sample: (a) SE image of the wear track, (b) a higher magnification BSE image of the area ‘M1’ outlined in (a), with EDS spectra taken at the 2 locations indicated (EDS Spot 1: Fe, Cr, Al, F, C, O, S; EDS Spot 2: F, S, C, O), (c) a higher magnification SE image of the area ‘M2’ outlined in (a), showing coating failure in the form of minor cracking.

SEM images for the composite coatings containing 10-wt% 9- μ m graphite filler are shown in Figure 4.32. The 10-wt% composites have significantly thinner wear tracks and are characterized by less abrasive wear as compared to the 20-wt% filler composite coatings. Figure 4.32a displays the SE image of the wear track on the 9 μ m-10wt%-25h coating. A higher magnification BSE image reveals coating failure through tearing and polymer fibrillation (Fig. 4.32b). The EDS spectra of the light gray specks (EDS Spot 2) is

composed of both the substrate (iron, chromium, aluminum, nickel), and PFA primer (fluorine, sulfur, carbon, and oxygen) (Fig. 4.32b). Figure 4.32c displays the SE image of the wear track on the M9 μ m-10wt%-25h coating. Less abrasive wear was observed on the diluted 9- μ m composite coating; a high magnification BSE image at the center of the wear track reveals only minor tearing and cracking (Fig. 4.32d).

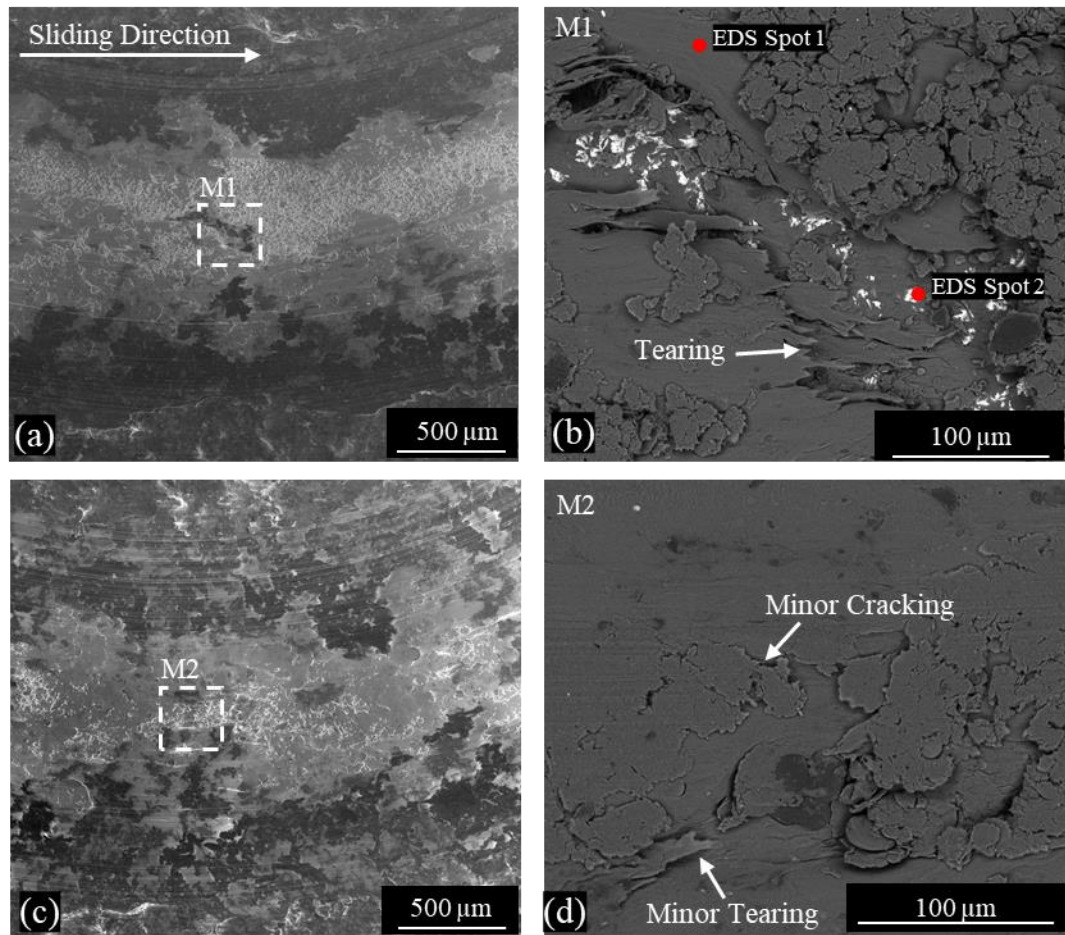


Figure 4.32 SEM images of the composite-coating containing 10 wt% 9 μ m graphite filler: (a) SE image of the wear track on the 9 μ m-10wt%-25h coating, (b) a higher magnification BSE image of the area 'M1' outlined in (a), displaying coating failure in the form of tearing, (c) SE image of the wear track on the M9 μ m-10wt%-25h coating, and (d) a higher magnification BSE image of the area 'M2' outlined in (c), displaying coating failure in the form of minor tearing and cracking.

Figure 4.33a shows the SE image of the wear track on the MF-MLG-2g-10wt% coating. The outside edges of wear track appear smooth, followed by an inner edge characterized by several large cracks within the coating, as shown in higher magnification in Figure 4.33b. In contrast, a high magnification BSE image reveals that the center of the wear track is very smooth with fine cracks and light gray specks (Fig. 4.33c). EDS spectrum indicates that the light gray specs (EDS Spot 2) are composed of the substrate elements (iron, chromium, aluminum, nickel), and traces of the primer layer (fluorine, sulfur, carbon, and oxygen).

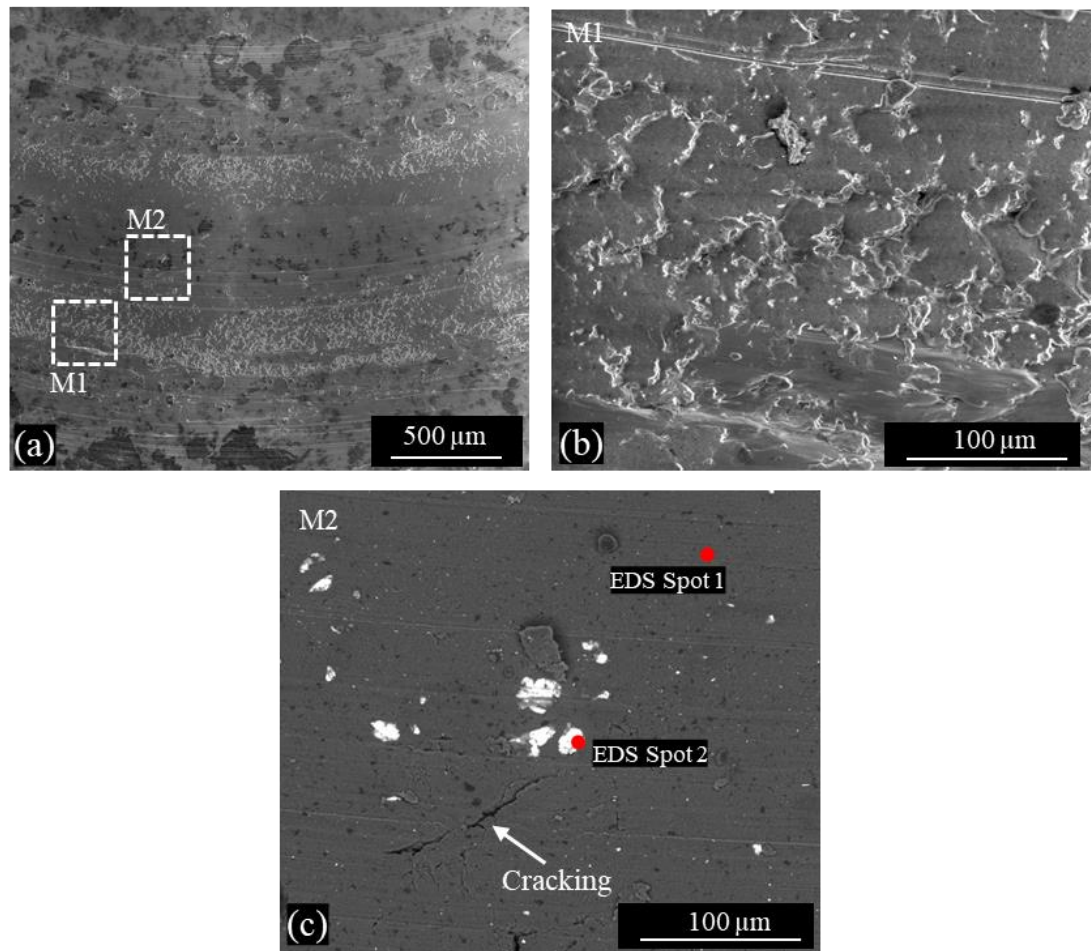


Figure 4.33 SEM images of the wear track on the MF-MLG-2g-10wt% composite coatings: (a) SE image of the wear track, (b) a higher magnification SE image of the area ‘M1’ outlined in (a), displaying large cracks within the coating, (c) a higher magnification BSE image of the area ‘M2’ outlined in (a), displaying fine cracks within the coating.

4.5 Raman Spectroscopy Results

Raman spectroscopy was performed on the graphite/graphene particles in the ball milled composite samples according to section 3.4.5. The estimated number of graphene layers (N_G), and defect intensity ratios (I_D/I_G) were calculated from the Raman spectra. The main graphite peaks (D peak at $\sim 1350\text{ cm}^{-1}$, G peak at $\sim 1580\text{ cm}^{-1}$, and 2D peak at $\sim 2700\text{ cm}^{-1}$ [10]) for the milled graphite particles are shown in Figure 4.34 and 4.36. All samples also exhibit a Rayleigh peak at the beginning of the Raman spectra however, this peak is not one of peaks used to characterize graphite and is not further analyzed.

The Raman spectra for the graphite/graphene particles in the composite samples with 20 wt% filler that underwent balling for various lengths of time (0 – 30 hours) are shown in Figure 4.34. The corresponding (estimated) number of graphene layers (N_G) and I_D/I_G ratios are summarized in Figure 4.35. The Raman spectra for the 60 nm MLG (Fig. 4.34a) shows no distinctive change in any of the peaks with the increase of milling time. The Raman spectra for the 9 μm graphite (Fig. 4.34b) shows no major changes in the 2D band with respect to the milling time. However, a distinctive increase in the D-band intensity is observed for milling times greater than 5 hours. This is also reflected in the I_D/I_G ratios (Fig. 4.35b), as the defect intensity ratio significantly increases after 5 hours of ball milling. The Raman spectra for the 44- μm sample also displays no visible changes in the 2D band, but a minor increase in the D-band intensity after ball milling, supported by the corresponding defect intensity ratios (Fig. 4.35b).

The Raman spectra for the three different filler materials after ball milling for 25 hours are compared in Figure 4.34d. Single layer graphene has a distinctive 2D band that has a larger intensity than the G band. The 2D band for the milled samples displayed a

much lower intensity than the G band, indicating that the ball milling process did not produce single layer graphene. The number of graphene layers was estimated (Fig. 4.35a), and all samples displayed very similar values. The 9- μm graphite had the lowest estimated number of graphene layers, followed by the 44- μm graphite, and then the 60-nm MLG. The D-band for the milled samples slightly increased as the initial particle size increased. However, no distinct trend is observed when comparing the defect intensity ratios (I_D/I_G) of the three different filler types.

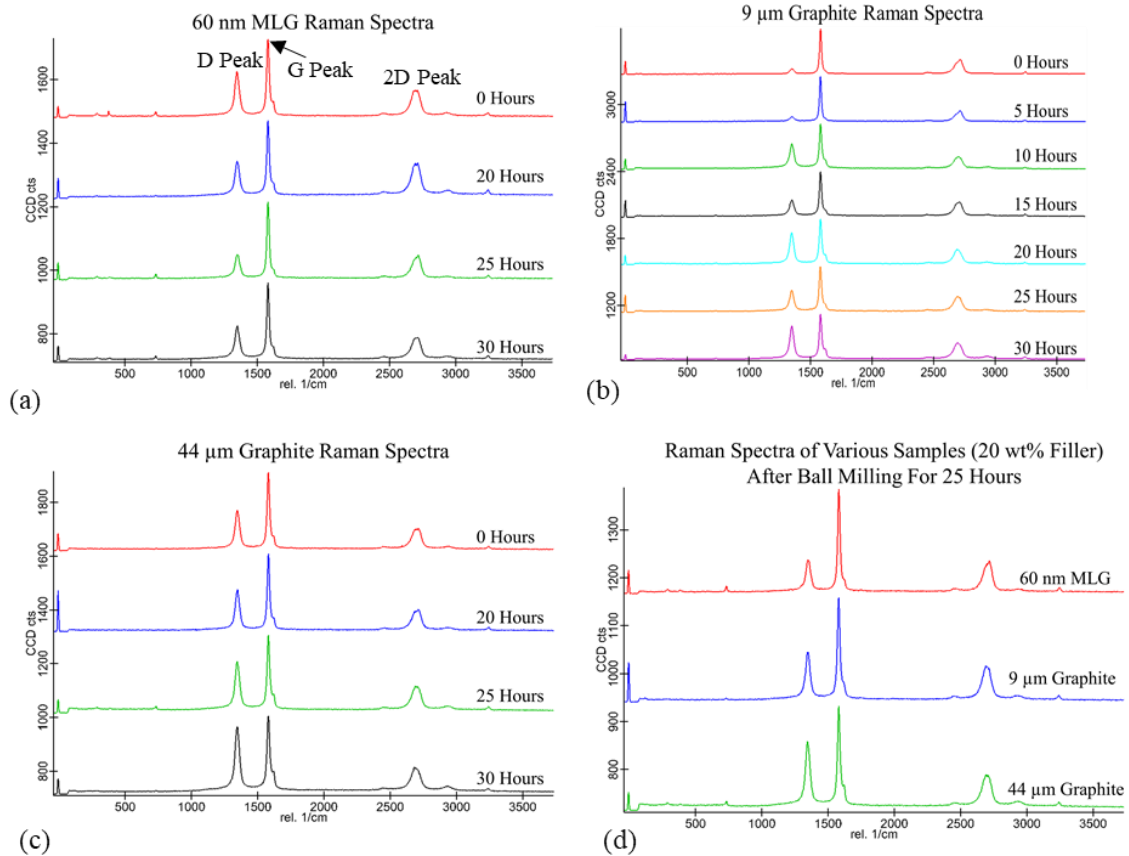


Figure 4.34 The Raman Spectra of graphene/graphite in composite samples containing 20 wt% filler ball milled for 0-30 hours. The graphs display the effect of ball milling time on the graphene particles: (a) 60 nm MLG, (b) 9 μm graphite, and (c) 44 μm graphite, (d) comparison of all three filler materials after 25 hours of ball milling.

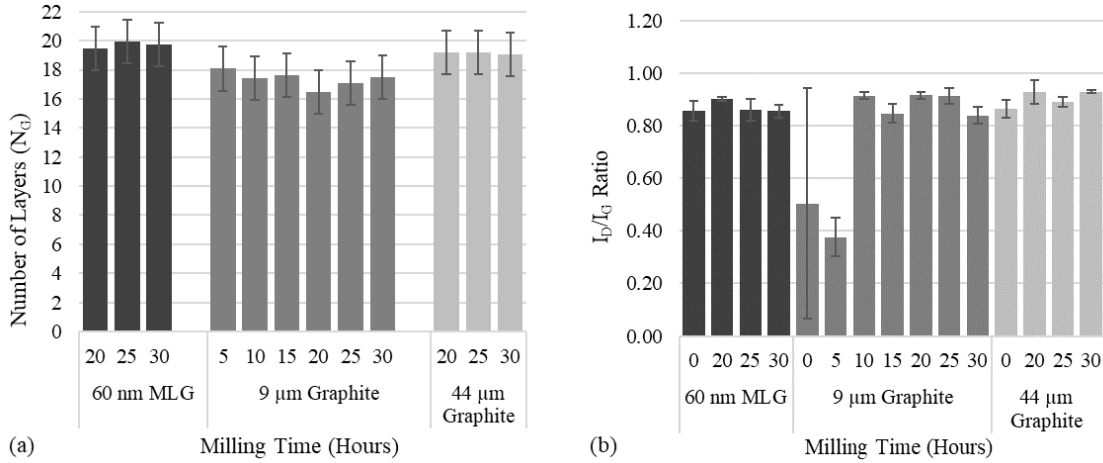


Figure 4.35 Raman spectra analysis for the PFA composite samples with increasing ball milling times showing: (a) the number of graphene layers (N_G), and (b) the I_D/I_G ratio.

The Raman spectra of the graphite/graphene particles within the PFA composites with various filler weight fractions are shown in Figure 4.36. None of the filler materials shows a correlation between the D band intensity, or the I_D/I_G ratio, and filler weight fraction (wt%). Furthermore, none of the filler materials shows a correlation between the 2D-band shape/intensity, or the estimated number of graphene layers (N_G), and the filler weight fraction (wt%). The estimated number of graphene layers (Fig. 4.37a) for the 10-20 wt% composite samples ball milled for 25 hours is the lowest for the 9 μm graphite, followed by the 44 μm graphite, and then the 60 nm MLG. However, the number of graphene layers is an estimation and has a reported accuracy of ± 1.5 graphene layers [131], thus all samples are considered to be very similar in thickness.

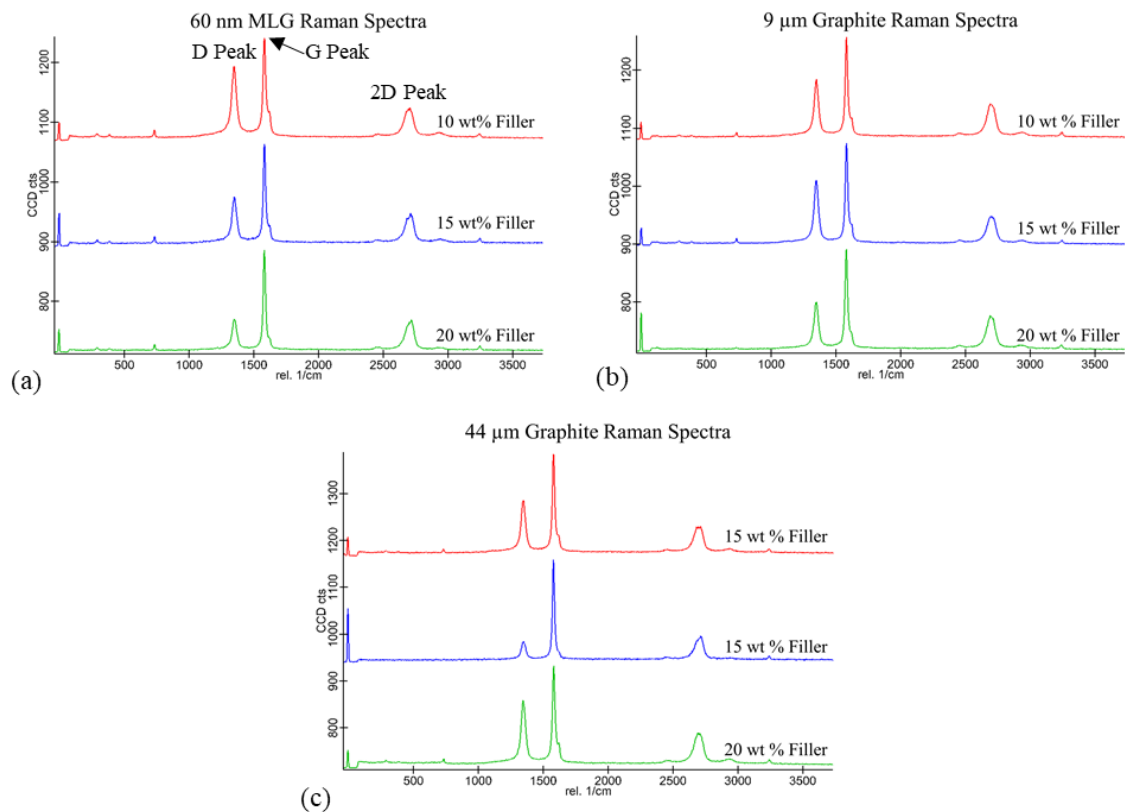


Figure 4.36: The Raman Spectra of graphene/graphite in composite samples ball milled for 25 hours. The graphs display the effect of filler weight fraction (10, 15, and 20 wt% filler) on the graphene particles: (a) 60 nm MLG, (b) 9 μm graphite, and (c) 44 μm graphite.

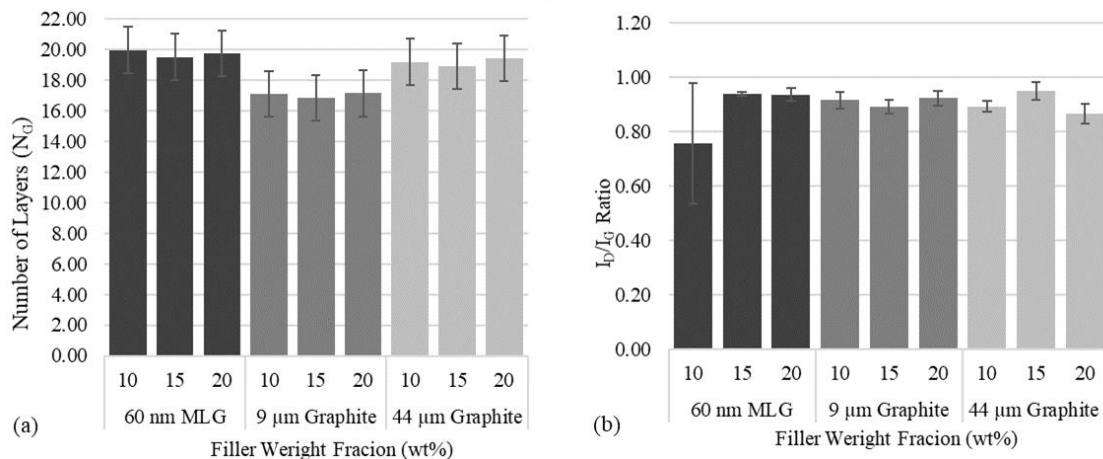


Figure 4.37 Raman spectra analysis for the PFA composite samples with increasing filler weight fractions showing: (a) the number of graphene layers (N_G), and (b) the I_D/I_G ratio.

CHAPTER 5: DISCUSSION

The following sections discuss the experimental results presented in Chapter 4 and their significance in relation to the overall objectives of the study. The discussion is divided into three sections. The first section discusses the composite phase distribution, surface topography, and the corresponding Raman spectra. The second section explains the thermal property results, focusing on the impact of the processing methods on the resulted thermal conductivity of the composites. The third section discusses the wear results, including the wear rate and coefficient of friction, the effects of the different filler materials, filler weight percentage, and processing methods on the overall tribological behaviour of the composite.

5.1 Composite Morphology

5.1.1 Effect of Ball Milling on Filler Particle Alignment and Distribution

Micrographs of the compression-molded PFA composites shown in Figure 4.1 – 4.4 display distinct changes in the sample microstructure before and after ball milling. Ball milled samples exhibit improved filler particle distribution, and visible alignment of graphite and MLG filler particles in the lateral direction. Particle alignment occurs perpendicular to the pressing direction, as shown in Figure 5.1. Related research on preparing graphene polymer composites in situ via ball milling do not show alignment of MLG filler particles [10], [84], [96], [97]. However, in papers studying graphite-polymer composites, it was reported that graphite flakes have a tendency to orient perpendicular to the pressing direction in compression-molded samples [133]–[135]. Furthermore, other researchers have observed self-alignment of graphene in polymer composites when incorporating graphene-oxide and reduced-graphene-oxide particles with large surface area and strong interfacial interaction with the matrix polymer [136], [137].

Research has shown that incorporating graphite filler particles via ball milling improves the compatibility at the graphite-polymer interface [10], [84], [96], [97]. Observation of the ball-milled composite powder mixtures through SEM (Fig 4.11- 4.12) reveals that the graphite particles are well combined with the PFA particles such that the graphite and PFA particles are essentially indistinguishable. EDS mapping (Fig. 4.13) further indicates a strong interfacial interaction between the graphite and PFA particles as the large clusters of carbon (graphite particles) contain traces of fluorine (from PFA), and consistent particle morphology is maintained amongst both the graphite and PFA particles. Thus, the particle alignment may be attributed to the compression molding process (in compression-molded samples), large flake-like graphite particle morphology, and the compatibility of the graphene-polymer interface.

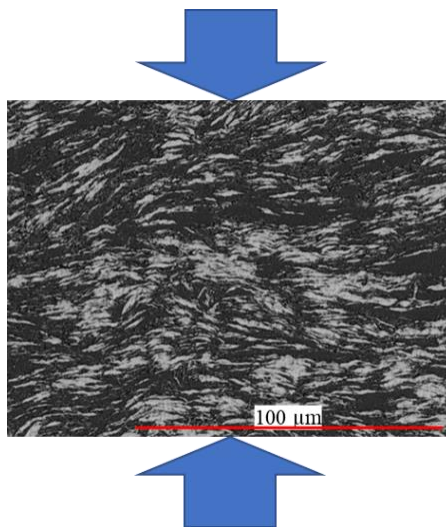


Figure 5.1 The laser/optical micrograph of the PFA- 60nm MLG sample, with arrows indicating the pressing direction in compression-molding.

Similar to previous studies [10], [96], the SEM results support the observation that the ball-milled graphite particles are lightly coated with the polymer, thus preventing re-

agglomeration of graphite particles during curing. This is evident in the microscopy of both the compression-molded (Fig. 4.11-4.12) and electrostatically coated samples (Fig. 4.7-4.9), as the graphite particles are evenly distributed with no major observable agglomerates. However, minor particle stacking between some of the filler particles is observed in the 60nm-20wt%-25h and 9 μ m-20wt%-25h samples, likely due to the excellent particle distribution and small particle size. Micrographs of the undiluted samples containing 10 wt% 9 μ m graphite (9 μ m-10wt%-25h) display visibly better graphite dispersion as compared to the diluted sample (M9 μ m-10wt%-25h). Gaps of plain PFA surrounded by a loose network of graphite particles are observed in micrographs of the sample diluted with unprocessed PFA (M9 μ m-10wt%-25h). Therefore, incorporating PFA during ball milling results in excellent filler particle dispersion as compared to traditional filler incorporation methods, such as blending composite powders in a tumbler mixer.

5.1.2 Effect of Compression Molding Versus Electrostatic Coating on Microscopy

It has been shown that the area percent of filler, quantitatively analyzed using the ImageJ software, was significantly higher in the compression-molded samples than in the electrostatically sprayed coupons with the same filler weight percentages. This effect was also observed in graphene-polymer composites in a previous study conducted by this research group [8]. The compression has a more significant impact on PFA than on the filler particles as polymers are significantly softer and more deformable than the graphite/MLG filler materials. As PFA is compressed, its area percent decreases; subsequently, the area percent of the graphite/MLG filler increases as it is not easily compressed during molding. During electrostatic spraying, the PFA particles are not

compressed so they take up a larger area percent; therefore, the apparent area percent of graphite/MLG filler is decreased compared to in the compression-molded samples.

Compression molding contributes to the alignment of the graphite filler particles in graphite-polymer composites [133]–[135]. Consequently, filler alignment is visibly more ordered in the compression-molded samples than in the electrostatically coated samples. Nonetheless, the electrostatically coated samples still display slight alignment of filler particles along the lateral direction. The large aspect ratio of the graphite particles and their strong interfacial interaction with the PFA matrix aid the filler alignment [136], [137]. Moreover, the electrostatic spray coating process favours the lateral alignment of graphite filler particles. Electrostatic spraying imposes a negative charge on the blended powder mixture, which is subsequently attracted to the grounded substrate. Graphite particles have a high aspect ratio, thus the face with the larger surface area has a greater electrostatic charge and assists in the alignment of the graphite particles when attracted to the ground substrate. As a result, the particles are normally aligned with the longitudinal direction parallel to the substrate surface since the surface area is larger along the long axis.

5.1.3 Effect of MF-MLG Particles on Composite Microstructure

Micrographs of the compression-molded disks and electrostatically sprayed coupons containing the MF-MLG particles are shown in Figure 4.5 and Figure 4.9, respectively. Although the MF-MLG particles were responsive to an external magnetic field, as shown in Figure 3.2, the micrographs of the cured samples show no signs of filler particle alignment. The MF-MLG particles formed large agglomerates within the cured PFA matrix, similar to the SEM images of the uncured MF-MLG particles (Fig. 4.14).

Despite the MF-MLG particles not resulting in filler alignment within the cured composite samples, the technique is still promising for future work as the particles respond to an external magnetic field. Success in magnetically aligned graphene particles has been demonstrated using liquid based resin polymers [13], [95], [111], whereas in this work powdered PFA was used as the matrix. A few factors may have affected the alignment of the MF-MLG particles in the desired direction: (a) the PFA powder may have restricted the movement of the MF-MLG particles and prevented alignment, and (b) the aligned particles may have shifted as the polymer melted, as the permanent magnet was not graded for high temperature use and was removed before heating and curing.

Suggested future work includes: (i) investigate the use of paint slurry based PFA coatings as the matrix, which may facilitate the alignment of the particles as illustrated in the literature with liquid mediums; (ii) use electromagnets instead of permanent magnets to apply the magnetic field, which may be applied even at the melting temperature of the PFA; (iii) control the field strength of the magnets during the coating process so that the particles can be aligned as they are sprayed onto the substrate. Furthermore, the Curie temperature of the magnetic nanoparticles is well above the processing temperature used during curing so the particles will maintain their magnetic properties [138], [139].

5.1.4 Effect of Filler Particles on Surface Topography

The surface roughness of the electrostatically coated samples is influenced by both the filler particle size and weight fraction, as shown in Table 4.2 and Figure 4.15. The surface roughness is higher in samples with smaller initial graphite flake size and higher filler weight content. Bao et al. reported a “cross-linking density reduction effect” in graphene polymer composites. It was observed that when the graphene filler content is too

high, there is insufficient polymer to surround the graphene within the composite matrix [103]. The PFA matrix studied in the present research is a thermoplastic polymer, however, the same effect is observed. Increasing the filler weight fraction directly reduces the “cross-linking density”. Similarly, decreases in the filler particle size also reduce the “cross-linking density” as more particles are required to achieve the same filler weight fraction. The coating surface roughness increases when the cross-linking density is reduced since the filler particles are not adequately adhered within the PFA matrix.

Earlier studies conducted by this research group reported rough surfaces when the graphite content reached 30 wt% and higher [3], whereas the present work displays rough surfaces when the filler content is above 10 wt%. The effect of cross-linking density is exaggerated in polymer composites containing graphene, MLG, and graphite flakes due to the high surface area of the filler particles. This effect is further magnified in ball-milled samples as ball milling prevents the agglomeration of graphite flakes, while graphite agglomerates act as larger graphite particles within the composite. Furthermore, based on the filler area percent results (Fig. 4.10), the graphite flakes decrease in particle size after ball milling.

The composite coating containing the 10 wt% undiluted 9 μm graphite (9 μm -10wt%-25h) displays a smoother surface finish than the diluted sample with the same amount of filler (M9 μm -10wt%-25h). The increase in surface roughness in the diluted sample may be due to poorer dispersion of the graphite particles within the PFA matrix, as shown in the composite micrographs (Fig. 4.4 and Fig. 4.8).

Surface roughness influences the heat exchanger performance as rough surfaces are more prone to fouling [140], and are more difficult to clean during maintenance. Thus, rough surfaces are not suitable for heat exchanger applications. As previously studied [49], the surface finish may be improved by altering the composition of the composite for the top layer of the coating.

5.1.5 Effect of Ball Milling on Raman Spectra

Raman spectroscopy was performed on the ball-milled samples to evaluate the resulted thickness and defect intensity of the MLG and graphite filler particles after ball milling. As observed in Figure 4.34, the 2D band of all samples displays a much lower intensity than the G band, indicating that the ball milling process did not produce monolayer graphene. The number of graphene layers was estimated according to the method presented by Paton et al. [131], and all samples displayed very similar values ($\sim 20 \pm 1.5$ graphene layers).

Related literature [10], [84], [96], [97] has reported the achievement of monolayer and few layer (≥ 10 layers) graphene using an in-situ ball milling process to prepare graphene polymer composites. However, this was not achieved in the present work. Previous work using liquid resin based polymers reported that the polymer matrix protected the graphite filler particles during milling, and the mitigated milling induced defects [10], [84], [96]. The PFA matrix used in the present research is a thermoplastic polymer, and does not dissolve in the milling solution (acetone). Based on the Raman spectra and SEM micrographs of the milled graphite particles, it is postulated that the PFA matrix protected the graphite particles during milling and prevented exfoliation of graphite into monolayer graphene. Thus, the use of thermoplastic polymers may limit the ability of the ball milling

process to simultaneously exfoliate graphite particles to produce graphene while mixing the graphite particles throughout the polymer matrix.

Slight increases in the D band were observed in the Raman spectra of the ball-milled samples with increasing milling time. The defect intensity ratio (I_D/I_G) may be used to compare the quality of different graphene samples; a higher defect intensity ratio indicates that the sample contains more defects [10], [131], [132]. All samples experienced an increase in the defect intensity ratio after ball milling. However, the I_D/I_G ratio did not consistently increase with increasing milling time. The 9- μm graphite sample was ball milled from 0 to 30 hours with 5 hour increments, and a consistent increase in the I_D/I_G ratio was observed from 0 to 10 hours, followed by relatively consistent I_D/I_G ratios with further increases in milling time. Thus, it is believed that after an initial “breaking in” period the PFA matrix protected the graphite particles and no further defects were introduced.

Guo and Chen [10] observed an increase in the defect intensity ratio of graphene-polymer composites when the graphene filler content was increased, as there was less polymer matrix to protect the graphene particles. This effect was not observed in the present research, as the graphite samples did not show any clear trends between the filler weight fraction and the I_D/I_G ratio.

5.2 Thermal Properties

The incorporation of filler particles increased the thermal conductivity of the composite as compared to pure PFA, as shown in Figures 4.16 – 4.21. Consistent with

previous research, higher weight fractions of thermally conductive filler particles result in further increases in the composites thermal performance [3], [8].

Studies conducted by Guo and Chen [10] displayed increases in the composites' thermal conductivity by preparing graphite polymer composites via ball milling. Conversely, the present research displayed a decrease in the composite's thermal conductivity after ball milling, consistent among all the graphite filler materials studied. Micrographs of the composite samples produced via ball milling displayed a distinctive alignment of the graphite filler particles along the lateral direction. Graphite-based filler materials display superior thermal properties along their in-plane direction; thus, composite materials with aligned graphite filler particles experience increased thermal properties along the in-plane direction [12], [13], [95], [133], [134]. Furthermore, Yan et al. reported that the thermal conductivity of composites in the out-of-plane direction decreases as compared to composites with randomly oriented filler particles [95]. The thermal conductivity of the composites in the present research was measured in the out-of-plane direction; therefore lower thermal conductivity values were displayed. The slight increase in the defect intensity ratio after ball milling also increases phonon scattering, which may contribute to the lower thermal conductivity.

The microstructure of the composite sample containing 9- μm graphite diluted with unprocessed PFA (Fig. 4.4) influenced the resulted thermal properties. The micrograph of the composite containing 9- μm graphite (9 μm -10wt%-25h) displayed significantly better filler particle dispersion than the sample diluted with unprocessed PFA (M9 μm -10wt%-25h). The slight networking of filler particles in the diluted sampled resulted in higher thermal conductivity values than the undiluted sample. This may be due to the formation

of an interconnected network of filler particles, and the decreased orientation of the filler particles within the matrix.

The initial size of the graphite particles also influenced the composites' thermal performance; smaller filler particles resulted in higher thermal conductivities, as shown in Figure 4.17. The influence of particle size on thermal conductivity was observed before and after ball milling. However, ball milling significantly reduced the impact of filler particle size. The large graphite flakes (9 μm , and 44 μm graphite) were exfoliated during ball milling and the resulted flakes were all similar in size. This is supported by the filler area percent data, and the Raman spectra analysis of the milled graphite particles.

Kim et al. [86] reported that larger MLG particles (greater thickness and lateral dimensions) result in higher thermal conductivity values in polymer composites due to lower interface densities and phonon scattering. Conversely, the present work agrees with studies conducted by Deng et al. [135], which stated that smaller filler particles result in higher thermal conductivities. This phenomenon is attributed to the available surface area; to achieve the same weight percentage of filler, more small particles are required compared to large particles. Therefore, the combined surface area of the smaller graphite particles is higher, increasing the probability of an interconnected thermal network among graphite particles [135].

The thermal conductivity values of the composites containing the MF-MLG filler particles exhibit interesting behaviour (Fig. 4.21). From 25 °C to ~120 °C the MF-MLG composites display lower thermal conductivity values than the randomly oriented graphene. At ~120°C the thermal conductivity values become the same, which is followed

by the MF-MLG composites having higher thermal conductivity values with further increases in temperature. The lower initial thermal performance of the MF-MLG composites may be attributed to the poor filler particle dispersion and the lack of filler particle alignment, as observed through microscopy. It is important to note that the thermal performance of the MF-MLG composites is also influenced by the magnetic nanoparticles (maghemite and magnetite). The thermal conductivity of graphite decreases at an *increasing* rate as temperatures increase from 25 °C to 250 °C [141]. Conversely, the thermal conductivity of magnetite (a main component in the magnetic nanoparticles) decreases at a *decreasing* rate as temperatures increase from 25 °C to 250 °C [142]. Therefore, the magnetic nanoparticles help stabilize the thermal conductivity as the temperature increases, resulting in the breakeven point between the composite containing the randomly oriented graphene and the MF-MLG.

As described in section 5.1.2, different factors influence filler alignment in the compression-molded samples and electrostatically sprayed coupons. These differences may result in slight variations of the thermal performance of the composite. Due to instrumental restrictions, the compression-molded samples are used to analyze the thermal conductivity of the composite. This procedure is consistent with previously conducted research [3], [7], [8], and related literature [39], [73], [97], [143], [144], to characterize the bulk thermal properties of the composite. Future work may aim to identify procedures capable of measuring the thermal conductivity of the coated samples rather than the compression molded disks. Alternatively, the use of paint slurry PFA rather than PFA powder may be investigated to create molded samples without compression. The powdered samples require compression molding to remove air bubbles during curing.

5.3 Wear Behaviour of Composite Coatings

Graphite is known for its natural lubricating properties and is often used as internal lubricant in composite materials [145], [146]. Its influence on the COF of the polymer composite coatings has been shown in Figures 4.22-4.23. The graphite filler content, particle size, and dispersion all influence the tribological properties of the composite. The COF decreases when the graphite filler content increases, as observed when the filler content was increased from 10 wt% to 20 wt% in the 9- μm graphite composite coatings. Furthermore, the COF was lower in the undiluted sample (9 μm -20wt%-25h) compared to the sample diluted with unprocessed PFA (M9 μm -20wt%-25h), due to the better filler particle dispersion and lower surface roughness of the undiluted sample. Therefore, increases in graphite content and filler distribution result in lower COF values.

The impact of particle size on the COF performance of the 20 wt% samples does not follow a clear trend; the 44- μm graphite filled sample has the lowest COF, followed by the 60-nm sample, and then the 9- μm sample. However, it is important to note that the ball milling process exfoliated the graphite particles such that the final graphite particle size is smaller than the initial particle size, as shown through microscopy and Raman analysis. The samples all displayed excellent COF performance for all filler weight fractions and particle sizes; with lower COF values than those from previous research under similar testing conditions. For example, the MF-MLG-2g-10wt% coating displayed the highest COF ($\mu=0.1293$), which is still lower compared to graphite-polymer coatings ($\mu=0.133$) [3] and graphene-polymer coatings ($\mu=0.1658$) [8] prepared via traditional processing methods (filler incorporation by blending in a tumbler mixer). The polymer composite with

20 wt% 44 μm graphite filler exhibited the lowest steady state COF, which is roughly 30% lower than the traditional graphite-polymer coatings under the same test conditions [3].

Large fluctuations observed in the COF values for the 20 wt% composites are due to the high surface roughness of the coating, which was also observed in a previous study with graphene-polymer coatings [8]. The extreme fluctuation displayed through sudden rises and drops in the COF values in the MF-MLG-2g-10wt% composite coating is due to the magnetic nanoparticles (magnetite and maghemite) attached to the MLG within the composite. Chen et al. analyzed the tribological performance of magnetite and maghemite (magnetitic nanoparticles) films and reported poor wear resistance and high coefficient of friction values [147]. Therefore, rises in the COF occur as large agglomerates of MF-MLG particles are worn within the coating, followed by drops in the COF when the MF-MLG agglomerates are removed through abrasive wear.

Despite the lower COF values, the 20 wt% samples still resulted in higher volumetric wear rates and mass losses. When analyzing the 20 wt% and 10 wt% samples separately, samples with higher COF values display higher volumetric wear rates. The minor particle stacking observed through microscopy in both the 60nm-20wt%-25h and 9 μm -20wt%-25h samples may have reduced the wear resistance of the coatings. Literature has shown that particle agglomeration generates stress fields within the matrix [148], resulting in failure initiation sites during wear [149], [150]. The filler particle agglomerates within the 9- μm graphite and 60-nm MLG composite coatings were more susceptible to flaking and particle pull-out during wear, reducing their wear resistance. This effect may have been more prominent in the samples containing the 9- μm graphite particles compared to the 60-nm MLG filler particles due to their larger particle size. It is interesting to note

that the MF-MLG-2g-10wt% sample displayed the third lowest wear rate but the second highest mass loss. This is due to the random dispersion of the large MF-MLG agglomerates within the coating. The removal of MF-MLG agglomerates during wear results in mass losses. However, their removal may be undetected in wear area calculations depending on where the micrographs are taken on the wear track. Therefore, the volumetric wear rate of the MF-MLG composites is likely higher than the estimated value.

The higher wear rates observed in the 20 wt% samples as compared to the 10 wt% samples are directly related to decreases in the cross-linking density [103]. The “cross-linking density reduction” effect results in decreases in mechanical properties when the graphene content is too high in graphene-polymer composites [96], [103]. Studies conducted by Zhang et al. displayed a similar decrease in the wear resistance of graphene polymer-composites when filler content was increased above 10 wt% [73]. At high graphene filler contents less polymer is available to surround and adhere the graphene filler particles within the matrix, making them susceptible to flaking off as debris during wear [73], [148]. Removal of material from the coating results in grooves and micro-crack formation on the coating surface, known as abrasive wear [146]. Abrasive wear leads to adhesive wear as the wear debris adheres to the counter-face surface and forms a transfer layer [73], [146], [148]. Material transfer is shown in laser/optical micrographs of the counter-face balls in Figure 4.25 and confirmed through EDS analysis.

The wear and failure mechanisms of the polymer composite coatings are observed through SEM, as shown in Figures 4.28 – 4.33. Corresponding to the higher volumetric wear rates and mass losses, significantly more abrasive wear is observed through SEM images of the 20 wt% coatings as compared to the 10 wt% coatings. The wear tracks on

the 20 wt% samples are readily distinguished from the unworn coating as the edges are smooth and visibly worn to the shape of the counter-face ball, with small grooves along the sliding direction. The wear tracks on the 10 wt% samples are much more subtle, showing slight smoothing of the polymer at the track edges with fine grooves along the sliding direction. The severity of abrasive wear for all samples progresses towards the centre of the wear track, with the onset of failure characterized by tearing and cracking within the coating. Similar failure mechanisms were observed in previous studies on graphite-polymer coatings [7], [8], [127]. Coating delamination and substrate exposure is further investigated through EDS.

Delamination and coating removal in polymer-composite coatings are typically observed as lighter areas within BSE images of the worn sample [7], [127]. Large patches of lighter areas are observed at the centre of the wear track on both the 60nm-20wt%-25h and 9 μ m-20wt%-25h coatings; high magnification BSE images at the centre of the wear track reveal 3 distinct material phases. EDS analysis confirms that all phases contain varying amounts of the substrate material and PFA. The lightest colour phase contains very low traces of PFA and high traces of the substrate material, whereas the darkest phase contains very low traces of the substrate material and high traces of PFA. As discussed above, these phases are known as a transfer film, and are formed when wear debris adheres to the coating and counter-face surfaces [73], [146], [148]. The transfer films help reduce the COF and abrasive wear, thus preventing the extremely large spikes in COF that typically occur after coating removal. Small specs of lighter material are observed on the 10 wt% and 20 wt% samples; EDS confirmed that all worn areas contain traces of PFA, thus complete coating removal did not occur in any of the coatings.

CHAPTER 6: CONCLUSIONS

This chapter summarizes the significant conclusions and future recommendation regarding the impact of the two different processing techniques, ball milling and magnetic functionalization, on the performance of the resulted graphite/graphene-polymer composite coatings.

6.1 Conclusions

- Microstructural analysis indicated that the ball milling process improves graphite filler particle dispersion and aligns graphite particles along the lateral direction. Alignment of filler particles is attributed to the large flake-like morphology of graphite particles, compatibility at the graphite-polymer interface, and is further enhanced through the compression molding and electrostatic spray coating processes. A strong interfacial interaction between the graphite and PFA particles was observed, thus preventing particle agglomeration during curing and contributing to excellent filler particle dispersion in the ball-milled composites.
- Raman analysis of the ball-milled graphite particles determined that monolayer graphene was not produced, as exhibited by the low intensity of the 2D band relative to the G band in the Raman Spectra. It is suggested that after an initial “breaking-in” period, the graphite particles are surrounded by a protective layer of PFA, which prevents further exfoliation of graphite particles through ball milling. Moreover, all samples experienced an increase in the defect intensity ratio after ball milling however, after 10 hours of ball milling the defect intensity ratio remained relatively consistent with no further increases.

- Thermal property analysis indicated that higher filler weight fractions and smaller graphite filler particles lead to higher thermal conductivities in the graphite-polymer composites. Interestingly, all samples displayed a significant decrease in thermal conductivity after ball milling. The lower thermal performance in the ball milled composites is due to the lateral alignment of the graphite filler particles. Graphite exhibits superior thermal properties along their in-plane direction. However, the thermal properties were measured along the out-of-plane direction, resulting in lower thermal conductivity values.
- Surface topography analysis displayed higher surface roughness values for composites with higher filler weight fractions, and smaller particle sizes. Increases in the surface roughness are attributed to decreases in the cross-linking density, such that the graphite particles are not adequately surrounded and adhered within the PFA matrix. Rough surfaces are prone to fouling and are therefore not desirable for heat exchangers, thus lower filler weight fractions (10 wt%) or surface modification would be required.
- Wear testing showed higher volumetric wear rates and mass losses in the composite coatings containing higher weight fractions of graphite filler (20 wt% versus 10 wt%). The reduced wear resistance in samples with higher filler content is due to the lower cross-linking density; the graphite particles are not adequately adhered within the polymer matrix and are susceptible to flaking off as debris during wear. Correspondingly, a combination of abrasive and adhesive wear was observed in all the graphite-polymer coatings. Failure mechanisms of the composite coating included cracking and tearing, and adhesive wear on both the worn surface and

wear counter-face. The adhesive wear formed a transfer film on the worn surface of the 60nm-20wt%-25h and 9 μ m-20wt%-25h coatings, reducing further abrasive wear and preventing COF increases on the severely worn surfaces. All samples displayed excellent steady state COF values, with lower values observed at higher graphite contents.

- Microstructural analysis indicated alignment of the MF-MLG particles within the PFA matrix was not achieved. Furthermore, thermal property analysis of the MF-MLG polymer composite displayed thermal conductivities comparable to randomly oriented graphene composites. The tribological performance of the MF-MLG composites was slightly lower as compared to the graphite-filled composites due to the negative impact of the magnetic nanoparticles.

6.2 Recommendations

Future work may focus on identifying different methods and instruments to analyze the thermal properties of the composite coating, rather than the compression-molded disk samples. Furthermore, the thermal performance of the ball-milled graphite polymer composite samples should be studied in both the in-plane and out-of-plane direction to fully characterize the impact of ball milling on the thermal properties. Studies may also be conducted to improve the surface roughness of the coating on the ball-milled composite samples through additional processing such as altering the composition of the top layer.

Although the MF-MLG particles were not aligned within the PFA matrix, the MF-MLG particles were magnetically responsive and are thus a promising technique to facilitate graphene filler alignment in composite materials. Future work may incorporate the MF-MLG particles in paint slurry based PFA coatings to investigate the effectiveness

of filler alignment in a liquid medium, rather than within a blended powder mixture. Additionally, electromagnetic field may be applied at high temperatures to prevent particle shifting during curing. If alignment is achieved, the corrosion resistance of the MF-MLG PFA composite should be investigated in a sulfuric acid medium to expand knowledge on the performance of the new composite in low temperature heat exchanger operating environments. Lastly, methods may be studied to simplify the procedure to attach the magnetic nano-particles onto the surface of the graphene particles and prevent potential agglomeration of graphene and MF-MLG particles during processing.

REFERENCES

- [1] I. Johnson and W. Chaote, “Waste Heat Recovery: Technology and Opportunities in U.S. Industry, Report of US Department of Energy, Industrial Technologies Program: Prepared by BCS, Incorporated.”
- [2] M. Li, S. Tang, F. Wang, Q. Zhao, and W. Tao, “Gas-side fouling , erosion and corrosion of heat exchangers for middle / low temperature waste heat utilization : A review on simulation and experiment,” *Appl. Therm. Eng.*, vol. 126, pp. 737–761, 2017.
- [3] Y. He, D. Walsh, and C. Shi, “Fluoropolymer composite coating for condensing heat exchangers : Characterization of the mechanical , tribological and thermal properties,” *Appl. Therm. Eng.*, vol. 91, pp. 387–398, 2015.
- [4] J. G. Cevallos, A. E. Bergles, A. Bar-cohen, P. Rodgers, and S. K. Gupta, “Polymer Heat Exchangers — History , Opportunities , and Challenges,” *Heat Transf. Eng.*, vol. 33, no. 13, pp. 1075–1093, 2012.
- [5] P. D. Roach and R. E. Holtz, “Plastic Heat Exchangers for Waste Heat Recovery,” Argonne, Illinois, 1983.
- [6] Y. He, J. Lo, and R. Santos, “Method and Composite for Preparing Heat Exchnagers for Corrosive Environments,” PCT/CA2013/000580, 2014.
- [7] Y. He, K. Farokhzadeh, and A. Edrissy, “Characterization of Thermal , Mechanical and Tribological Properties of Fluoropolymer Composite Coatings,” *J. Mater. Eng. Perform.*, vol. 26, no. June, pp. 2520–2534, 2017.
- [8] M. Cierpisz, “Development of Graphene-Filled Fluoropolymer Composite Coatings for Condensing Heat Exchangers,” 2020.
- [9] Y. Tong, S. Bohm, and M. Song, “Graphene based materials and their composites as coatings,” *Austin J. Nanomedicine Nanotechnol.*, vol. 1, no. 1, pp. 1–16, 2013.
- [10] W. Guo and G. Chen, “Fabrication of Graphene / Epoxy Resin Composites with

- Much Enhanced Thermal Conductivity via Ball Milling Technique,” *J. Appl. Polym. Sci.*, vol. 131, no. 15, pp. 1–5, 2014.
- [11] A. Li, C. Zhang, and Y.-F. Zhang, “Thermal Conductivity of Graphene-Polymer Composites: Mechanisms, Properties, and Applications,” *Polymers (Basel)*, vol. 9, pp. 437–454, 2017.
- [12] N. Burger, A. Laachachi, M. Ferriol, M. Lutz, V. Toniazzo, and D. Ruch, “Review of thermal conductivity in composites: Mechanisms, parameters and theory,” *Prog. Polym. Sci.*, pp. 1–28, 2016.
- [13] J. Renteria *et al.*, “Magnetically-functionalized self-aligning graphene fillers for high-efficiency thermal management applications,” *Mater. Des.*, vol. 88, pp. 214–221, 2015.
- [14] M. Kutz, “3.8.2 PFA Properties,” in *Applied Plastics Engineering Handbook- Processing, Materials, and Applications (2nd Edition)*, 2017, pp. 64–65.
- [15] W. Wei, F. Sun, Y. Shi, and L. Ma, “Theoretical prediction of acid dew point and safe operating temperature of heat exchangers for coal-fired power plants,” *Appl. Therm. Eng.*, vol. 123, pp. 782–790, 2017.
- [16] M. P. Perujo, “Condensation of Water Vapor and Acid Mixtures from Exhaust Gases,” Technical University of Berlin, 2004.
- [17] R. K. Srivastava, C. A. Miller, C. Erickson, and R. Jambhekar, “Emissions of Sulfur Trioxide from Coal-Fired Power Plants,” *J. Air Waste Manage. Assoc.*, vol. 54, no. 6, pp. 750–762, 2004.
- [18] Y. C. Wang and G. H. Tang, “Prediction of sulfuric acid dew point temperature on heat transfer fin surface,” *Appl. Therm. Eng.*, vol. 98, pp. 492–501, 2016.
- [19] R. G. I. Leferink and W. m. m. Huijbregts, “Nitrate stress corrosion cracking in waste heat recovery boilers,” *Anti-Corrosion Methods Mater.*, vol. 49, no. 2, pp. 118–126, 2002.

- [20] E. Levy, H. Bilirgen, and J. Dupont, "Recovery of water from boiler flue gas using condensing heat exchangers," Bethlehem, PA, 2011.
- [21] X. Q. Cheng, F. L. Sun, S. J. Lv, and X. G. Li, "A new steel with good low-temperature sulfuric acid dew point corrosion resistance," *Mater. Corros.*, vol. 63, no. 7, pp. 598–606, 2012.
- [22] Q. Ding, X.-F. Tang, and Z.-G. Yang, "Failure analysis on abnormal corrosion of economizer tubes in a waste heat boiler," *Eng. Fail. Anal.*, vol. 73, pp. 129–138, 2017.
- [23] M. G. Fontana, "Chapter 7- Mineral Acids," in *Corrosion Engineering, 3rd Edition*, New York: McGraw-Hill Book Company, 1987, pp. 317–337.
- [24] S. K. Brubaker, "Section 77- Corrosion by Sulfuric Acid," in *ASM Handbook, 13C-Corrosion: Environments and Industries*, 2006, pp. 659–667.
- [25] R. Ebara, F. Tanaka, and M. Kawasaki, "Sulfuric acid dew point corrosion in waste heat boiler tube for copper smelting furnace," *Eng. Fail. Anal.*, vol. 33, pp. 29–36, 2013.
- [26] W. M. M. Huijbregts and R. G. I. Leferink, "Latest advances in the understanding of acid dewpoint corrosion : corrosion and stress corrosion cracking in combustion gas condensates," *Anti-Corrosion Methods Mater.*, vol. 51, no. 3, pp. 173–188, 2004.
- [27] L. Zaheed and R. J. J. Jachuck, "Review of polymer compact heat exchangers , with special emphasis on a polymer film unit," *Appl. Therm. Eng.*, vol. 24, pp. 2323–2358, 2004.
- [28] P. A. Schweitzer, *Mechanical and Corrosion-Resistant Properties of Plastics and Elastomers*. Fallston, Maryland: CRC Press, 2002.
- [29] M. Xuehu, C. Jiabin, and L. Jifang, "Dropwise Condensation Heat Transfer of Steam on a Polytetrafluoroethylene Film," *J. Therm. Sci.*, vol. 10, no. 3, pp. 247–253, 2001.

- [30] A. T. Paxson, J. L. Yagüe, K. K. Gleason, and K. K. Varanasi, “Stable Dropwise Condensation for Enhancing Heat Transfer via the Initiated Chemical Vapor Deposition (iCVD) of Grafted Polymer Films,” *Adv. Mater.*, vol. 26, pp. 418–423, 2014.
- [31] A. S. Wanniarachchi, P. J. Marto, D. H. Boone, and J. W. Rose, “The Use of Organic Coatings to Promote Dropwise Condensation of Steam,” *Trans. ASME*, vol. 109, pp. 768–774, 1987.
- [32] M. Ahlers, A. Buck-emden, and H. Bart, “Is dropwise condensation feasible ? A review on surface modifications for continuous dropwise condensation and a profitability analysis,” *J. Adv. Res.*, vol. 16, pp. 1–13, 2019.
- [33] D. Miller, R. E. Holtz, R. N. Koopman, T. J. Marciniak, and D. R. MacFarlane, “Plastic Heat Exchnagers: A State-of-The-Art-Review,” 1979.
- [34] X. Chen, Y. Su, D. Reay, and S. Riffat, “Recent research developments in polymer heat exchangers – A review,” *Renew. Sustain. Energy Rev.*, vol. 60, pp. 1367–1386, 2016.
- [35] R. K. Shah, “Advances in Science and Technology of Compact Heat Exchangers,” *Heat Transf. Eng.*, vol. 27, no. 5, pp. 3–22, 2006.
- [36] Y. P. Mamunya, V. V Davydenko, P. Pissis, and E. V Lebedev, “Electrical and thermal conductivity of polymers filled with metal powders,” *Eur. Polym. J.*, vol. 38, pp. 1887–1897, 2002.
- [37] E. Ge, “Electrical and thermal behavior of polypropylene filled with copper particles,” vol. 36, pp. 1545–1554, 2005.
- [38] M. A. Yarbrough and A. Coats, “Corrosion-Resistant Composition of Matter Having Enhanced Thermal Conductivity, Heat Exchangers Made Therefrom, and Method of Making Same,” US 6465561 B1, 2002.
- [39] I. Krupa and I. Chod, “Physical properties of thermoplastic / graphite composites,” vol. 37, pp. 2159–2168, 2001.

- [40] O. Breuer and U. Sundararaj, "Big Returns From Small Fibers : A Review of Polymer / Carbon Nanotube Composites," vol. 25, no. 6, pp. 630–645, 2004.
- [41] W. Cheewawuttipong, D. Fuoka, S. Tanoue, H. Uematsu, and Y. Iemoto, "Thermal and Mechanical Properties of Polypropylene / Boron Nitride Composites," *Energy Procedia*, vol. 34, pp. 808–817, 2013.
- [42] J. G. Drobny, *Technology of Fluoropolymers, 2nd ed.* Boca Raton: CRC Press, 2008.
- [43] S. Ebnesajjad, "9.2 Perfluoroalkoxy Polymer," in *Fluoroplastics, Volume 2: Melt Processible Fluoropolymers- The Definitive User's Guide and Data Book*, 2nd ed., 2015, pp. 216–235.
- [44] Q. Zhuang, P. Geddis, B. Clements, and V. Ko, "Corrosion-Resistant Coating Development with Potential Application in Equipment of Low-Temperature Waste Heat Recovery," vol. 96, pp. 101–106, 2018.
- [45] E. Leivo, T. Wilenius, T. Kinoshita, P. Vuoristo, and T. Mäntylä, "Properties of thermally sprayed fluoropolymer PVDF , ECTFE , PFA and FEP coatings," *Prog. Org. Coatings*, vol. 49, pp. 69–73, 2004.
- [46] D. M. Bigg, "Thermal Conductivity of Heterophase Polymer Compositions," in *Thermal and Electrical Conductivity of Polymer Materials*, vol. 119, Columbus, Ohio: Springer-Verlag Berlin Heidelberg, 1995, pp. 1–30.
- [47] Y. Agar, T. Uno, and O. Municipal, "Estimation on Thermal Conductivities of Filled Polymers," *J. Appl. Polym. Sci.*, vol. 32, pp. 5705–5712, 1986.
- [48] C. Xiang, H. Sue, J. Chu, and B. Coleman, "Scratch Behavior and Material Property Relationship in Polymers," *J. Polym. Sci. Part B Polym. Phys.*, vol. 39, no. 1, pp. 47–59, 2001.
- [49] J. McPhedran, A. Edrisy, and Y. He, "Tribological Properties of Polymer Composite Coatings Report," 2019.

- [50] K. S. Novoselov *et al.*, “Electric field effect in atomically thin carbon films,” *Science* (80-.), vol. 306, no. 5696, pp. 666–669, 2004.
- [51] A. Bianco *et al.*, “All in the graphene family – A recommended nomenclature for two-dimensional carbon materials,” *Carbon N. Y.*, vol. 65, pp. 1–6, 2013.
- [52] V. Singh, D. Joung, L. Zhai, and S. Das, “Graphene based materials: Past, present and future,” *Prog. Mater. Sci.*, vol. 56, no. 8, pp. 1178–1271, 2011.
- [53] A. A. Balandin *et al.*, “Superior Thermal Conductivity of Single-Layer Graphene,” *Am. Chem. Soc.*, vol. 8, no. 3, pp. 902–907, 2008.
- [54] A. A. Balandin, “Thermal Properties of Graphene , Carbon Nanotubes and Nanostructured Carbon Materials,” *Nat. Mater.*, vol. 10, no. 8, pp. 569–581, 2011.
- [55] C. Lee, J. W. Kysar, X. Wei, and J. Hone, “Measurement of the elastic properties and intrinsic strength of monolayer graphene,” *Science* (80-.), vol. 321, pp. 385–388, 2008.
- [56] C. Lee, X. Wei, Q. Li, R. Carpick, J. W. Kysar, and J. Hone, “Elastic and frictional properties of graphene,” *Phys. Status Solidi B*, vol. 246, no. 11–12, pp. 2562–2567, 2009.
- [57] L. Lin, D. Kim, W. Kim, and S. Jun, “Friction and wear characteristics of multi-layer graphene films investigated by atomic force microscopy,” *Surf. Coat. Technol.*, vol. 205, pp. 4864–4869, 2011.
- [58] C. Hsieh and W. Chen, “Water / oil repellency and work of adhesion of liquid droplets on graphene oxide and graphene surfaces,” *Surf. Coat. Technol.*, vol. 205, no. 19, pp. 4554–4561, 2011.
- [59] K. S. Novoselov, V. I. Fal, L. Colombo, P. R. Gellert, M. G. Schwab, and K. Kim, “A roadmap of graphene,” *Nature*, vol. 490, pp. 192–200, 2012.
- [60] W. Ren and H. Cheng, “The global growth of graphene,” *Nat. Publ. Gr.*, vol. 9, pp. 726–730, 2014.

- [61] K. M. F. Shahil and A. A. Balandin, "Thermal properties of graphene and multilayer graphene : Applications in thermal interface materials," *Solid State Commun.*, vol. 152, no. 15, pp. 1331–1340, 2012.
- [62] S. Ghosh *et al.*, "Dimensional crossover of thermal transport in few-layer graphene materials," *Nat. Mater.*, vol. 9, no. 7, pp. 55–558, 2010.
- [63] T. C. Mokhena, M. J. Machane, J. S. Sefadi, S. V. Motloug, and D. M. Andala, "11. Thermal conductivity of graphite-based polymer composites," in *Impact of Thermal Conductivity on Energy Technnologies*, 2018, pp. 181–197.
- [64] G. Fugallo, A. Cepellotti, L. Paulatto, M. Lazzeri, N. Marzari, and F. Mauri, "Thermal Conductivity of Graphene and Graphite: Collective Excitations and Mean Free Paths," *Nano Lett.*, vol. 14, pp. 6109–6114, 2014.
- [65] H. Fukushima, L. T. Drzal, B. P. Rook, and M. J. Rich, "Thermal conductivity of exfoliated graphite nanocomposites," *J. Therm. Anal. Calorim.*, vol. 85, no. 1, pp. 235–238, 2006.
- [66] B. L. M. Veca *et al.*, "Carbon Nanosheets for Polymeric Nanocomposites with High Thermal Conductivity," *Adv. Mater.*, vol. 21, pp. 2088–2092, 2009.
- [67] A. Yu, P. Ramesh, M. E. Itkis, E. Bekyarova, and R. C. Haddon, "Graphite Nanoplatelet - Epoxy Composite Thermal Interface Materials," *J. Phys. Chem.*, vol. 111, pp. 7565–7569, 2007.
- [68] K. Liao, Y. Qian, and C. W. Macosko, "Ultralow percolation graphene / polyurethane acrylate nanocomposites," *Polymer (Guildf.)*, vol. 53, no. 17, pp. 3756–3761, 2012.
- [69] S. G. Miller *et al.*, "Characterization of epoxy functionalized graphite nanoparticles and the physical properties of epoxy matrix nanocomposites," *Compos. Sci. Technol.*, vol. 70, pp. 1120–1125, 2010.
- [70] M. Yoonessi and J. R. Gaier, "Highly Conductive Multifunctional Graphene Polycarbonate Nanocomposites," *ACS Nano*, vol. 4, no. 12, pp. 7211–7220, 2010.

- [71] T. Ramanathan *et al.*, “Functionalized graphene sheets for polymer nanocomposites,” *Nat. Nanotechnol.*, vol. 3, pp. 327–331, 2008.
- [72] L. Graphene *et al.*, “Enhanced mechanical properties of nanocomposites at low graphene content,” *ACS Nano*, vol. 3, no. 12, pp. 3884–3890, 2009.
- [73] W. Zhang, H. Zuo, X. Zhang, J. Wang, L. Guo, and X. Peng, “Preparation of graphene-perfluoroalkoxy composite and thermal and mechanical properties,” *Polymers (Basel)*, vol. 10, pp. 700–715, 2018.
- [74] M. K. Mondal, K. Biswas, and J. Maity, “A Transient Heat Transfer Model for Assessment of Flash Temperature During Dry Sliding Wear in a Pin-on-Disk Tribometer,” *Metall. Mater. Trans. A*, vol. 47, no. 1, pp. 600–607, 2015.
- [75] S. E. Mcelwain, T. A. Blanchet, L. S. Schadler, and W. G. Sawyer, “Effect of Particle Size on the Wear Resistance of Alumina-Filled PTFE Micro- and Nanocomposites,” *Tribol. Trans.*, vol. 51, pp. 247–253, 2008.
- [76] S. R. Chauhan and S. Thakur, “Effects of particle size , particle loading and sliding distance on the friction and wear properties of cenosphere particulate filled vinylester composites,” *Mater. Des.*, vol. 51, pp. 398–408, 2013.
- [77] W. X. Chen *et al.*, “Tribological behavior of carbon-nanotube-filled PTFE composites,” *Tribol. Lett.*, vol. 15, no. 3, pp. 275–278, 2003.
- [78] I. . A. Tsekmes, R. Kochetov, P. H. F. Morshuis, and J. . J. Smit, “Thermal Conductivity of Polymeric Composites : A Review,” *IEEE Int. Conf. Solid Dielectr.*, pp. 678–681, 2013.
- [79] T. Luo and J. R. Lloyd, “Enhancement of Thermal Energy Transport Across Graphene / Graphite and Polymer Interfaces : A Molecular Dynamics Study,” pp. 2495–2502, 2012.
- [80] X. Shen, Z. Wang, Y. Wu, X. Liu, and J. Kim, “Effect of functionalization on thermal conductivities of graphene / epoxy composites,” *Carbon N. Y.*, vol. 108, pp. 412–422, 2016.

- [81] B.-Y. Cao, J.-H. Zou, G.-J. Hu, and G.-X. Cao, "Enhanced thermal transport across multilayer graphene and water by interlayer functionalization," *Appl. Phys. Lett.*, vol. 112, no. 4, pp. 1–4, 2018.
- [82] D. An, S. Cheng, S. Xi, Z. Zhang, X. Duan, and Y. Ren, "Flexible thermal interfacial materials with covalent bond connections for improving high thermal conductivity," *Chem. Eng. J.*, vol. 383, no. 123151, pp. 1–9, 2020.
- [83] G. Han *et al.*, "Highly flame-retardant epoxy-based thermal conductive composites with functionalized boron nitride nanosheets exfoliated by one-step ball milling," *Chem. Eng. J.*, vol. UPDATE, IN, no. August, pp. 1–12, 2020.
- [84] H. Wu, W. Zhao, H. Hu, and G. Chen, "One-step in situ ball milling synthesis of polymer-functionalized graphene nanocomposites," *J. Mater. Chem.*, vol. 21, pp. 8626–8632, 2011.
- [85] C. Yu *et al.*, "One-Step in Situ Ball Milling Synthesis of Polymer-Functionalized Few-Layered Boron Nitride and Its Application in High Thermally Conductive Cellulose Composites," *ACS Appl. Nano Mater.*, vol. 1, pp. 4875–4883, 2018.
- [86] H. S. Kim, H. S. Bae, J. Yu, and S. Y. Kim, "Thermal conductivity of polymer composites with the geometrical characteristics of graphene nanoplatelets," *Sci. Rep.*, vol. 6, pp. 26825–26831, 2016.
- [87] K. Chu and W. L. Hongfeng, "Role of graphene waviness on the thermal conductivity of graphene composites," *Appl. Physics A*, vol. 111, pp. 221–225, 2013.
- [88] S. Chatterjee, F. Nafezarefi, N. H. Tai, L. Schlagenhauf, F. A. Nuesch, and B. T. T. Chu, "Size and synergy effects of nanofiller hybrids including graphene nanoplatelets and carbon nanotubes in mechanical properties of epoxy composites," *Carbon 50*, vol. 0, pp. 5380–5386, 2012.
- [89] J. Xiang and L. T. Drzal, "Investigation of exfoliated graphite nanoplatelets (x GnP) in improving thermal conductivity of paraffin wax-based phase change

- material,” *Sol. Energy Mater. Sol. Cells*, vol. 95, pp. 1811–1818, 2011.
- [90] F. Kargar *et al.*, “Thermal Percolation Threshold and Thermal Properties of Composites with High Loading of Graphene and Boron Nitride Fillers,” *ACS Appl. Mater. Interfaces*, vol. 10, pp. 37555–37565, 2018.
- [91] N. Shenogina, S. Shenogin, L. Xue, and P. Keblinski, “On the lack of thermal percolation in carbon nanotube composites,” *Appl. Phys. Lett.*, vol. 87, no. 133106, pp. 1–3, 2005.
- [92] E. Pop, V. Varshney, and A. K. Roy, “Thermal properties of graphene: fundamentals and applications,” *MRS Bull.*, vol. 37, pp. 1273–1281, 2012.
- [93] F. Wang, H. Wang, and J. Mao, “Aligned-graphene composites : a review,” *J. Mater.*, vol. 54, pp. 36–61, 2019.
- [94] Q. Li *et al.*, “Ultrahigh Thermal Conductivity of Assembled Aligned Multilayer Graphene/Epoxy Composite,” *Chem. Mater.*, vol. 26, pp. 4459–4465, 2014.
- [95] H. Yan, Y. Tang, W. Long, and Y. Li, “Enhanced thermal conductivity in polymer composites with aligned graphene nanosheets,” *J. Mater. Sci.*, vol. 49, pp. 5256–5264, 2014.
- [96] Y. Liu, H. Wu, and G. Chen, “Enhanced Mechanical Properties of Nanocomposites at Low Graphene Content Based on In Situ Ball Milling,” *Polym. Compos.*, vol. 37, pp. 1190–1197, 2016.
- [97] H. Wu, W. Zhao, and G. Chen, “One-Pot In Situ Ball Milling Preparation of Polymer / Graphene Nanocomposites,” *J. Appl. Polym. Sci.*, vol. 125, pp. 3899–3903, 2012.
- [98] M. Yi and Z. Shen, “A review on mechanical exfoliation for scalable production of graphene,” *J. Mater. Chem. A*, vol. 3, no. 22, pp. 11700–11715, 2015.
- [99] C. Teng, D. Xie, J. Wang, Z. Yang, G. Ren, and Y. Zhu, “Ultrahigh Conductive Graphene Paper Based on Ball-Milling Exfoliated Graphene,” *Adv. Funct. Mater.*,

vol. 27, no. 20, pp. 1–7, 2017.

- [100] M. Borah, M. Dahiya, S. Sharma, R. B. Mathur, and S. R. Dhakate, “Few Layer Graphene Derived from Wet Ball Milling of Expanded Graphite and Few Layer Graphene Based Polymer Composite,” *Mater. Focus*, vol. 3, pp. 1–10, 2014.
- [101] W. Zhao, M. Fang, F. Wu, H. Wu, L. Wang, and G. Chen, “Preparation of graphene by exfoliation of graphite using wet ball milling,” *J. Mater. Chem.*, vol. 20, no. 28, pp. 5817–5819, 2010.
- [102] M. Cai, D. Thorpe, D. H. Adamson, and H. C. Schniepp, “Methods of graphite exfoliation,” *J. Mater. Chem.*, vol. 22, no. 48, pp. 24992–25002, 2012.
- [103] C. Bao, Y. Guo, L. Song, Y. Kan, X. Qian, and Y. Hu, “In situ preparation of functionalized graphene oxide/epoxy nanocomposites with effective reinforcements,” *J. Mater. Chem.*, vol. 21, pp. 13290–13298, 2011.
- [104] A. C. Ferrari, “Raman spectroscopy of graphene and graphite: Disorder, electron-phonon coupling, doping and nonadiabatic effects,” *Solid State Commun.*, vol. 143, pp. 47–57, 2007.
- [105] S. Wu *et al.*, “Aligning multilayer graphene flakes with an external electric field to improve multifunctional properties of epoxy nanocomposites,” *Carbon N. Y.*, vol. 94, pp. 607–618, 2015.
- [106] N. Yousefi *et al.*, “Highly aligned, ultralarge-size reduced graphene oxide/polyurethane nanocomposites: Mechanical properties and moisture permeability,” *Compos. Part A Appl. Sci. Manuf.*, vol. 49, pp. 42–50, 2013.
- [107] C. Yuan, B. Duan, L. Li, B. Xie, M. Huang, and X. Luo, “Thermal Conductivity of Polymer-Based Composites with Magnetic Aligned Hexagonal Boron Nitride Platelets,” *ACS Appl. Mater. Interfaces*, vol. 7, pp. 13000–13006, 2015.
- [108] Z. Lin, Y. Liu, S. Raghavan, K. S. Moon, S. K. Sitaraman, and C. P. Wong, “Magnetic alignment of hexagonal boron nitride platelets in polymer matrix: Toward high performance anisotropic polymer composites for electronic

- encapsulation,” *ACS Appl. Mater. Interfaces*, vol. 5, pp. 7633–7640, 2013.
- [109] Y. Haik, J. Chatterjee, and C.-J. Chen, “Alignment of carbon nanotubes using magnetic particles,” 2010.
- [110] M. Liu, H. Younes, H. Hong, and G. P. Peterson, “Polymer nanocomposites with improved mechanical and thermal properties by magnetically aligned carbon nanotubes,” *Polymer (Guildf)*., vol. 166, pp. 81–87, 2019.
- [111] H. Yan, R. Wang, Y. Li, and W. Long, “Thermal Conductivity of Magnetically Aligned Graphene–Polymer Composites with Fe₃O₄-Decorated Graphene Nanosheets,” *J. Electron. Mater.*, vol. 44, no. 2, pp. 658–666, 2015.
- [112] M. A. Correa-Duarte *et al.*, “Alignment of carbon nanotubes under low magnetic fields through attachment of magnetic nanoparticles,” *J. Phys. Chem. B*, vol. 109, pp. 19060–19063, 2005.
- [113] M. A. Correa-Duarte, N. Sobal, L. M. Liz-Marzán, and M. Giersig, “Linear assemblies of silica-coated gold nanoparticles using carbon nanotubes as templates,” *Adv. Mater.*, vol. 16, no. 23–24, pp. 2179–2184, 2004.
- [114] L. Li, Y. Cui, Z. Zhang, P. Tu, H. Gong, and P. Li, “Preparation of graphene/Fe₃O₄ composite varnish with excellent corrosion-resistant and electromagnetic shielding properties,” *Ceram. Int.*, vol. 46, pp. 22876–22882, 2020.
- [115] Y. Zhan, J. Zhang, X. Wan, Z. Long, S. He, and Y. He, “Epoxy composites coating with Fe₃O₄ decorated graphene oxide: Modified bio-inspired surface chemistry, synergistic effect and improved anti-corrosion performance,” *Appl. Surf. Sci.*, vol. 436, pp. 756–767, 2018.
- [116] J. P. Howe, “Properties of Graphite,” *J. Am. Ceram. Soc.*, vol. 35, no. 11, pp. 275–282, 1952.
- [117] M. A. Correa-Duarte *et al.*, “Alignment of carbon nanotubes under low magnetic fields through attachment of magnetic nanoparticles: Supporting Information,” *J.*

- Phys. Chem. B*, vol. 109, no. 41, pp. 19060–19063, 2005.
- [118] Retsch, “Colloidal Grinding,” Haan, Germany, 2005.
- [119] Retsch, “Ball Mills- Guidelines for sample amount and ball charge,” Haan, Germany, 2020.
- [120] R. Massart, “Preparation of Aqueous Magnetic Liquids in Alkaline and Acidic Media,” *IEEE Trans. Magn.*, vol. 17, no. 2, pp. 1247–1248, 1981.
- [121] T. Ferreira and W. Rasband, “ImageJ User Guide,” 2012.
- [122] L. Reinking, “Examples of Image Analysis Using ImageJ,” 2007.
- [123] ASTM International, “ASTM E1461-01, Standard Test Method for Thermal Diffusivity by the Flash Method 1,” 2001.
- [124] ASTM International, “ASTM E1269-11, Standard Test Method for Determining Specific Heat Capacity by Differential Scanning,” 2018.
- [125] W. J. Parker, R. J. Jenkins, C. P. Butler, and G. L. Abbott, “Flash Method of Determining Thermal Diffusivity, Heat Capacity, and Thermal Conductivity,” *J. Appl. Phys.*, vol. 32, pp. 1679–1684, 1961.
- [126] ASTM International, “Standard Test Method for Wear Testing with a Pin-on-Disk Apparatus: G99-05,” 2010.
- [127] K. Farokhzadeh, A. Edrisy, and H. Y., “Tribological and Mechanical Properties of Polymer Composite Coatings,” 2014.
- [128] K. Farokhzadeh, “Modification of Ion Nitriding of Ti – 6Al – 4V for Simultaneous Improvement of Wear and Fatigue Properties,” University of Windsor, Canada, 2014.
- [129] M. Wall, “The Raman Spectroscopy of Graphene and the Determination of Layer Thickness,” WI, USA, 2011.
- [130] A. C. Ferrari *et al.*, “Raman Spectrum of Graphene and Graphene Layers,” *Am.*

Phys. Soc., vol. 97, no. 18, pp. 187401–187404, 2006.

- [131] K. R. Paton *et al.*, “Scalable production of large quantities of defect-free few-layer graphene by shear exfoliation in liquids,” *Nat. Mater.*, vol. 13, no. 6, pp. 624–630, 2014.
- [132] T. Xing *et al.*, “Disorder in ball-milled graphite revealed by Raman spectroscopy,” *Carbon N. Y.*, vol. 57, pp. 515–519, 2013.
- [133] Y. Ming *et al.*, “Anisotropic thermal transport in MOF-5 composites,” *Int. J. Heat Mass Transf.*, vol. 82, pp. 250–258, 2015.
- [134] L. W. Wang, Z. Tamainot-Telto, S. J. Metcalf, R. E. Critoph, and R. Z. Wang, “Anisotropic thermal conductivity and permeability of compacted expanded natural graphite,” *Appl. Therm. Eng.*, vol. 30, no. 13, pp. 1805–1811, 2010.
- [135] S. Deng, Y. Zhu, X. Qi, W. Yu, F. Chen, and Q. Fu, “Preparation of polyvinylidene fluoride/expanded graphite composites with enhanced thermal conductivity via ball milling treatment,” *R. Soc. Chem.*, no. 6, pp. 45578–45584, 2016.
- [136] P. Kumar, S. Yu, F. Shahzad, S. M. Hong, Y. H. Kim, and C. M. Koo, “Ultrahigh electrically and thermally conductive self-aligned graphene/polymer composites using large-area reduced graphene oxides,” *Carbon N. Y.*, vol. 101, pp. 120–128, 2016.
- [137] N. Yousefi *et al.*, “Simultaneous in situ reduction, self-alignment and covalent bonding in graphene oxide/epoxy composites,” *Carbon N. Y.*, vol. 59, pp. 406–417, 2013.
- [138] L. Blaney, “Magnetite (Fe_3O_4): Properties , Synthesis , and Applications,” *Lehigh Rev.*, vol. 15, 2007.
- [139] V. N. Nikiforov, A. E. Goldt, E. A. Gudilin, V. G. Sredin, and V. Y. Irhin, “Magnetic Properties of Maghemite Nanoparticles,” *Bull. Russ. Acad. Sci. Phys.*, vol. 78, no. 10, pp. 1330–1335, 2014.

- [140] H. U. Zettler, M. Weiß, Q. Zhao, and H. Müller-Steinhagen, "Influence of surface properties and characteristics on fouling in plate heat exchangers," *Heat Transf. Eng.*, vol. 26, no. 2, pp. 3–17, 2005.
- [141] A. Alofi and G. P. Srivastava, "Thermal conductivity of graphene and graphite," vol. 115421, no. March, pp. 1–10, 2013.
- [142] Y. Grosu *et al.*, "Natural and by-product materials for thermocline-based thermal energy storage system at CSP plant : Structural and thermophysical properties," *Appl. Therm. Eng.*, vol. 136, no. March, pp. 185–193, 2018.
- [143] Z. Hu *et al.*, "Facile preparation of poly (p-phenylene benzobisoxazole)/ graphene composite films via one-pot in situ polymerization," *Polymer (Guildf.)*, vol. 71, pp. 8–14, 2015.
- [144] J. Gu, J. Du, J. Dang, W. Geng, and Q. Zhang, "Thermal conductivities, mechanical and thermal properties of graphite nanoplatelets/ polyphenylene sulfide composites," *RSC Adv.*, vol. 4, pp. 22101–22105, 2014.
- [145] Z. Zhang, C. Breidt, L. Chang, F. Hauptert, and K. Friedrich, "Enhancement of the wear resistance of epoxy : short carbon fibre , graphite , PTFE and nano-TiO 2," *Compos. Part A*, vol. 35, pp. 1385–1392, 2004.
- [146] A. Abdelbary, "Polymer Tribology," in *Wear of Polymers and Composites*, 2014, pp. 1–36.
- [147] M. Chen, J. Lin, T. Wu, and G. Castillo, "Wear resistance of iron oxide thin films," *J. Appl. Phys.*, vol. 63, pp. 3275–3277, 1988.
- [148] M. Zouari, M. Kharrat, M. Dammak, and M. Barletta, "Progress in Organic Coatings A comparative investigation of the tribological behavior and scratch response of polyester powder coatings filled with different solid lubricants," *Prog. Org. Coatings*, vol. 77, no. 9, pp. 1408–1417, 2014.
- [149] B. Wetzal, F. Hauptert, K. Friedrich, M. Q. Zhang, and M. Z. Rong, "Impact and wear resistance of polymer nanocomposites at low filler content," *Polym. Eng.*

Sci., vol. 42, no. 9, pp. 1919–1927, 2002.

- [150] I. O. Oladele, A. D. Akinwekomi, O. G. Agbabiaka, and M. O. Oladejo, “Influence of biodegradation on the tensile and wear resistance properties of bio-derived CaCO₃/epoxy composites,” *J. Polym. Res.*, vol. 26, no. 1, pp. 1–9, 2019.

VITA AUCTORIS

NAME: Joselyne McPhedran

PLACE OF BIRTH: Windsor, ON

YEAR OF BIRTH: 1996

EDUCATION: Sandwich Secondary School, LaSalle, ON,
2014

University of Windsor, B.A.Sc., Windsor, ON,
2018

University of Windsor, M.A.Sc., Windsor, ON,
2021